ADVANCED LECTURES 1987

CLOUD PHYSICS

VOLUME 2

LECTURE 4: THE PHYSICS OF LOW LEVEL STRATIFORM CLOUD

by S NICHOLLS, MET O 15

4.1 INTRODUCTION

Although stratiform cloud is observed at all levels in the atmosphere, we will concentrate here on low level layer clouds: stratocumulus (Sc) and stratus (St). The complications of the ice phase will be ignored although many of the concepts may be usefully generalised to deal with As or Cs.

Although these cloud types have a very limited vertical extent, often no more than a few hundred metres (which causes severe problems for models whose vertical grid resolution is greater than this), they cover very large areas - often in excess of a million square km, and tend to be very persistent. This is especially true around the edges of the subtropical anticyclones (Fig 1) where the combination of strong subsidence and cool ocean currents favour their formation. However even in the UK local area where our weather is dominated by mobile synoptic scale systems, stratocumulus is by far the most often reported cloud type (Fig 2). Other significant areas of low level stratiform cloud include polar stratus. It is estimated that stratus covers about 70% of the Arctic basin during the summer months.

The importance of Sc and St lie in the accompanying changes in the radiation budget. This drastically alters the energy transfers within, and therefore the structure of, the boundary layer and the surface energy balance. Forecasts of boundary layer phenomena: max/min temperatures, road surface conditions, fog formation & dispersal etc are therefore highly sensitive to the presence of these clouds. On a global scale, the planetary albedo and the the heat input to the ocean surface are strongly affected. In general, it is widely believed that inceased low level cloud would cause global cooling (a greatly increased shortwave albedo is not balanced by an equal reduction in longwave loss), Cs is generally thought to have the opposite effect. Which effect predominates clearly depends on the optical properties of the clouds (see lectures 6 & 7) together with their height (temperature).

Although these layer clouds cause relatively large amounts of energy to be redistributed, the processes responsible for their formation and maintainance are often closely balanced so that the clouds may be quite long lived. Because this balance involves interactions between turbulent motion, radiative transfer and cloud microphysics which are not well understood and difficult to quantify, predicting cloud evolution is particularly uncertain.

An expanded account of many of the issues discussed here and related topics may be found in Ref 13.

4.2. PHYSICAL PROCESSES OCCURRING IN STRATOCUMULUS

4.2.1 GENERAL FEATURES

In order to simplify discussion, we will limit attention to a single cloud layer. The formation of Sc is associated with the cooling or moistening of the boundary layer or the spreading out of cumulus beneath an inversion. The general features are best illustrated by a typical example (Fig 3). This shows data taken on a single aircraft descent and from a nearby radiosonde. These were taken in an extensive cloud layer which covered most of the North Sea (Fig 4). Unbroken cloud fills the upper half of the boundary layer beneath a marked inversion and hydrolapse. Other observations show that the region beneath the inversion is turbulent while the air above cloud top is not due to the strong static stability. The relatively large density difference keeps local perturbations of the interface small, so cloud top is quite flat: varying by no more than 100m over 100nm. However, on small scales (< few km) there are vertical variations of a few 10's of m caused by the turbulent motions beneath (or by shear across the interface in some situations). Convectively driven turbulent motions often show cellular type patterns at cloud top (Fig 5), which are especially obvious with grazing illumination, indicating rising motion in the centres with descent around the edges. Consequently, even in such horizontally uniform situations, there may be considerable small scale fluctuations (eg see Fig 3). The effect of the turbulent motion is to slowly erode (or entrain, see 4.2.4) the inversion from below which acts to keep the inversion sharply defined. These inversions may be very large (strong), up to 15K, and have extremely large vertical gradients, locally several degrees per metre.

Returning to Fig 3, we see that the liquid water content (q_l) increases with height to be a maximum close to cloud top. This contrasts with the situation usually found in other cloud types (eg Cu) where q_l decreases above a maximum reached lower down in the cloud. This is because dry air can only be mixed in through cloud top in Sc or St, and as we have seen this is impeded by the adverse density gradient there. In fact, any conserved quantity will tend to become equally distributed with height in any well-mixed layer eg potential temperature in a daytime convective boundary layer, because vertical gradients within the layer are prevented from forming by the efficient vertical mixing. Once cloud forms, the conservative thermodynamic variables must be modifed:

No cloud	Cloud
Potential temp, θ	Equivalent pot. temp, θ_e
Specific humidity, q	Total sp. hum., q_T

where

$$\theta_e = \theta \exp\left(\frac{L_v}{c_p}\frac{q_l}{T}\right) \quad \text{and} \quad q_T = q + q_l .$$

(θ_e , q_T) together with pressure fully specify the thermodynamic state if supersaturation is negligible. Note that in Fig 3, both θ_e and

($q + q_l$) are approximately constant with height in the boundary layer. Within cloud, q is constrained to be the saturation value at the local temperature which itself must be wet adiabatic. Thus q must decrease at a specified rate and the excess water ie $q_T - q$ must appear as liquid. q_l therefore increases with height at the adiabatic rate (approx. 1 g/kg/km, shown dotted on Fig 3) if q_T is constant with height. Observations tend to show that q_l does increase roughly linearly with height in stratocumulus, but at a somewhat smaller rate than adiabatic which probably reflects the mixing of drier air through cloud top. Note also that if vertical mixing is insufficient to render q_T height invariant, then q_l need not be close to the adiabatic value.

Only a small fraction (typically <20%) of the total water content appears in the liquid phase at any level. Relatively small errors in q_T or insufficient resolution of the inversion can lead to significant changes in the diagnosed cloud depth.

Cloudbase is located at the lifting condensation level, but even small variations in q_T and temperature cause significant variations in this level. Therefore, cloudbase is usually much more variable locally (eg $\pm$ 100m) than cloudtop.

4.2.2 MICROPHYSICAL STRUCTURE

The microphysical structure of the cloud is important for two main reasons:

i) Radiative transfer calculations are sensitive to drop size distributions (dsd's) as well as liquid water path.

ii)The formation of drizzle is also depends on the dsd's.

The microphysical properties of these clouds vary according to the CCN distributions, but it is fairly common to find that there is little variation in the droplet concentration with height (see Fig 6), although the actual value may vary widely from case to case. The increase in liquid water content is solely accounted for by an increase in mean droplet size. This is consistent with a simple microphysical explanation (Fig 7). If the peak supersaturation is attained near cloudbase because of the rapid activation of sufficient nuclei, continued condensation within updrafts will occur preferentially onto these preexisting drops. They limit the supersaturation by readily accepting the available vapour which prevents additional nuclei being activated.

As soon as the cloud layer becomes a few hundred metres thick, the liquid water path becomes sufficient for warm coalescence to transfer water from droplets < 20μm radius to drizzle drops ($r \sim 100\mu m$). The ability of such shallow clouds to produce significant amounts of drizzle is thought to be due to the effects of turbulent diffusion prolonging the lifetimes of a fraction of drops within the cloud (Ref 1). Although the vast majority of the liquid water within the cloud is still contained in the small drops (<20μm), the transport of water by gravitational settling (drizzle) is sensitive to the presence

of a relatively few large drops. This is because liquid water content is proportional to nr^3 while transport is proportional to nr^3v. The fallspeed, v, goes roughly as r^2 for drops up to drizzle size, so the transport rate is proportional to nr^5 (cf radar reflectivity which is proportional to nr^6). The relative contribution to the drizzle rate therefore depends on whether the number distribution decreases faster or less than r^{-5}.

This process may be less important in clouds with high droplet concentrations due to the reduced efficiency of the coalescence process, but in maritime clouds both models and observations suggest that the losses by drizzle may exceed the supply from the (upward) turbulent water vapour flux. Of course not all the drizzle will necessarily reach the ground. Smaller drops will evaporate in the subsaturated subcloud layer. The resultant cooling may also influence the dynamics of this layer.

4.2.3 CLOUD - RADIATION INTERACTION

With extensive layer clouds, horizontal scales are very large compared to vertical ones and the radiative properties may be discussed to sufficient accuracy in terms of two streams: upward and downward irradiance. Furthermore, since we are interested in the net heating effects only, it is sufficient to consider only the broadband fluxes: shortwave (0.3-4μm), $S\uparrow, S\downarrow$, and longwave (4-40μm), $L\uparrow, L\downarrow$. The main problem is to adequately determine the vertical variation of these fluxes in terms of known quantities eg liquid water content, dsd's etc. However, a number of efficient computational methods have been derived to calculate these fluxes for plane parallel clouds (eg Refs 2 & 3 and see lectures 6 & 7) which appear to offer a sufficiently accurate results. The details of these methods are not discussed further here. Because of the difficulty in making measurements, especially in cloud, it is generally felt that the calculated fluxes are less prone to error so much of the following discussion is based on calculations. In special cases good agreement has been demonstrated between observations and theory (eg Ref 4).

IR optical properties. A common approximation here is to neglect scattering and consider the cloud particles as pure absorbers. This is justified by the very strong molecular absorption outside the IR window (8-14μm) which limits the main effects of liquid water to this wavelength range and because the scattering efficiency of typical cloud droplet sized particles is much smaller than in the visible.

Examples of calculated longwave fluxes $L\uparrow, L\downarrow$ for a cloud similar to that seen in Fig 6 are shown in Fig 8. Note the large gradients found at cloud top: about $70 Wm^{-2}$ in about 50m in $L\downarrow$. As the local heating rate is given by

$$\frac{d\theta}{dt} = -\frac{1}{\rho c_p} \, d(L\uparrow - L\downarrow)/dz$$

cloud top is cooling at a rate of several degrees per hour (Fig 9). This reflects the concentration of liquid water just below the

inversion and the clear, dry atmosphere above. Note also the tendency for the inversion layer to be cooled (reflecting the large temperature difference across cloud top) and for cloudbase to be warmed due to transfer through the window region from the warmer surface. In the centre of the cloud $L\uparrow \approx L\downarrow$ as if immersed in a black body. Considering the cloud layer as a whole, the total longwave loss is about 65 Wm^{-2}.

These features depend primarily on the cloud liquid water content, the variation of temperature and water vapour with height and the surface temperature. Cloud drop-size distributions have little effect.

Shortwave optical properties. These are characterized by strong multiple scattering by the cloud droplets which greatly increases the mean path length of a photon within cloud. Although the absorption coefficient of pure water is very small in the visible part of the spectrum, it increases in the near IR (1-4μm), and since 30% of the incoming solar flux is contained in this region, this is quite important. Absorption is not only due to droplets. Molecular absorption, mainly by water vapour, is also enhanced by the multiple scattering.

The shortwave properties are mainly dependent on the liquid water distribution, drop size distribution and solar zenith angle (ie time of day, latitude, season). Important contributions may also be made by aerosol loading both inside and outside droplets.

For relatively thick clouds (liquid water path > 1-200 gm^{-2}), calculations suggest that the albedo ($S\uparrow/S\downarrow$ evaluated just above cloud) should vary between 50% and 90%, with cloud layer absorption from 3% to 10%. The absorption increases with liquid water path (cloud depth) but reaches a limiting value if precipitation or aerosol loading is absent. As the zenith angle increases (ie low sun), the albedo increases and the percentage absorption decreases. There is also some dependance on drop size. With increasing drop size, a given cloud will tend to reflect less and absorb more.

Note there is still considerable discussion about the figures quoted above. Observed albedos tend to be slightly lower than the plane parallel, horizontally uniform calculations suggest probably because small scale fluctuations do exist. Measured absorptions, a notoriously difficult measurement to make, have been reported as high as 20%. This is difficult to explain theoretically. Possible explanations include experimental error, absorbing aerosols, large drops, horizontal inhomogeneities and finite cloud sizes.

Nevertheless, as typical values of $S\downarrow$ just above cloud are 1000Wm^{-2} (sun overhead), 800Wm^{-2} (UK summer midday), 400Wm^{-2} (UK October midday), even a 10% absorption is a significant amount. Examples of $S\uparrow, S\downarrow$ for midday, 60°N in July are shown in Fig 8 with the corresponding heating rates in Fig 9. Note that the depth over which the heating occurs is much greater than that over which the IR cooling takes place, although the net gain (the flux divergence across the cloud) is numerically about equal to the longwave loss in this example.

Although the shortwave heating is a maximum near cloud top, it is insufficient to cancel the locally intense IR cooling. The combined effect of the SW and LW on the local heating rates (Fig 9) is therefore to produce strong cooling within a few tens of metres of cloud top with warming beneath, although on this occasion there is little net heating of the whole layer. However, this distribution of heating is clearly strongly destabilizing and turbulent motions will be generated to redistribute this energy to greater depths. The magnitude of the SW absorption ($\sim 70 Wm^{-2}$) suggests that thick clouds may well display significant diurnal changes. This is less likely to be the case for thin clouds where the absorption is less, or at high latitudes or in winter (see Ref 5). This is confirmed by recent analyses of satellite data (Fig 10, Ref 7). Ref 5 suggests a mechanism which would explain these observations in terms of the processes outlined here.

4.2.4 TURBULENCE AND ENTRAINMENT

The local heating distribution shown in Fig 9 would, by itself, promote an unstable density stratification, so even in the absence of other sources, turbulent motions must be generated to compensate. In situations where radiative effects dominate, relatively cold, narrow, negatively buoyant downdrafts are observed descending from the vicinity of cloud top with relatively broad, warm updrafts between. Such motions therefore comprise an upward heat flux to balance the strong radiative cooling from cloud top. The downdrafts penetrate deep into the cloud, losing their buoyancy deficit in a similar manner seen in positively buoyant rising thermals in a clear, daytime convective boundary layer. The degree of penetration and the intensity of these motions depends on the energy balance of the whole layer.

There are two sources of turbulent kinetic energy (TKE) in such a layer: generation by buoyancy and shear. The generation of TKE by buoyancy depends mainly on the magnitude and location of internal (virtual) heat sources and the input at the boundaries. Heating the lower regions of the boundary layer or cooling the top will both tend to generate buoyancy and hence TKE. Heating the top or cooling the bottom will be sinks of buoyancy and will tend to destroy TKE. TKE is also transported vertically by a variety of mechanisms, so a layer with net TKE production may export some to a layer of net dissipation. There is a continuous destruction of TKE at all levels by (eventually) viscosity. It is this TKE balance which is crucial to the understanding of the transport processes within the whole cloud+subcloud layer and to the evolution of the layer with time. There may be considerable differences in this balance between a radiatively-driven convective cloud (Sc) and a strong wind situation where there is strong shear production (eg St). This may affect the water transport or entrainment so much that the gross characteristics of the cloud layer may be completely different. These are central questions which current research is trying to answer. All models are concerned with predicting the various source/sink and transport terms

from the known model variables (eg the radiative fluxes, surface conditions etc).

An important consequence of the cloud being turbulent is that relatively warm, dry air from the inversion is entrained into the cloud top. This continual erosion of the inversion maintains a very sharp interface. The actual mechanisms by which this occurs are not well known and probably vary from one situation to another. There are a number of important consequences:

i) Cloud top grows upwards. The boundary layer must therefore deepen as air passes through the upper boundary unless counteracted by subsidence ie

$$\frac{dh}{dt} = w + w_e$$

where dh/dt is the rate of change of the upper boundary surface, w is the large scale subsidence velocity and w_e is the "entrainment velocity". Thus in the absence of mean vertical motion, $w_e = dh/dt$. A typical value in Sc is w_e=0.5 cm/s (ie $w_e \approx w$ and is very difficult to measure experimentally).

ii) Positively buoyant air is pulled downwards into the cloud. This constitutes a negative buoyancy flux (although the cooling experienced as water drops are evaporated may offset this) which must be supported by some other source of TKE or transport from below. The previously quiescent air must also be supplied with TKE to bring it up to the levels found in cloud. These affect the TKE balance.

iii) Dry air is mixed into the cloud. Turbulence must therefore transport water from below if the cloud liquid water is to be maintained.

Although there are currently many different suggestions for predicting entrainment velocities, none has yet been shown to be accurate for cloudy layers. However, the fluxes associated with entrainment are often not as large as those due to other processes (eg radiative fluxes) so some degree of uncertainty can be tolerated. However in other cases is may be that entrainment dominates. It is not currently known whether, or how often, or in what conditions this might be the case.

Entrainment into a cloudy layer is much more complicated than that into a cloudfree layer. It is usual to use a characterstic turbulent velocity scale and some measure of the interfacial stability to try and predict the entrainment velocity. However, in the cloudy case, not only are the internal sources and sinks of TKE more varied, but there is the added complication of phase change occurring at the interface.

Consider the following situation in which less dense air with thermodynamic properties ($\theta_1, q_1, q_{T1}, \theta_{e1}, \theta_{v1}$) lies above denser air with properties (θ_2, q_2 etc) and is separated by a density interface. If a mass m_1 of state 1 is mixed isobarically with a mass m_2 of state 2 defining a mixing ratio

$$\epsilon = m_1 / (m_1 + m_2)$$

it can be shown (Ref 8) that the buoyancy excess of the mixture over that of state 2 is not necessarily positive. Under certain conditions, the density of the mixture is greater than either of the initial states. This can occur if the air in state 1 is so dry that evaporative cooling on mixing is great enough to compensate for the original temperature excess. There are two conditions necessary for this to occur:

i) The condition $\beta \Delta\theta_e < \theta \Delta q_T$ must be satisfied, where β is a slowly varying function of temperature (typically 0.5-0.6) and Δ = (state 1 - state 2).

ii) The mixture must remain saturated.

When considering cloud layers, state 1 is usually warmer and drier and state 2 contains liquid water.

Fig 11 shows values of buoyancy excess in terms of virtual temperature difference for two examples as a function of ϵ. Only when i) is satisfied do small negative values appear, and only at small values of ϵ because of ii). The turning point on the curves indicates where all of the liquid water in the mixture is just evaporated. Increasing the liquid water content of state 1 moves this point to higher ϵ's ie greater negative values are possible since there is more liquid to be evaporated.

Clearly, if these conditions are fulfilled, entrainment rather than being a sink of TKE will tend to produce TKE and will augment that from other sources. It has been suggested (Ref 9) that if i) is satisfied, such a situation would be unstable: turbulence promoting entrainment, increasing TKE production, increasing turbulence etc resulting in the rapid dispersal of the cloud. This has been termed "entrainment instability" and has been hypothesized to be the cause of the break up of subtropical Sc into the trade-wind Cu regime. However, such a mechanism seems a gross simplification: a number of different mechanisms are involved in the TKE balance and a much more careful evaluation is required before such a process could be shown to be operative. For example neither of the conditions constrain the liquid water in the cloudy layer - values of 0.1g/kg are deemed to be as unstable as those with 1g/kg. Recent observational evidence also suggests that long lived cloud sheets can exist even in conditions where i) is well satisfied (see lecture 10).

4.5 SUMMARY

The physical processes described above which are believed to be important in determining the evolution of layers of Sc are illustrated schematically in Fig 12. The processes themselves respond quickly to imposed changes (related to the turbulence adjustment time, typically some tens of minutes) and are therefore reflect local conditions. However, the flux gradients associated with these processes are such

that they tend to alter the mean state (eg the gross properties of the cloud) on timescales of a few hours. Advective effects controlled by the synoptic scale flow (eg subsidence velocity, changing surface boundary conditions) will therefore in general be equally important in determining cloud layer development. For this reason alone, it is very unlikely that the gross cloud structure at any particular location is determined solely by local conditions.

4.6 STRATIFORM CLOUD MODELLING

A number of models of varying complexity have been developed recently. These may be broadly classified into three main types. In general, the simpler the formulation, the more must be assumed about the vertical turbulent structure.

4.6.1 BULK MODELS

These are the simplest type and are based on the prognostic equations for mean variables (eg θ_e, q_T) integrated vertically through the boundary layer. It is assumed that the shapes of the vertical profiles are self-similar and a known function of model variables. Best known are mixed-layer models in which the basic assumption is that conservative variables are independent of height throughout the depth of the boundary layer. This assumption is justified as long as the dominant turbulent length scale is of the order of the boundary layer depth (which may not always be the case according to Ref 5). Closure in these types of model requires a formulation for the entrainment velocity, usually made dependent on the TKE through a simplified integrated TKE balance.

Advantages:

i. Conceptually simple, yet allow interactions between all important physical processes to be included. Cause and effect are easily indentified.

ii. Computationally very efficient.

iii. Explicit representation of boundary layer height (cloudtop) and cloudbase.

iv. Vertical resolution is not restricted by a discete vertical grid. Very large inversion gradients are well represented by discontinuities.

v. Turbulent transport within the layer does not require explicit representation. These follow directly from heat and water budget considerations.

Disadvantages

i. Assumption that the shapes of the profiles remain fixed.

ii. Models are one-dimensional and implicitly assume small-scale horizontal uniformity. Broken cloud is therefore difficult to represent.

iii. Entrainment rates must be specified.

iv. They rely heavily on empirical assumptions and observational studies.

v. Only a limited range of quantities are predicted.

Examples: Refs 5 & 6

4.6.2 TURBULENCE CLOSURE MODELS

Here the boundary layer is resolved into a number of levels. Only the statistical properties of the turbulence are calculated, however these require additional assumptions concerning the higher-order statistical moments. Closure assumptions with varying degrees of sophistication have been used, from eddy-diffusivity formulations to 2nd and 3rd order schemes.

Advantages

i. Any type of statistically homogeneous boundary layer can be modelled.

ii. Computing requirements are moderate (10,000 times less than for LES : see 4.6.3).

iii. All turbulence generating processes can be included.

Disadvantages

i. The range of validity of the necessary closure assumptions is uncertain and not easily tested.

ii. Prior knowledge is assumed to relate the dominant turbulence length scales to model parameters.

iii. Vertical resolution may be inadequate near cloud top.

iv. Empirical relationships relating sub-grid condensation and fractional cloudiness are required.

Examples: Ref 10

4.6.3 LARGE EDDY SIMULATIONS (LES)

These solve the full equations of motion on a 3D grid small enough to explicitly resolve the main energy containing eddies throughout the boundary layer. The grid must be small enough (<50m) to ensure that the sub-grid motions (which must still be parametrized) lie in the inertial subrange. These eddies have relatively little energy and their properties are relatively well understood, so few a priori assumptions about the nature of the turbulent flow are necessary.

Advantages

i. Gives explicit, very detailed information on nearly all aspects of the flow. Detail is comparable with that provided by observations.

ii. No restrictions on the type of conditions eg very unsteady situations can be successfully modelled.

iii. Many different statistics can be computed directly from the solutions.

Disadvantages

i. Computationally very expensive, so very few simulations have been carried out.

ii. The small grid size necessarily restricts the domain size to a few km.

iii. Long averaging times are necessary to produce stable statistics.

iv. Only rudimentary attention to cloud physics has been possible so far.

v. Extremely fine resolution (10m) appears to be necessary to resolve details near cloud top. This is necessary if entrainment is to be studied.

Examples: Refs 11 & 12

REFERENCES

1. Nicholls S 1987 A model of drizzle growth in warm, turbulent, stratiform clouds. QJRMS, 113, ??-??

2. Roach W T & Slingo A 1979 A high resolution IR transfer scheme to study the interaction of radiation with cloud. QJRMS ,105, 603-614.

3. Slingo A & Schrecker H 1982 On the shortwave properties of stratiform water clouds. QJRMS, 108, 407-426.

4. Slingo A, Nicholls S & Schmetz J 1982 Aircraft observations of marine stratocumulus during JASIN. QJRMS, 108, 833-856.

5. Turton J & Nicholls S, 1987 A study of the diurnal variation of stratocumulus using a multiple mixed layer model. QJRMS, 113, ??-??.

6. Lilly D 1968 Models of cloud-topped mixed layers under a strong inversion, 94, 292-309.

7. Minnis P & Harrison E F 1984 Diurnal variability of regional cloud and clear sky radiative parameters derived from GOES data. J Clim Appl Met, 23, 993-1051.

8. Nicholls S & Turton J 1986 An observational study of the structure of stratiform cloud sheets: Part II: Entrainment. QJRMS, 112, 461-480.

9. Randall D A 1980 Conditional instability of the first kind, upside down. JAS, 37, 125-130.

10. Bougeault P 1985 The diurnal cycle of the marine stratocumulus layer: A higher order model study. J A S, 42, 2826-2843.

11. Deardorff J W 1980 Stratocumulus-capped mixed layer derived from a three dimensional model. Bound. Layer Meteor, 18, 495-527.

12. Moeng C H 1987 Large eddy simulations of a stratus-topped boundary layer. Part I: Structure and budgets. JAS, 43, 2886-2900.

13. W M O 1986 Report of the JSC/CAS workshop on modelling the cloud-topped boundary layer. WMO/TD No. 75, WCP 106.

Some points to think about

1. What changes do you think you would see in the lower cloud if a sheet of thick altostratus was advected over the stratocumulus deck seen in Fig 3?

2. How many of these processes are likely to be important in the maintainance of cirrostratus? What else would need to be considered in this case?

3. What are the differences between these cloud layers and thick fogs?

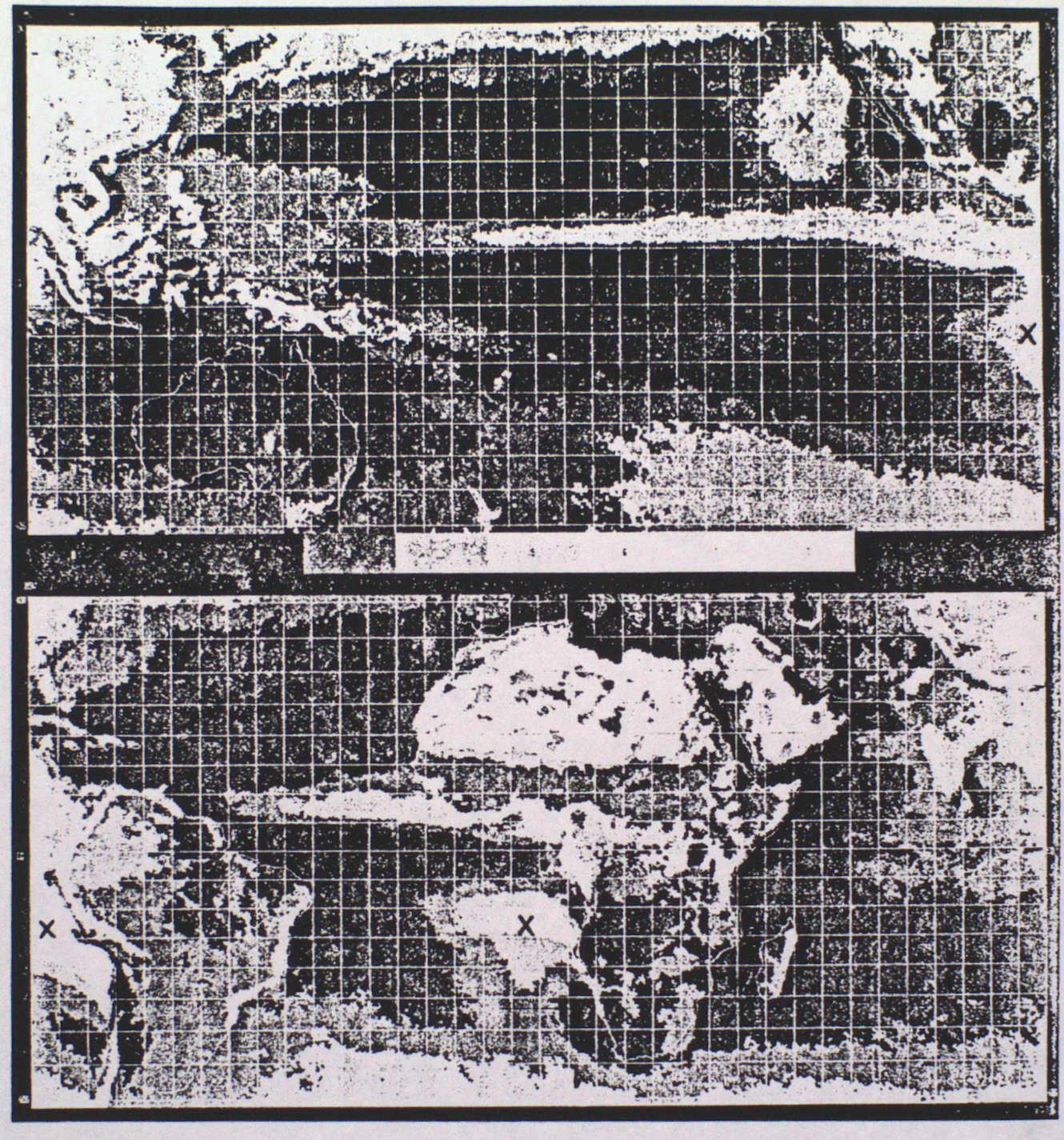

Mercator Satellite Relative Cloud Cover, 1400 Local, 40° N to 40° S, Mean Octas, Semiannual, June through November 1967-1970.

Fig 1. Areas of persistent low-level stratiform cloud show up as the light areas denoted X. Taken from 'Global Atlas of Relative Cloud Cover 1967-1970', NOAA & AWS (1971).

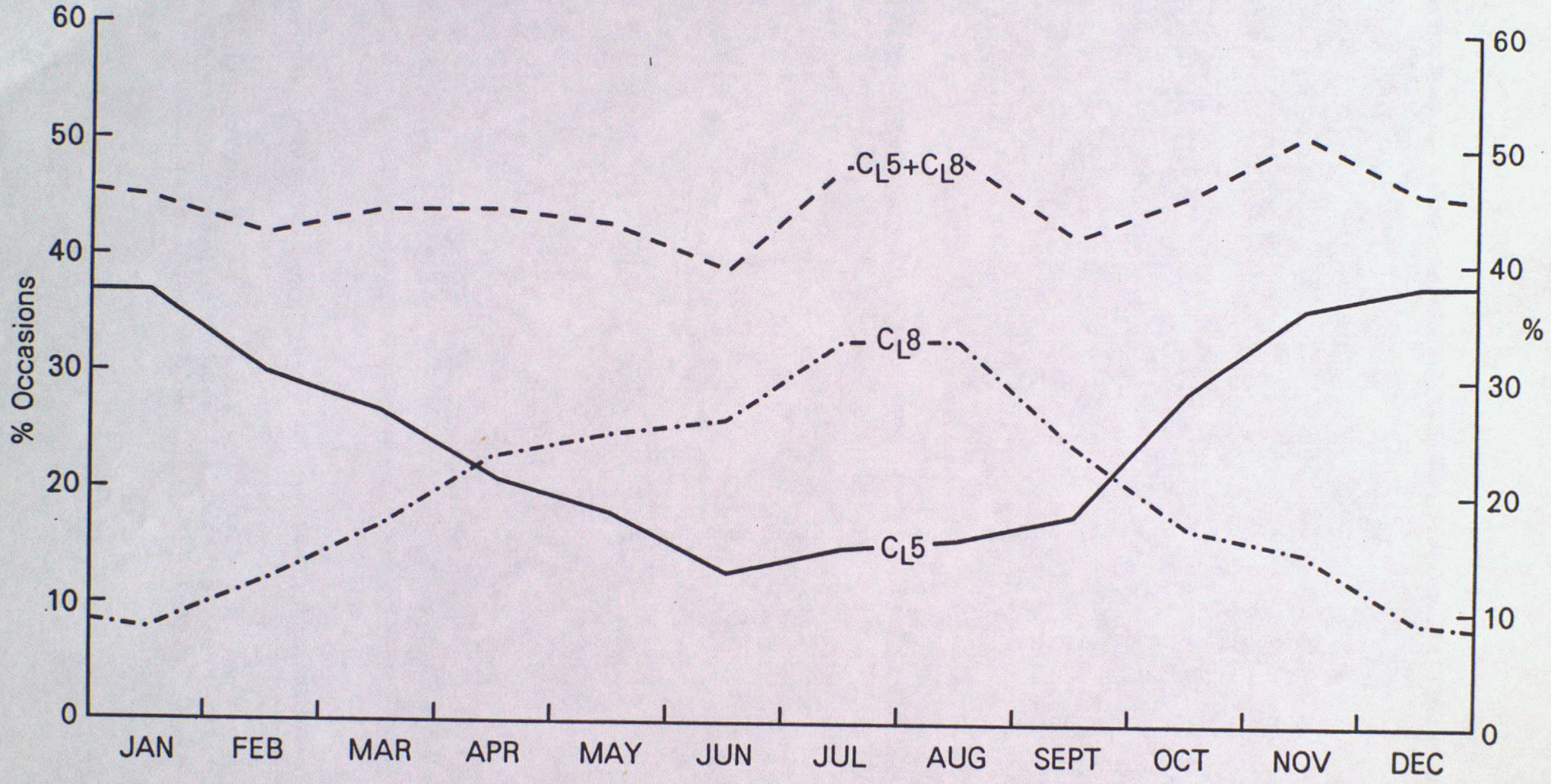

Fig 2 Frequency of occurrence of low cloud types C_L5 (stratocumulus) and C_L8 (cumulus rising into stratocumulus) in daytime observations at a typical UK station. Data are monthly averages.

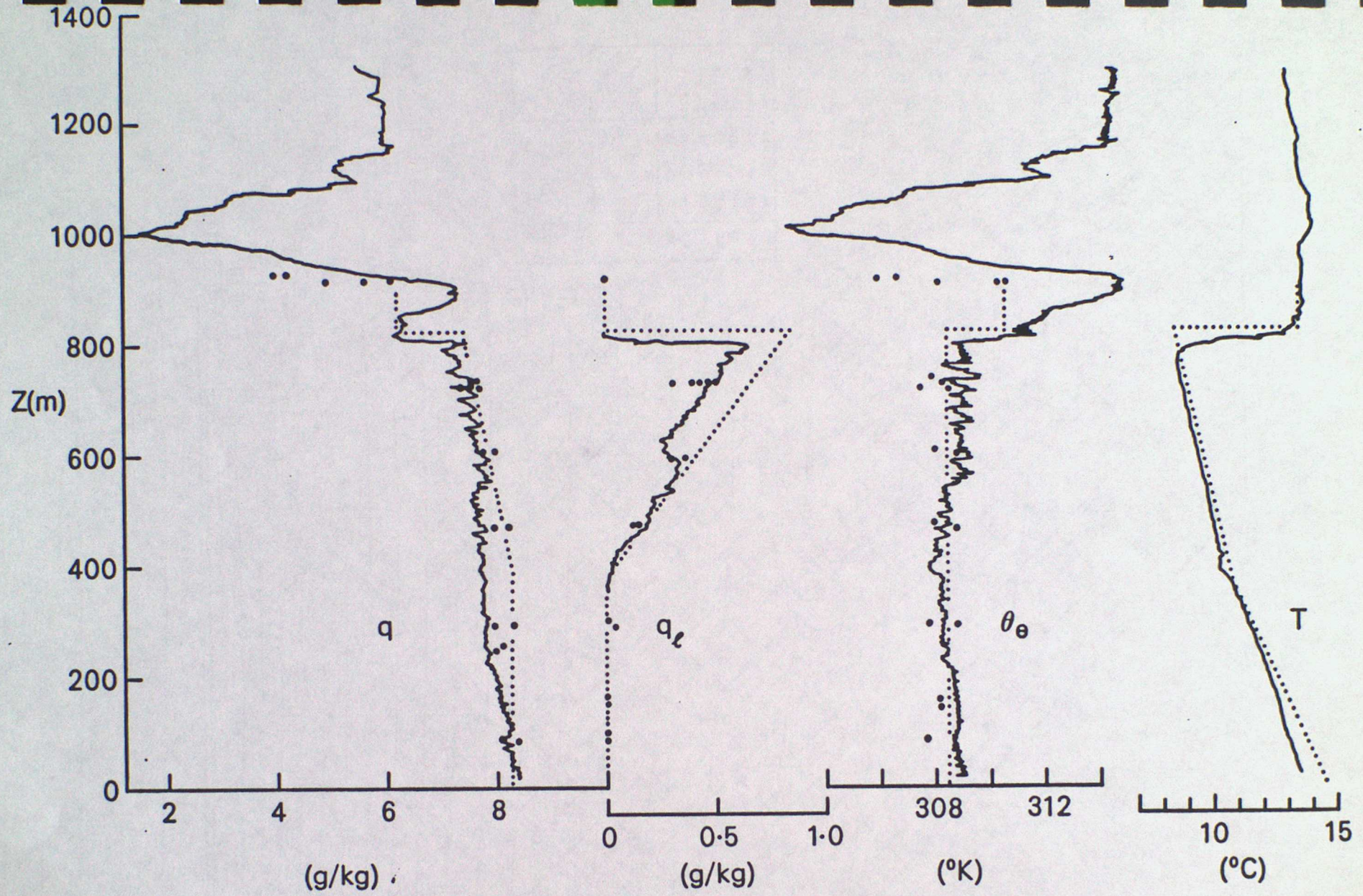

Fig 3a Vertical structure measured by the MRF C130 on a slow descent at 1100 GMT on 22 July 1982 (solid lines) together with horizontal run averages (•) and the representation used in a mixed layer model (dotted).

Fig 3b. The Hemsby sounding at 00Z 23 July 1982.

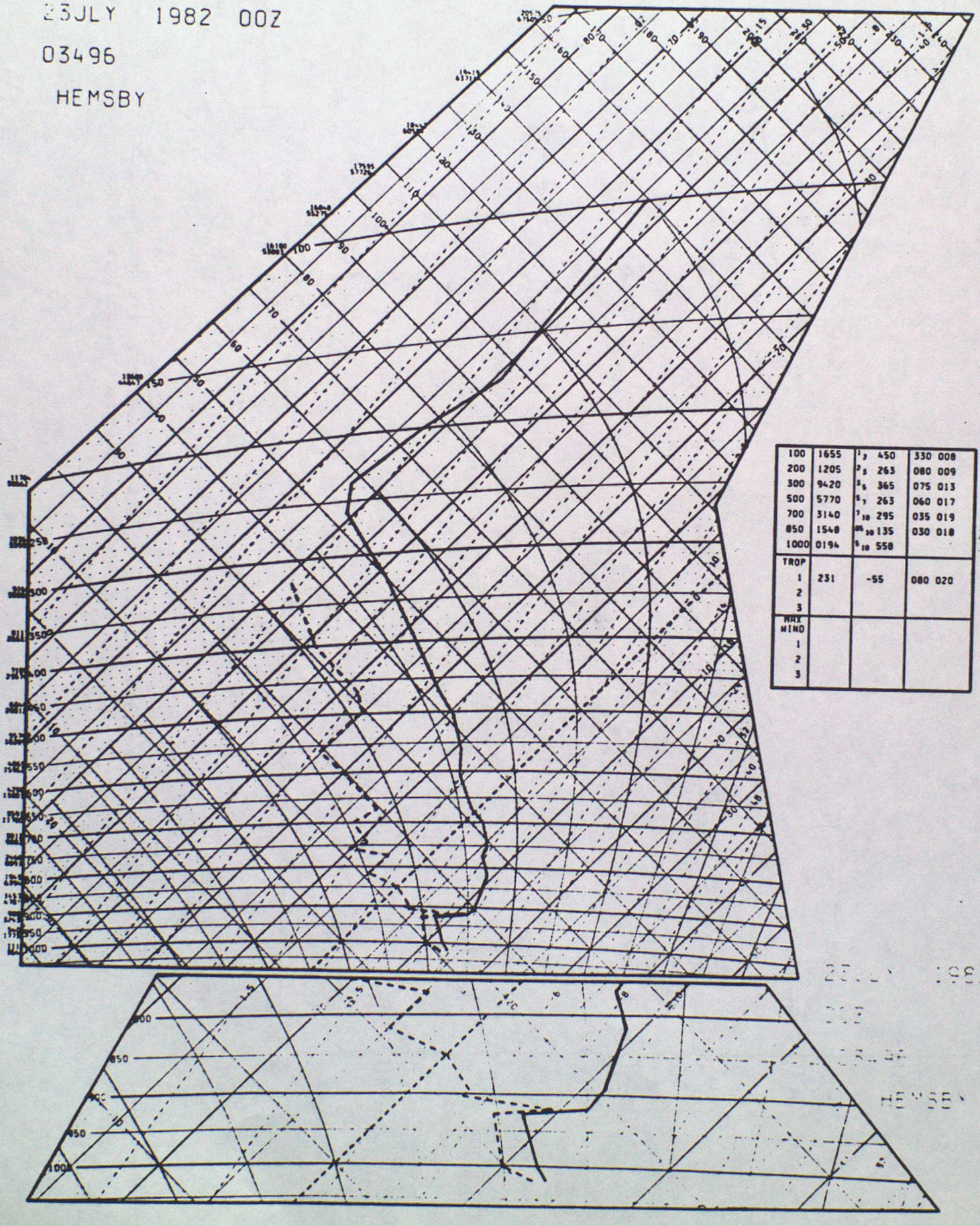

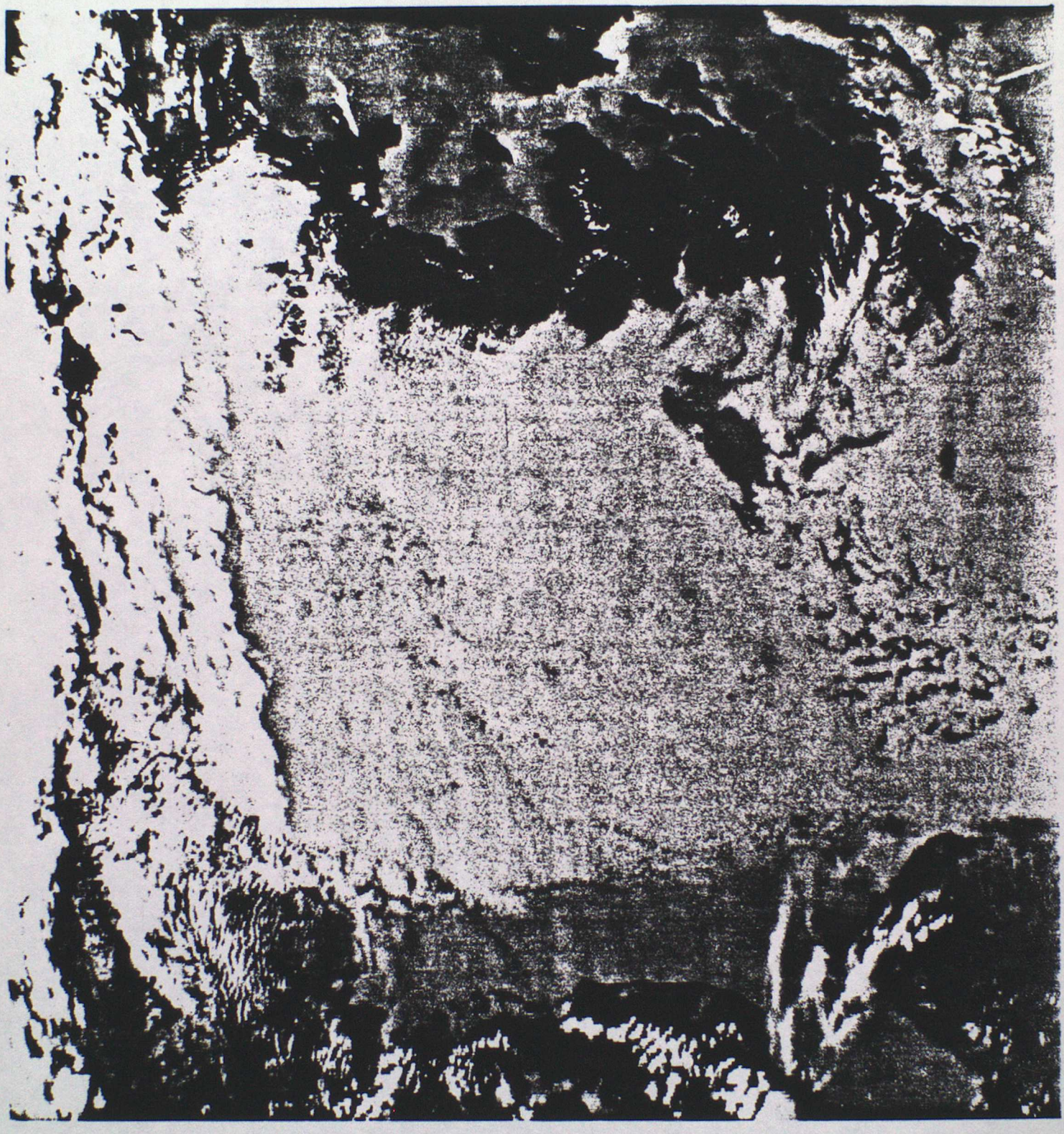

Fig 4. AVHRR IR image of cloud layer in the North Sea (cf Fig 3) taken at 1441 GMT on 22 July 1982.

Fig 5. Typical convective cellular patterns seen in the tops of stratocumulus some 10,000ft below. A low sun angle enhances the contrast. The larger cells are a few km across.

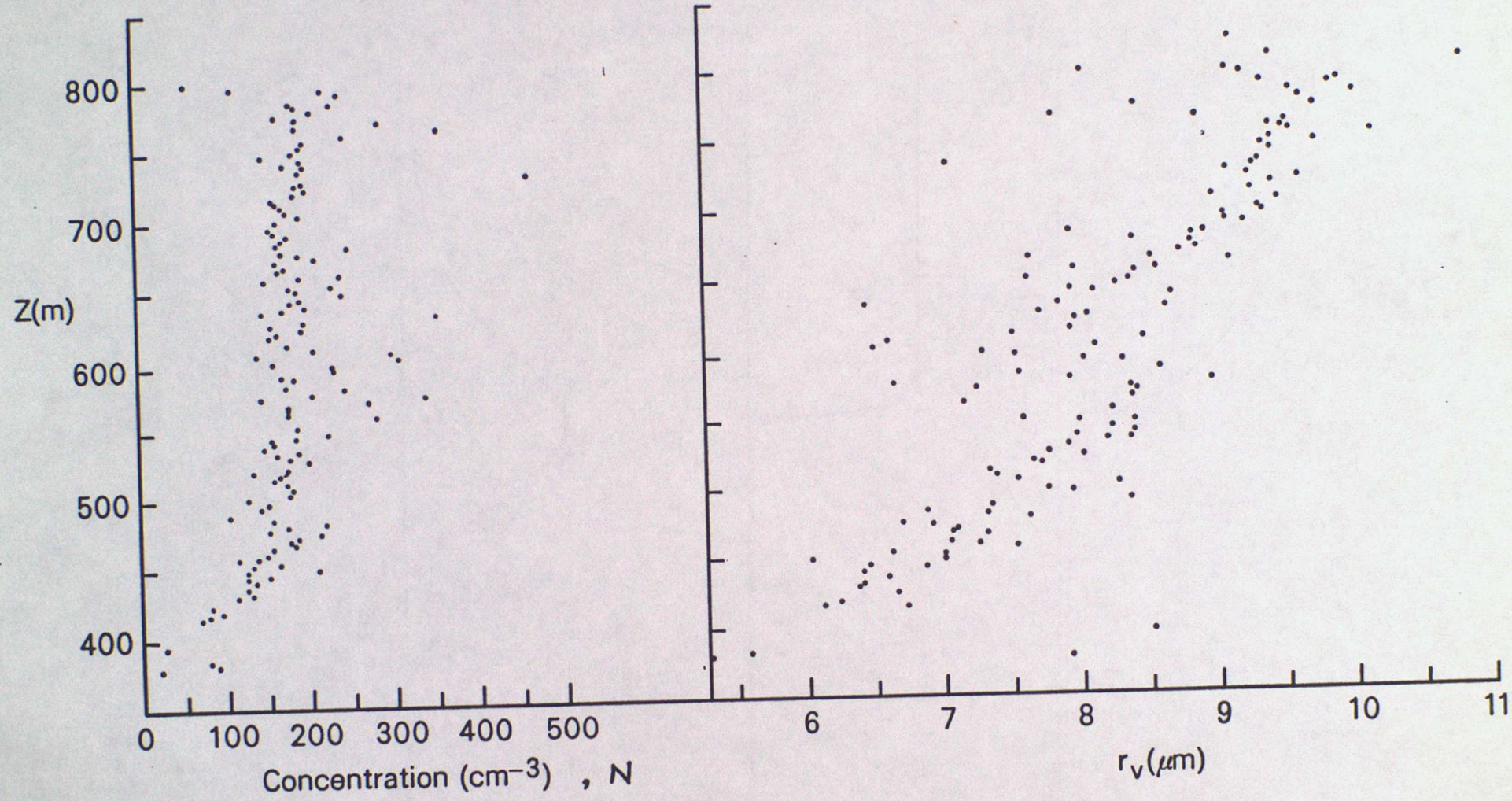

Fig 6 Variation of droplet concentration and mean volume radius, r_v, with height on the same descent as Fig 3. Each point is a 1s average.

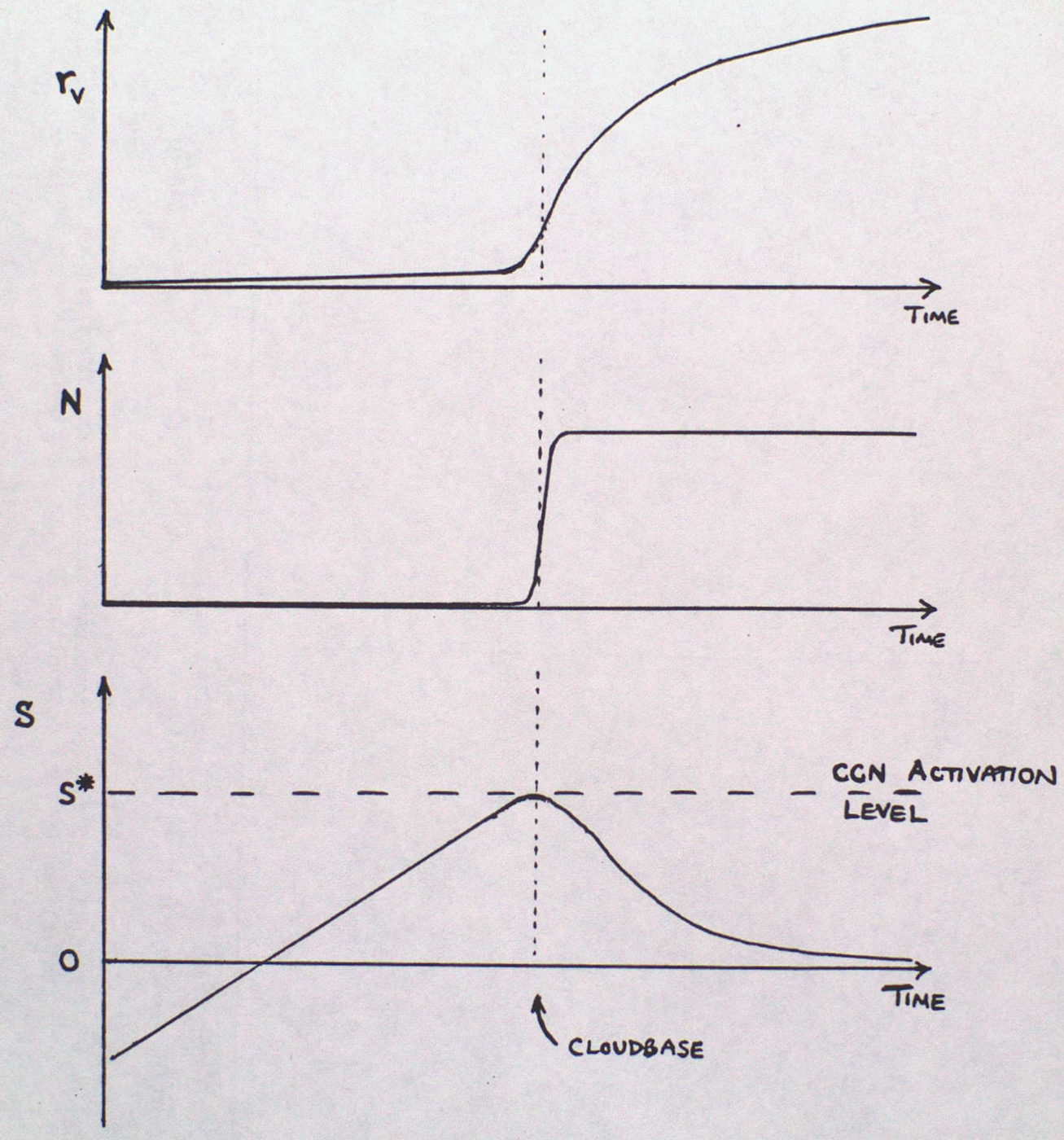

Fig 7. Schematic variation of supersaturation, S, droplet concentration, N, and mean volume radius, r_v, as a function of time in a steadily rising parcel as it passes through cloud base.

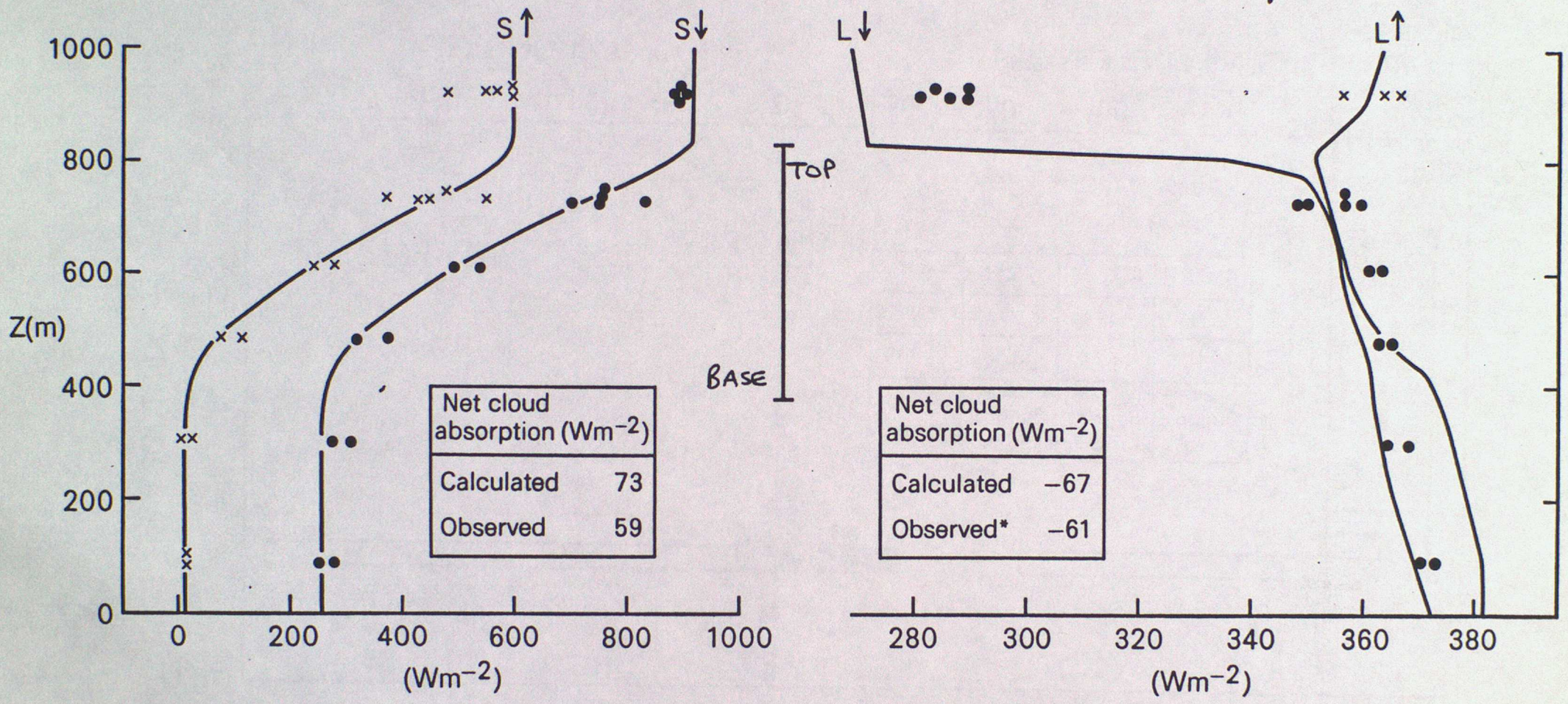

Fig 8 Measured average radiation fluxes from horizontal runs, • (S↓, L↓) and x (S↑, L↑) with theoretical solutions shown by the curves. The extent of the cloud layer is shown by the vertical bar.
* In calculating this value, L↑ beneath cloud is assumed equal to the computed value.

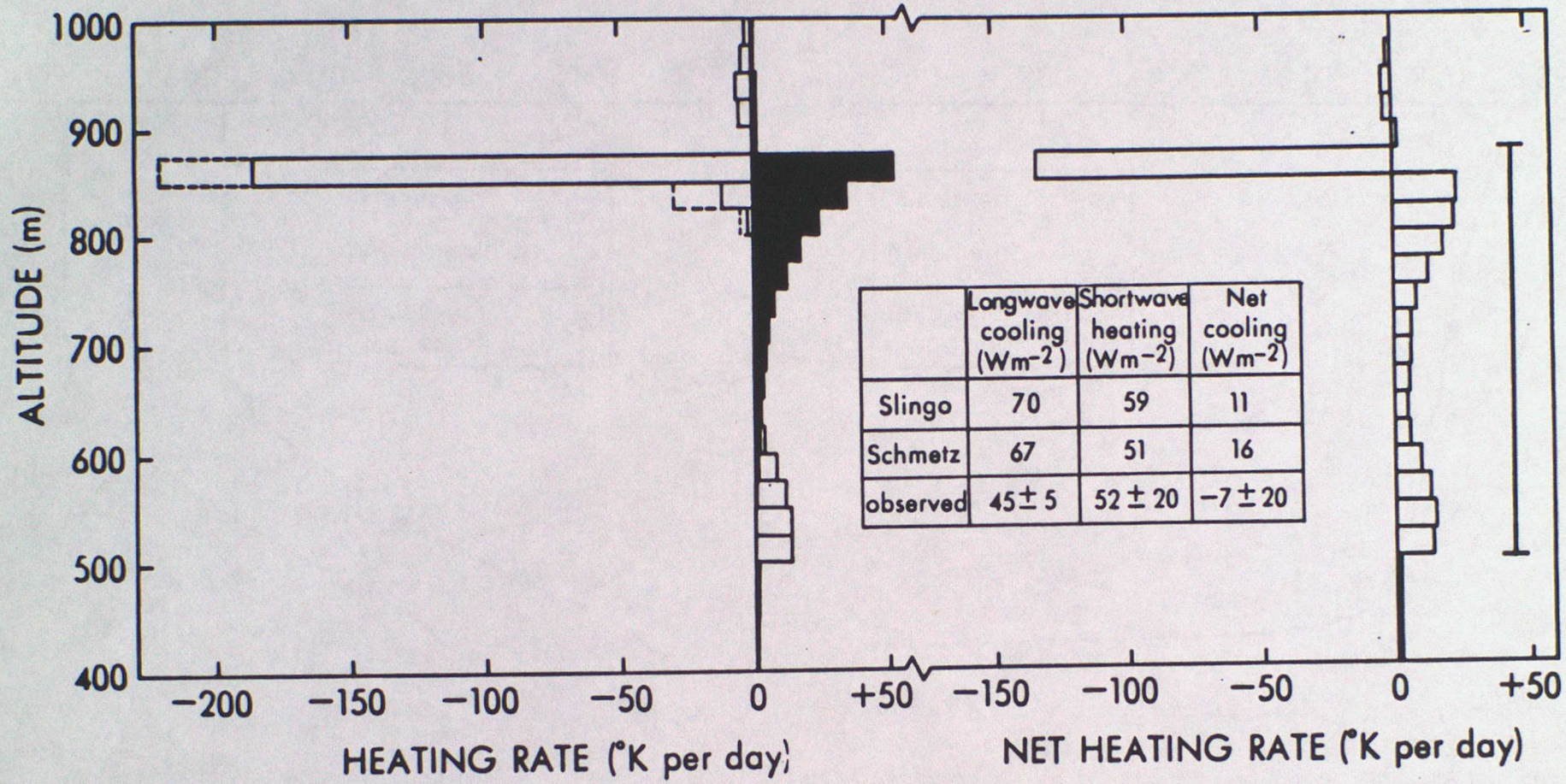

Fig 9. Heating rates derived by differentiating fluxes shown in Fig 8, ie $dT/dt = - d (S\uparrow - S\downarrow + L\uparrow - L\downarrow) / dz$. Two different theoretical calculations and observed values are also shown. The cloud layer is again indicated by the vertical bar.

FIG 10a MEAN DIURNAL VARIATION OF CLOUD AMOUNT (C) AND TEMPERATURE (T) FROM GOES, NOV 1978 (FROM MINNIS & HARRISON, 1984)

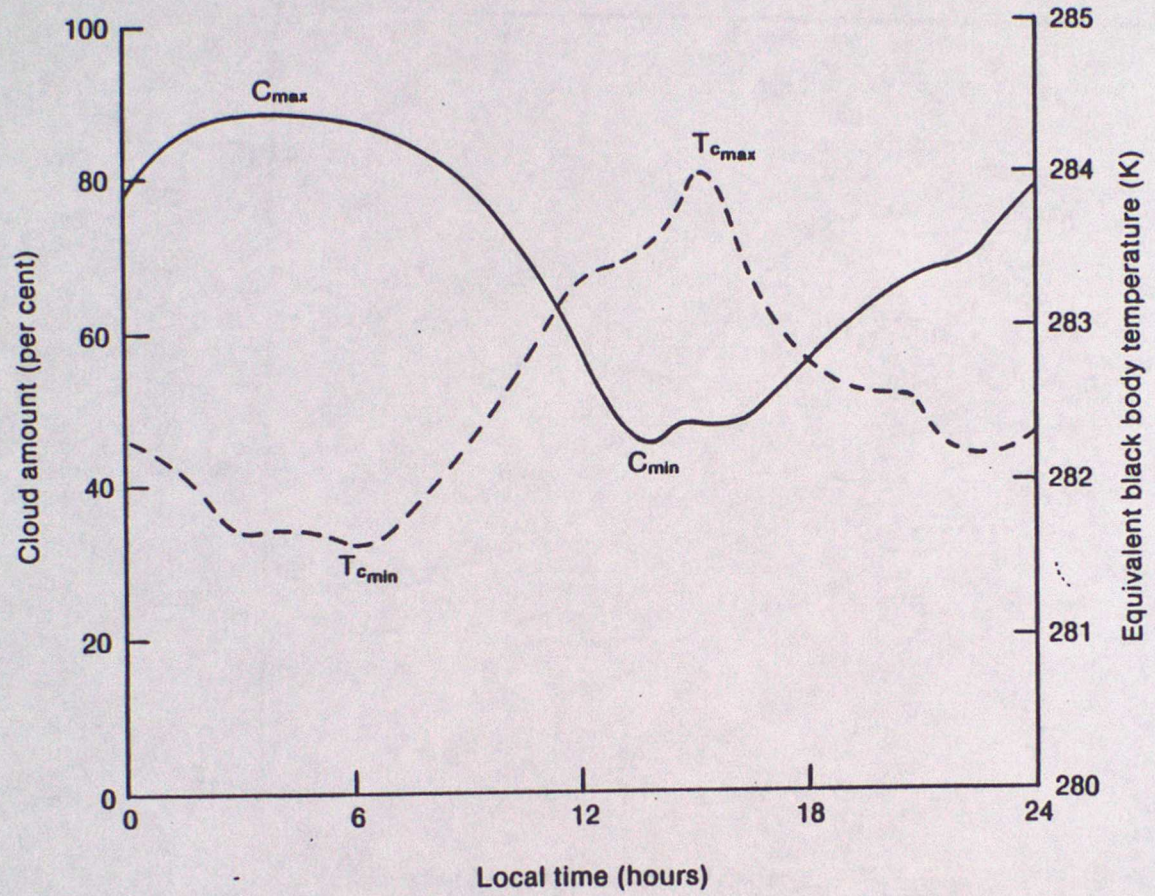

POSITION : 21°S, 86°W

Fig 10 b

SEASONAL DIURNAL VARIATION OF MONTHLY MEAN CLOUD COVER FROM GOES

LAT. = 23.6°S, LONG. = 78.8°W

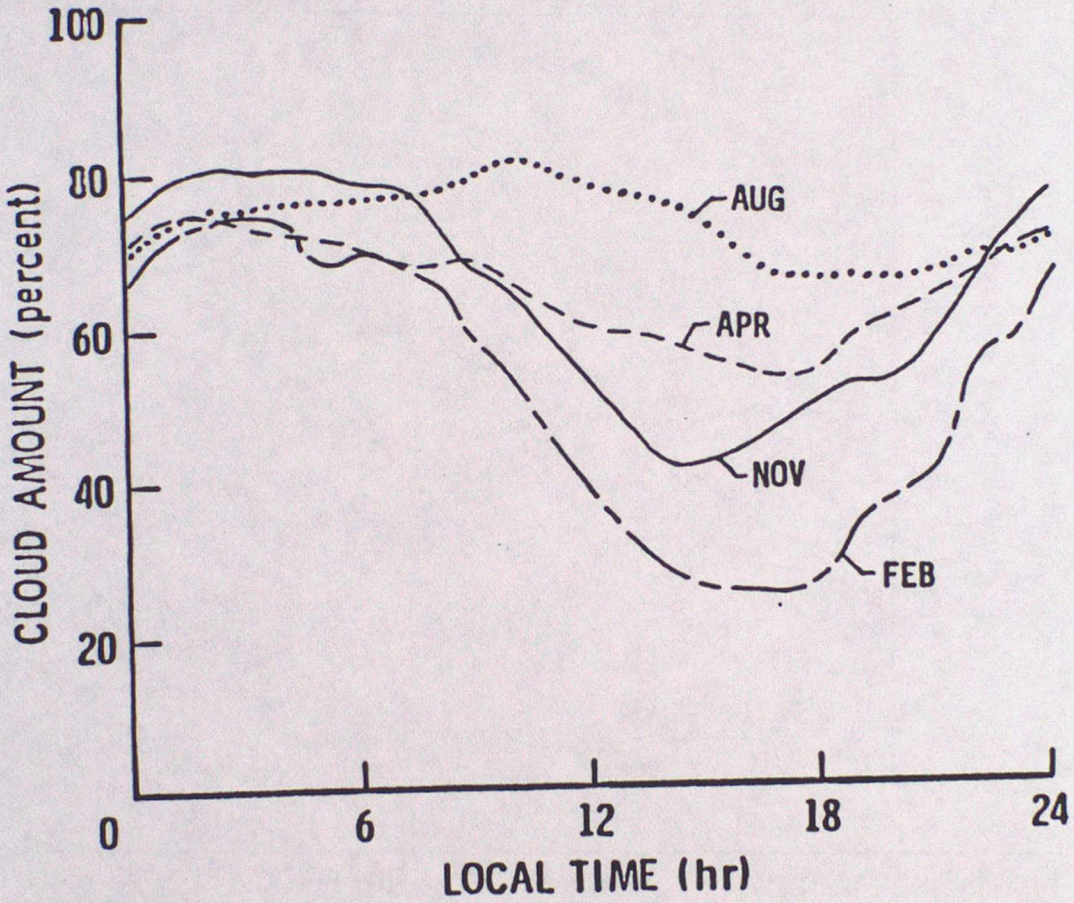

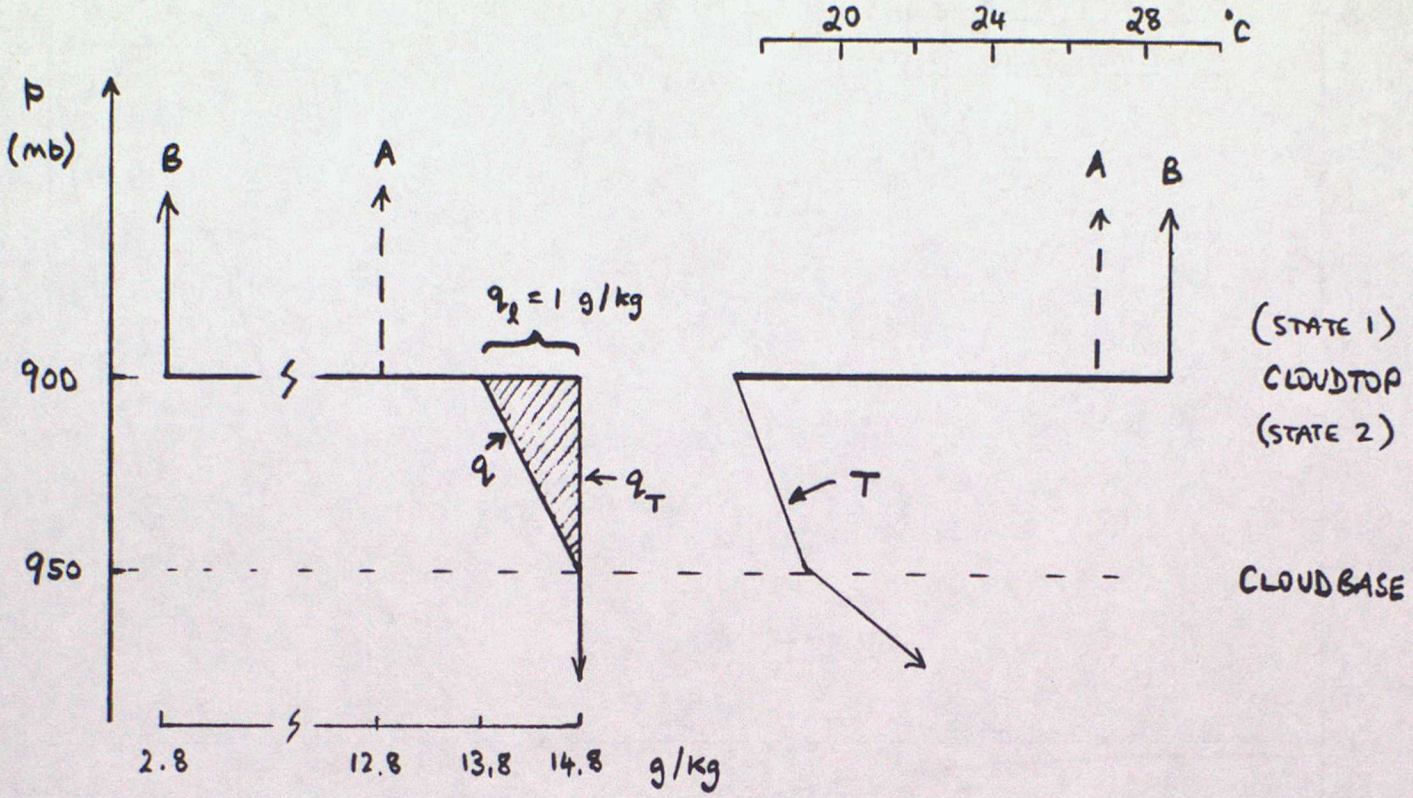

Example		θ_e (K)	q_T (g/kg)	θ (K)	q (g/kg)	q_ℓ (g/kg)	θ_v (K)
A	State 1	339.0	12.8	307.0	12.8	0	309.4
B	State 1	316.0	2.8	309.0	2.8	0	309.4
	State 2	334.0	14.8	299.5	13.8	1.0	301.7
A	Δ (1-2)	5	-2				7.7
B	Δ (1-2)	-18	-12				7.7

ie	Example	$\beta\Delta\theta_e$	$\theta\Delta q_T$	Condition satisfied ?
	A	2.5	-0.6	No
	B	-9.0	-3.6	Yes

Fig 11a. Definition sketch of the thermodynamic states (1 & 2) in examples A and B discussed in the text.

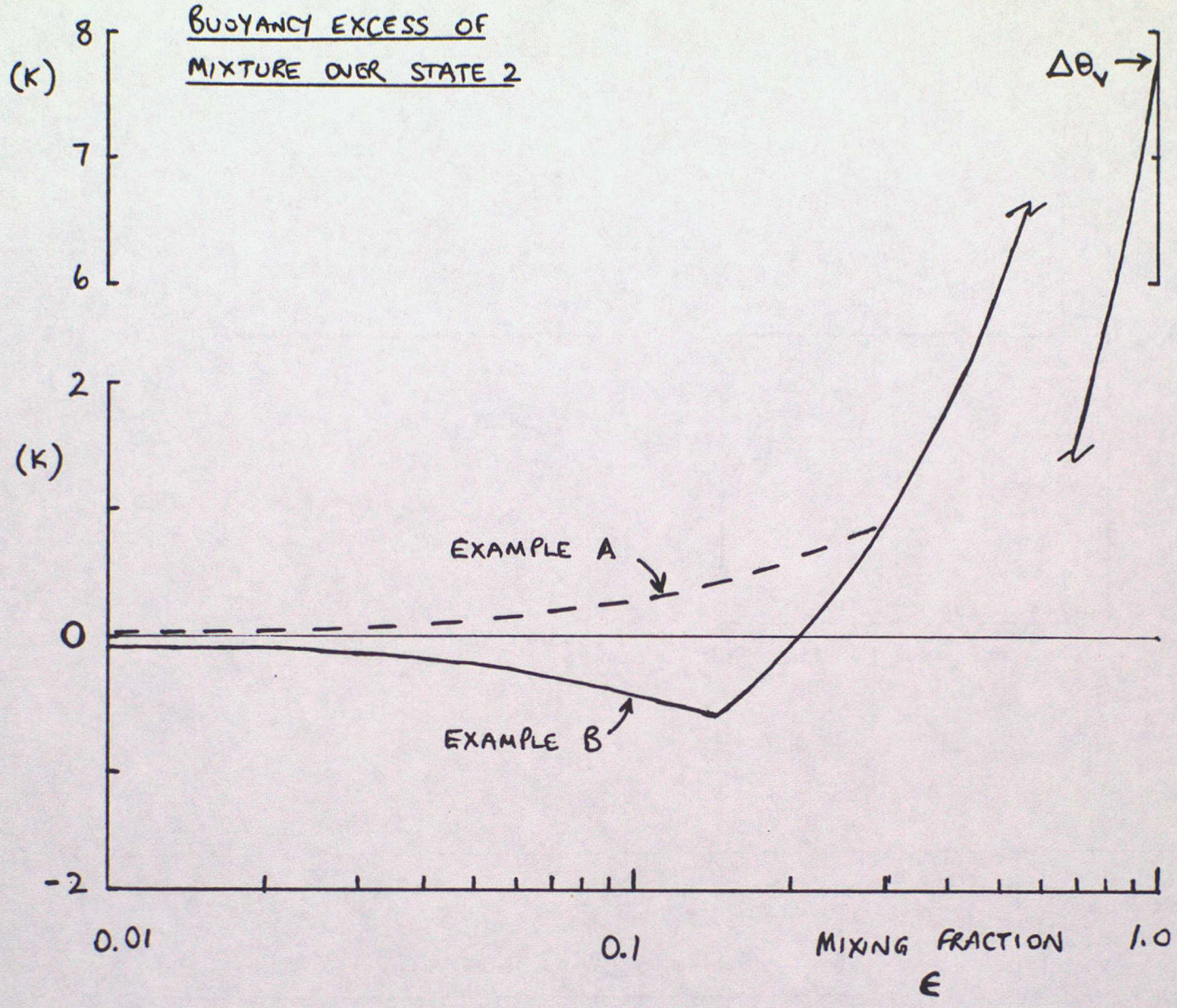

Fig 11b. Buoyancy excess (expressed as a virtual temperature difference) of the mixture over state 2, expressed as a function of mixing ratio, ϵ.

Only when the condition referred to is satisfied (Example B), do negative values occur.

When $\epsilon=1$ and there is no mixing, the buoyancy excess is simply $\Delta\theta_v$.

Fig 12. Summary of the important physical processes occurring in low-level stratiform cloud layers.

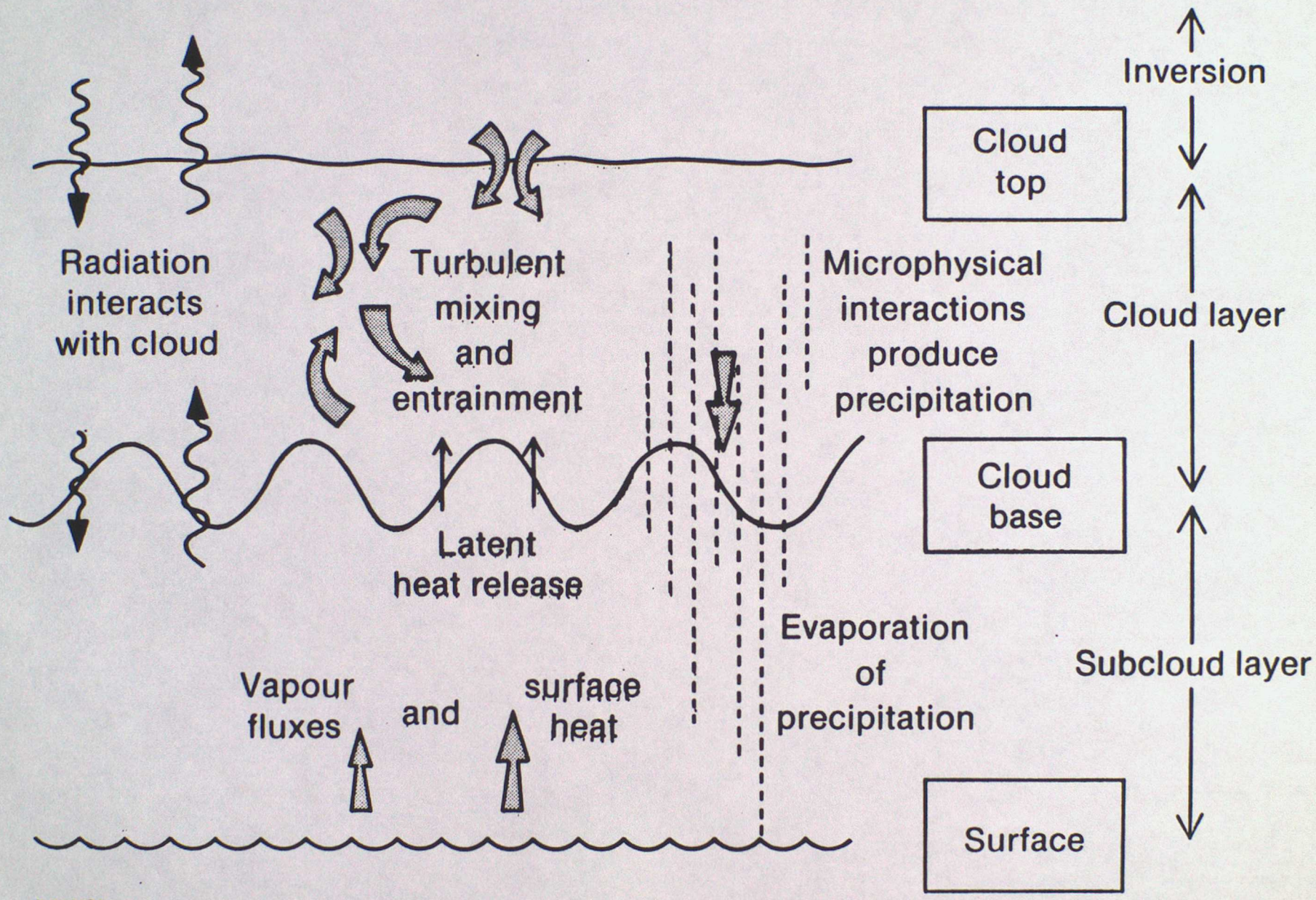

DO 3938

LECTURE 5: CLOUD PHYSICS INSTRUMENTATION

BY S NICHOLLS, MET O 15

5.1. INTRODUCTION

In the past decade, the main emphasis in cloud physics research has swung away from laboratory based investigations of simple particle interactions to observational studies of real clouds. This revolution has come about because of the development of new measurement techniques. This lecture is intended to give a basic appreciation of these techniques and will describe some of the cloud physics instrumentation currently in use, concentrating on basic operating principles and pointing out the limitations of each device. Examples of the types of data obtained will also be given.

The scope will be restricted to in situ techniques only; important remote methods eg radar, lidar, which have played a large role in cloud physics research will not be considered (these must often be calibrated using in situ measurements anyway). The increasing use of satellite data will be described in Lecture 10. Methods suitable only for laboratory use will also be omitted. Finally, the lecture is biased towards those devices operated by Met O 15 which is an extensive subset of those currently available, covering a wide range of measurements.

Measurements may be divided into two types:

i. Microscale measurements in which individual particles are examined yielding shape, size, composition, number density information etc.

ii. Integrated or bulk measurements which refer to volume averaged properties (eg specific liquid water or ice content, rainfall rate, temperature or humidity mixing ratio).

The different scales on which these measurements are made usually demand very different measurement techniques.

Another important consideration is the platform from which the observations are to be made. Although measurements can be made from the ground, tethered balloons or towers, the height limitations, restricted sampling capability (waiting for the cloud to travel past fixed sensors) and the limited perspective gained from a fixed ground position mean that most observations are now made from aircraft. This immediately presents a number of problems:

i. Exposure. How to measure an uncontaminated sample while moving at 100 ms^{-1} in something very large. The inertial sorting of particles in an accelerating (curved) flow is a potential problem, creating concentration enhancements or shadow zones (Ref 1).

ii. Response. If an average cloud droplet is characterised by a length

scale of ~10μm, its transit time relative to the aircraft is $\sim 10^{-7}$s.

iii. Artificial modification. The passage of a powered aircraft through a cloud might significantly alter the cloud structure either by the amount of turbulence generated in its wake or by the ejection of exhaust gases and particulates (eg Ref 2).

iv. Environment. Measurement techniques must be impervious to wetting. Icing conditions are particularly difficult.

These are usually overcome by carefully siting equipment in exposed positions in relatively undisturbed airflow, calculating correction factors as necessary (i), stringent criteria in instrument design (ii, iv) and by paying close attention to sampling strategy, flight planning and navigation (iii).

5.2. MICROSCALE MESUREMENTS

Here we are essentially interested in single particle counters. The particle sizes which are of interest vary from 0.1μm to a few mm (all subsequent particle dimensions refer to particle radius or 1/2 maximum dimension for non-spherical particles) as shown in Fig 1. Dealing with the smallest first:

5.2.1 CCN Counters:

Recall that cloud droplets grow initially by condensation onto pre-existing cloud condensation nuclei (CCN). However, only a small fraction of the total aerosol concentration act as CCN. This is because a small fraction become activated at very low supersaturations. Any subsequent excess water vapour is preferentially taken up by these drops, maintaining the supersaturation at a very low level, and preventing the activation of further nuclei.

In more detail, recall that the equilibrium saturated vapour pressure (s.v.p) over a solution droplet of radius r, denoted $e'_s(r)$, is given by the eqn shown in Fig 2 where $e_s(\infty)$ refers to the equilibrium s.v.p over a plane, pure water surface under similar conditions. The 'curvature term' represents the increase in s.v.p over a curved rather than a plane surface, the 'solution' term shows the reduction in s.v.p caused by the solute. Together, these result in the typical variation of equilibrium s.v.p shown in Fig 2 (values for a,b may be found in Ref 3, p62).

At small r ($r<r^*$), the solution effect dominates and a droplet can be in equilibrium at relative humidities (RH) less than 100%. Note that a droplet is stable if the RH is constant. If r is slightly increased, its equilibrium s.v.p is also increased, so with the RH fixed, the droplet must evaporate back towards its original size. Conversely, the RH must be increased if the droplet is to grow. If the RH continues to increase, the droplets will continue to grow, in equilibrium with the

current RH until $S = S^*$, when $r = r^*$. Once a droplet grows beyond r^*, its equilibrium s.v.p is less than S^*, vapour diffuses towards the drop and it will continue to grow without any further increase in the supersaturation. In fact the growth of the drops will generally quickly lower the supersaturation by taking up the available water vapour. Growth will continue until the s.v.p falls below the equilibrium value again.

Droplets smaller than r^* grow only in response to RH changes and are termed 'haze particles'. A condensation nucleus is said to be 'activated' once it has grown to a size r^*, when it can grow under any supersaturated conditions (ie $0<S<S^*$) to form a cloud drop.

The value of S^* depends on the properties of the condensation nucleus: decreasing the amount of solute increases S^* (very small pure water drops need very high supersaturations to remain stable). The number of nuclei which will be activated in incipient cloud formation therefore depends on the nature of the CCN and the degree of saturation achieved. Since the latter is also a function of the cloud dynamics, the number of nuclei activated as a function of supersaturation must be known if the evolution of the droplet spectrum is to be modelled. This is known as an activation spectrum and is a prerequisite for detailed calculations of droplet growth. In real clouds, $S < 1\%$, so a repeatable method of maintaining small supersaturations is required to make measurements of the activation spectrum.

The most common method is to use a thermal gradient diffusion chamber (TGDC) which uses the principle illustrated in Fig 3. Two highly conducting, wet surfaces are maintained at slightly different temperatures. In steady state conditions, diffusion will maintain linear temperature (θ) and humidity (q) gradients (eg since $d\theta/dt = K_\theta d^2\theta/dz^2 = 0$ and K_θ is not a strong function of θ, then $d\theta/dz$ = constant. Similarly for q). However, q_{SAT} varies non-linearly with θ and if both plates remain saturated, $q > q_{SAT}$ in the centre of the chamber as illustrated (Fig 4). In fact S varies parabolically with z, $S_{MAX} \propto \Delta\theta^2$ and $S_{MAX} \propto 1/\theta$ (Ref 4). Small constant supersaturations can thus be maintained by altering $\Delta\theta$. For example, if z=1cm, θ=20°C and $\Delta\theta$=3K, then S_{MAX} =0.4%.

If a sample is introduced into the chamber, some of the CCN will be activated and grow within a few seconds to several microns. They will then settle out. The number of drops larger than, say, 1um in the centre of the chamber will initially increase and then decrease as the drops fall out (see eg Fig 4). The peak number of drops in the chamber may be measured either directly or by light scattering techniques and is directly related to the number of activated nuclei. The complete spectrum may be built up by repeated measurements with different $\Delta\theta$'s. An example is shown in Fig 4.

Limitations

i. S must exceed 0.1-0.2%, otherwise drops do not grow sufficiently large sufficiently quickly to be distinguishable from haze droplets and some drops may sediment out before

others have had time to grow.

ii. If the number of activated drops is very large (>1000/cc), the water vapour supply in the centre of the chamber may be temporarily depleted leading to undercounting.

iii. Each measurement at each supersaturation takes at least a minute to perform, so an activation spectrum is built up only slowly. This may be overcome, at the expense of simplicity, by designing a chamber in which the boundary temperature (and therefore the supersaturation) varies with distance while a continuous flow of sample air is maintained. The growth of drops as a function of distance along the plate allows the activation spectrum to be recovered (eg Ref 5).

5.2.2 Small droplets, 1-25μm

The vast majority of cloud drops lie in this range.

5.2.2.1 Impact devices: Now largely superseded, these were virtually all that were available until the mid 70's. These all involve the inertial capture of drops on suitably prepared surfaces followed by microscopic examination. Many different methods were used (see Ref 6) with slides or films exposed for short times (fractions of a second) to the airflow. Coverings of soot or MgO record particle impacts as craters proportional to particle size while an oily coating traps drops and arrests evaporation. 'Replication' uses a continuous tape coated with a 70μm-thick layer of Formvar (a plastic solution) in which particles are embedded. Drying the tape hardens the plastic and evaporates the encapsulated particles leaving behind a replica for later examination.

Limitations

i. All these methods suffer from the major disadvantage that the collection efficiency is strongly dependent on particle size because of inertial sorting.

ii. Particles may break up on impact.

iii. Craters are only proportional to particle size and require calibrating.

iv. Small samples are necessary to avoid double impacts.

v. Subsequent microscopic analysis is long and tedious.

5.2.2.2 PMS Forward Scattering Probe (FSSP)

Developed in the early 70's by Dr R Knollenberg in the US, these devices have almost entirely superseded impact methods. The basic principle is to measure light scattered in the forward direction by

single particles. A number of similar devices are now also available from other sources, and the technique has been extended to cover size ranges in the interval $0.1\mu m < r < 45\mu m$.

Fig 5 shows a schematic layout of the FSSP. Light from a 5mW CW He-Ne laser ($0.63\mu m$) is focussed to a diameter of $\sim 200\mu m$ at the centre of the sampling aperture through which air passes in a direction perpendicular to the plane of the diagram. The collection optics only accepts light scattered between 4° and 15°. In this range, small water droplets scatter light with an intensity which is approximately proportional to r^2. Fig 6 shows this intensity as a function of drop size computed using Mie theory assuming the scatterers are spherical, pure water drops. If the sampling volume is made so small that it contains only one drop at any time, measurements of the scattered light intensity enable water drops to be counted and sized automatically.

In practice, the scattered intensity depends upon

i. Particle size and shape

ii. The optical properties of the particle material

iii. The location of the particle within the beam

iv. The optical properties of the instrument (beam intensity, uniformity etc).

Particles are assumed to be perfectly spherical and composed of pure water. The effects of iii. and iv, are minimized by restricting the sampling volume. This is achieved in two ways.

i. The scattered light passes through a beam splitter (Fig 5) to two detectors, one of which has an annular mask. Particles in focus (those within $\pm 2mm$ of the object plane) form an image on the central dump spot, so only out of focus images will register. These are rejected.

ii. The transit time of the particle through the beam is also measured. If this is less than average, the particle must have passed through the edge of the beam and is also rejected.

These two criteria govern the sampling volume: approx. 4mm by $0.62 \times (200\mu m)$ by $200\mu m = \sim 10^{-3}$ cc. Since particle concentrations are usually less than 1000/cc, the volume will usually contain only a single particle.

Advantages

i. Sample is relatively undisturbed.

ii. Produces a drop-size distribution ($0.5\mu m$ - $24\mu m$) in real time.

iii. Good time resolution because of short (0.1 - 10s) averaging

period.

iv. Good spectral resolution (15 size bins from 0.5μm - 1.5μm wide)

v. Data produced in computer compatible form.

Limitations

i. The sample volume/particle rejection criteria are not defined with sufficient accuracy to enable integrated quantities eg liquid water content to be obtained directly from the spectra.

ii. The sampling volume is an odd shape: 200μm (across) x 100m for a 1-sec averaged spectrum. This limits spatial resolution.

iii. Technique works for water drops only. Specular reflection from ice may give misleading counts and incorrect sizing.

iv. Mie peaks may produce ambiguity when sizing small (r<3μm) drops (see Fig 6).

Some examples of data obtained with the FSSP are shown in Fig 7. A large number of intercomparisons between these instruments and other techniques have now been published (eg Refs 7,8).

5.2.3 Larger particles, 20μm - 3mm

5.2.3.1 Impactors: As in 5.2.2.1 for droplets, these methods alsao work for larger particles. In addition, foil impactors have also been used for large (>100μm) particles where impact depressions in thin metal foil are measured (Ref 6, p606), however, the same disadvantages noted earlier remain.

5.2.3.2 PMS 2-D probes: These have replaced most of the earlier techniques. Since the particles measured are much bigger than those measured by the FSSP (see 5.2.2.2), essentially geometrical optical techniques are employed.

The beam from a 2mW CW He-Ne laser passes through the sample volume and illuminates a linear array of 32 photodiodes (Fig 8). Particles in the airflow enter the beam and shadow some of the diodes as shown. If the illumination of any diode falls below 50%, it changes state. By recording the state of the whole array many times during the particle's transit through the beam, a digital image is built up of the shadow (Fig 9).

The optics are arranged to magnify the shadow image, so the pixel size is governed by the actual diode spacing and the magnification. Two probes are needed to cover the entire range, the 'cloud' probe (12.5μm - 400μm) where the image of the diode spacing is 25μm and the 'precipitation' probe (100μm - 3mm) where the image of the diode spacing is 200μm.

If the ('clock') frequency with which the diode array state is

recorded is set so that particles move 25μm through the cloud probe beam between pulses (or 200μm for the precip. probe), the shadow will be recorded undistorted. If the airspeed is 100m/s, the cloud probe clock frequency must be 4MHz (0.5MHz for the precip probe). Thus each probe records a 2-D 'plan' or 'projected' view of each particle (Fig 10). (Other similar but simpler models simply record the maximum dimension or shadow area rather than the full image data.) To convert this to particle density information, the sampling volume must also be known. This is essentially the product of the sampling area normal to the airflow and the airspeed. The sampling area, A, is given by $A = F \times W$ where W is the diode array width and F the depth of field.

Were it not for diffraction effects, an object placed in a parallel beam of coherent light would generate a shadow which itself was rectilinearly propagating. The image of the shadow would be brought to a sharp focus in the focal plane of a lens wherever the shadowing object was situated. Theoretically, there would be an infinite depth of field limited only by the physical aperture of the probe (ie the distance between the probe tips). However, in the real world, diffracton effects cause the object's shadow to be in focus only when the object is confined to a more limited, size dependent, depth of field. Ref 9 has shown that providing a spherical object (of diameter D μm) is within $\pm 7.5 \times 10^{-5} D^2/\lambda$ of the object plane (where λ μm is the wavelength of the illuminating beam) there will be a reduction of intensity of at least 50% in the shadow and that the inferred size will be correct to within ±10%. The depth of field must therefore be calculated for each image. It is limited by the physical aperture for particles with r>80μm (cloud probe, aperture 6.1cm) or r>166μm (precip. probe, aperture 26.3cm).

Additional assumptions about the third dimension must be made for non-spherical particles if further statistics are to be calculated. Bulk quantities eg liquid water content, rainfall rate, radar reflectivity may also be derived if further assumptions are introduced eg particle composition, density etc. Some additional water phase information is made available by recording the depolarization of an initially plane polarized beam. The presence of ice tends to produce a larger signal.

Advantages:

i. As FSSP.

ii. Numerical particle-type recognition algorithms may be used with images of sufficiently large particles (>150μm), to automatically discriminate between different particle types.

Limitations:

i. The discrete detector size causes severe undercounting of particles shadowimg fewer than several pixels.

ii. The pixel size is fairly large compared to the image size, so shape information is often coarse. Distinguishing different particle types eg drops and lightly rimed ice particles, is

difficult.

iii. The sampling volume is dependent on measured particle dimensions. These are difficult to guage for non-spherical particles.

5.2.4 Other methods

5.2.4.1 High speed photography: Has been used, but the major limitation is the very small depth of field. Sampling volumes are therefore $\sim 10^{-3}$ cc which are unlikely to contain many particles although drops as small as 1um may be detected. Analysis is also time consuming.

5.2.4.2 Holography: Developed in Met O 15, this overcomes the depth of field limitation of conventional photography. Highly coherent light from a pulsed laser is passed through a diverging lens to illuminate the sampling volume (Fig 11). Light scattered by particles interferes with the original beam in the plane of the film forming a set of fringes. When the developed film is illuminated by a CW laser on the ground, the hologram acts as a diffraction grating and an image is formed as shown. This reconstructed image is that of a plane in the original sampling volume. Moving the hologram w.r.t the source of the illumination images another plane. Successive planes in a 3-D volume can therefore be scanned giving an extremely large effective depth of field (several 10's of cm) (Fig 12).

A high power Nd-YAG laser (1.06μm) is necessary to provide sufficient light to expose the hologram although a frequency doubling lithium iodate crystal is also used because sufficiently sensitive emulsions are not available in the near IR. A very short pulse length (20ns) effectively freezes particle motion and a 2ms camera shutter speed eliminates daylight fogging. The laser may be fired up to several times a second.

The use of divergent beams results in real images being substantially magnified. This varies as the hologram is moved away from the illuminating source during reconstruction (decreasing with increasing distance from the source). Using slightly different wavelengths during recording and reconstruction (0.53/0.63 μm) and a CCTV camera & monitor for reconstruction (23x) provides further magnification. Overall magnification factors up to several hundred may be obtained and particles from around 5μm to a few mm can be imaged.

Some examples of reconstructed images are shown in Fig 13 and Ref 10.

Advantages:

i. Delivers an instantaneous, compact sample of about 0.5l.

ii. Images are not limited by discrete pixel size giving much better edge/shape definition than the 2-D probes which facilitates ice/water classification and the detection of rime on large particles.

iii. Some information in the third dimension is available as different parts of the same image may be brought into focus by moving the hologram.

iv. The actual spatial positions of the particles are preserved, so relative separations may be measured and artefacts created by inertial sorting in the flow around the camera pod may be isolated and rejected.

Limitations:

i. Noise in the reconstructed images caused by beam non-uniformity on recording and film characteristics degrades the images and makes the detection of small drops difficult. It also eliminates the possibility of completely automatic image processing.

ii. The need for human pattern recognition makes analysis lengthy (nb it is not clear that the automatic processing of the more complex 2-D images is any better, although counting is much quicker).

5.3 BULK MEASUREMENTS

5.3.1 Liquid water content (lwc): As we have seen, sampling limitations or uncertainties about sampling volumes preclude the accurate measurement of lwc by counting single particles even if the particles are known to be spherical water drops. Ice water or mixed ice+liquid content measurements are even more difficult. There is therefore a need for bulk condensed water measurements.

The most widely used technique is based on measuring the heat balance of a heated, exposed wire (eg the Johnson-Williams (JW) probe) or cylinder (eg the King probe). Due to the complexity of these flows, calibration is empirical and depends on wind-tunnel trials.

In the JW probe (Fig 14), a 2cm length of heated wire (diam. 0.5mm) is exposed transversely to the airstream. Impinging drops are evaporated and cool the wire, changing its electrical resistance, thus

Electrical dissipation = Rate of loss of sensible heat + Evaporation.
(I) (II)

Term (I) clearly depends on many factors including the ambient temperature and the airspeed, so to compensate a second wire is mounted longitudinally. Its heat loss also depends on these factors, but it is not so sensitive to lwc. Therefore, the difference in the power dissipated in the two wires mainly reflects the rate of accretion of liquid water, from which the lwc may be derived. With a well-maintained probe and a good calibration, accuracy is about $\pm$5% (Ref 11). The response time is about 0.4s.

An example of data from this probe is shown in Fig 7.

Limitations:

i. Needs an empirical calibration against a standard in a wind tunnel.

ii. Sensitive to water drops only. The collection efficiency of the wire is believed to become increasingly poor for drops with r> 30μm, so their contribution (nb this is usually small) is underestimated.

iii. It saturates if lwc> 3g/m^3 when there is insufficient heat available to evaporate all the accreted water.

iv. The compensation method is only approximate and needs frequent adjustment (baselining) in clear air.

v. Misreads in icing conditions when ice can form on the compensation wire mount and probe housing.

5.3.2 Total water content: Because of the difficulties of separating one phase from another prior to measurement, another approach is to evaporate all the water in condensed phases and to measure the vapour density. This is often useful since it is often more useful to know the total water content than that contained in the various phases. The main problems lie in designing efficient evaporators and hygrometers capable of working at sustained high temperatures. However, progress is being made (eg Ref 12) and a fast response can be achieved if Lyman-alpha hygrometers are used.

5.3.3 Temperature: Although a basic thermodynamic variable, it is notoriously difficult to measure in cloud because of potential evaporative cooling effects. This is especially true for aircraft where dynamic heating of several degrees inside thermometer housings is not uncommon. The air is thus no longer saturated and significant evaporative cooling is possible. Air can either be cooled during compression, or drops can impinge on immersion sensors before evaporating. Electrical resistance thermometers are therefore usually carefully designed to try and keep the elements dry. This appears to be fairly successful, and although there appears to be a limited sensitivity to lwc, in-cloud temperatures measured by immersion techniques are certainly within 1°C of the true values. However, until recently there was no alternative method for comparison.

Attempts have been made to avoid these problems by only measuring wet-bulb temperature in cloud. However, this is also beset with problems: the wicks are usually very fragile, it is difficult to ensure that the wick stays wet and they are sensitive to chemical pollution of the wetting agent.

5.3.3.1 Radiation thermometers: These appear to hold out the best hope for accurately measuring the temperatures inside water clouds since they avoid all of the problems of immersion devices.

In order to make a local measurement, the chosen wavelength must lie in a region where the atmosphere absorbs very strongly. This also reduces the sensitivity to particle concentration, shape and composition. Met O 15 have developed a radiometer working in the 4.3μm CO_2 absorption band where 80% of the signal originates from within 10m of the instrument (Ref 13). This has undergone flight trials only very recently, but appears to be working very well. Examples of data obtained from this device are compared with temperatures from the Rosemount platinum resistance thermometer during a cumulus penetration in Fig 15. The scatter plot of the same data (Fig 16) suggests that the Rosemount underreads by about 0.5°C per g/kg of liquid water because of evaporative cooling. Further tests are continuing.

5.4 SUMMARY

Table 1 summarizes some of the main characteristics of the devices discussed above.

5.5 OUTSTANDING PROBLEMS

These include the following:

i. How to classify images from 2-D data, assign the correct physical properties and hence determine bulk quantities. This is especially difficult with small (<100μm) particles.

ii. There is currently no way of measuring small ice particles or distinguishing them from liquid drops. Conversely, are small particles in supercooled clouds liquid or frozen?

iii. When do automatic cooled mirror hygrometers measure dew point and when do they measure frost point?

iv. There have been very few in-situ measurements of ice nuclei and their properties.

v. We have a poor understanding of CCN distributions and their evolution.

REFERENCES

1. King W 1986 Air flow and particle trajectories around aircraft fuselages. I: Theory. J Atmos. Ocean. Technol., 1, 5-13.

2. Rangno A & Hobbs P 1983 Production of ice particles in clouds due to aircraft penetrations. J Appl Met, 22, 214-232.

3. Rogers R R 1979 A short course in cloud physics. Pergamon Internatl. Library.

4. Twomey S 1978 Developments in Atmospheric Science. Atmospheric Aerosols 169-172.

5. Hudson J & Squires P 1976 An improved continuous flow diffusion cloud chamber. J Appl Met, 15, 776-782.

6. Mason B J 1971 The Physics of Clouds. O.U.P.

7. Mossop S C 1983 Intercomparison of instruments used for measurements of cloud drop concentration and size distribution. J Appl Met, 22, 419-428.

8. Pinnick R et al 1981 Calibration of Knollenburg FSSP light scattering counters for measurements of cloud drops. J Appl Met, 20, 1049-1057.

9. Knollenburg R G 1970 The optical array: an alternative to scattering or extinction for airborne particle size determination. J Appl Met, 9, 86-123.

10. Conway B J et al 1982 Ground-based and airborne holography of ice and water clouds. Atmos. Environment, 16, 1193-1207.

11. Strapp J & Schemenauer R 1982 Calibrations of Johnson-Williams liquid water content meters in a high speed icing tunnel. J Appl Met, 21, 98-108

12. Leighton J et al 1985 A Lyman-alpha total water content hygrometer: construction and testing of a prototype. Met O 15 Internal Note No. 65, 53pp.

13. Atkinson N et al 1984 A radiation thermometer for cloud temperature measurement from aircraft. Proc IX Internatl. Cloud Phys Conf., Tallinn, USSR.

Instrument	Ice/water	Size range (radius)	Sampling details	Limitations
TGDC CCN counter	water	-	~ 1 count/min	$0.1 < S < 5\%$ $N < \sim 10^3$ cm^{-3}
Impactors Oil MgO or soot Foil Replication	 both both	 1 μm → 10 μm → 100 μm →	Fraction of a)second exposure)time Few secs	Collection efficiency si Particle shattering on impact. Small samples. Tedious analysis.
FSSP	water	0.5-24 μm	0.1s-10s average	Sampling volume uncertai and shape. No ice crystals present. Sizing ambiguity at smal radii.
2-D probes cloud precip.	both	12.5-400 μm 0.1-4mm	Each particle image recorded	Discrete detector size. Undercounting at small r Sampling volume uncertainty
Holography	both	5 μm →	Instantaneous ~0.5l volume	Lengthy analysis Noise limits
Photography	both	1 μm →	Instantaneous $\sim 10^{-3}$ cm^3	Small depth of field.
Johnson-Williams	water	smaller drops collected with higher efficiency	Response time ~0.4s	lwc < 3 g m^{-3}. Insensitive to ice particles. Misreads in icing conditio

Table 1 Summary

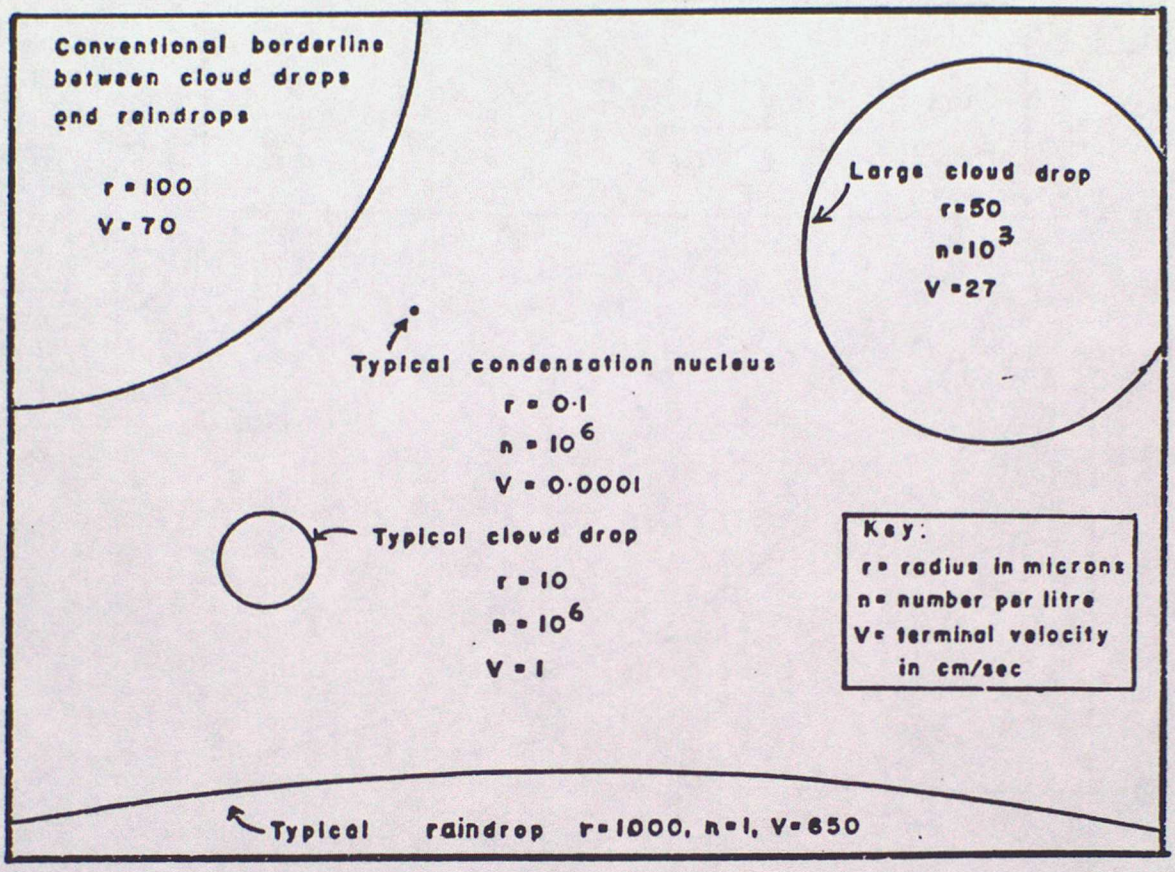

Fig 1 Relative particle sizes.

$$1 + S = \frac{e_s'(r)}{e_s(\infty)} = 1 + \frac{a}{r} - \frac{b}{r^3}$$

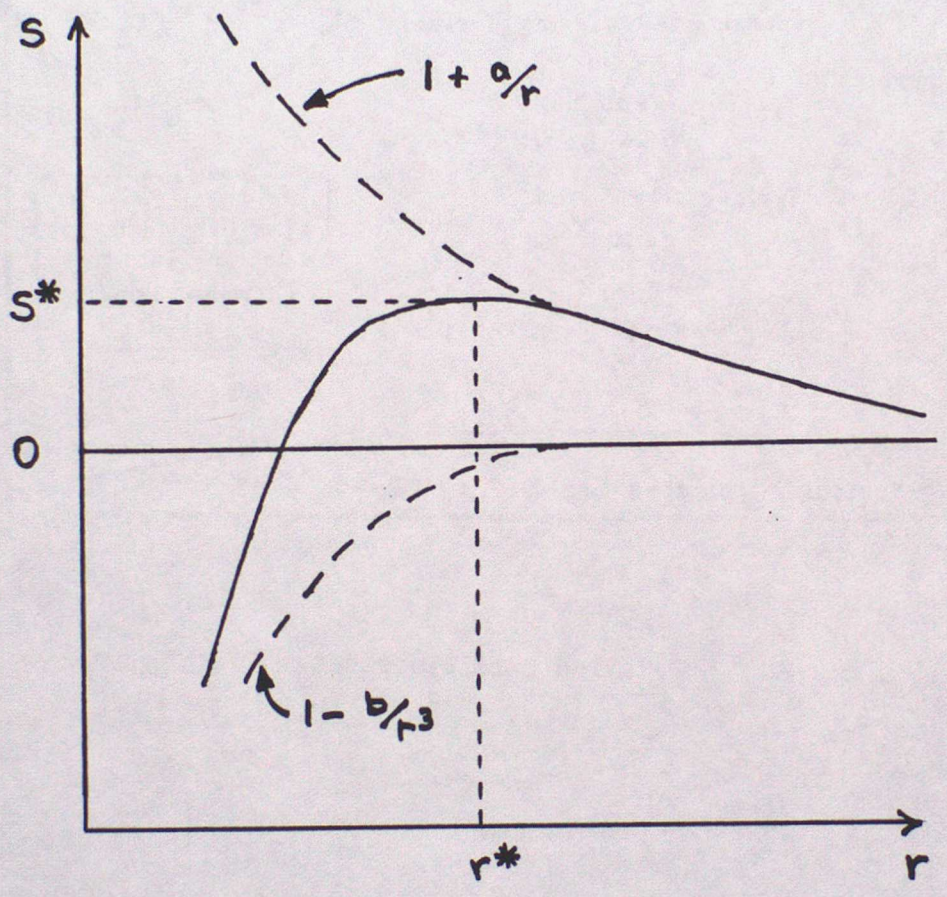

Fig 2 Equilibrium supersaturation as a function of solution droplet size.

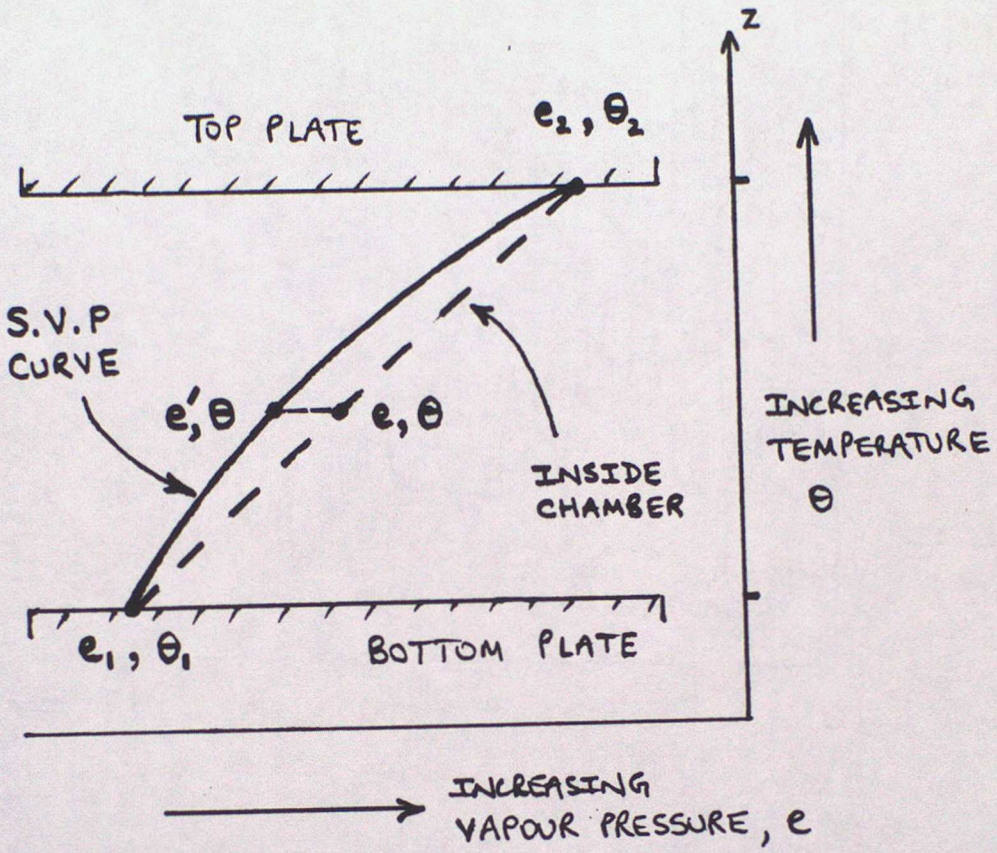

SUPERSATURATION, $S = (e - e')/e'$

e.g. IF $z = 1$ cm, $\theta = 20°C$, $\theta_2 - \theta_1 = 3°C$

then $S = 0.4\%$

Fig 3 Operating principle of the TGDC.

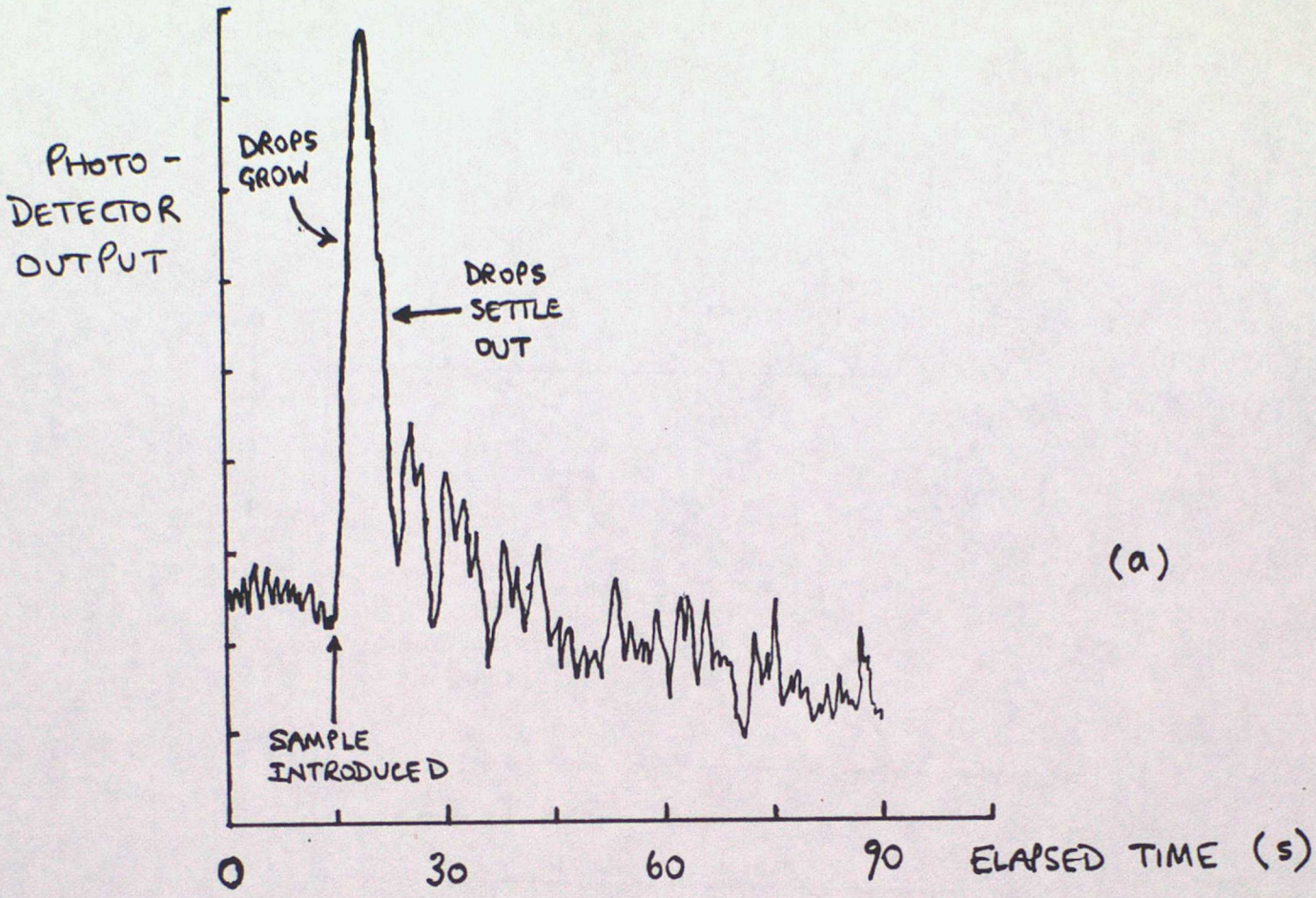

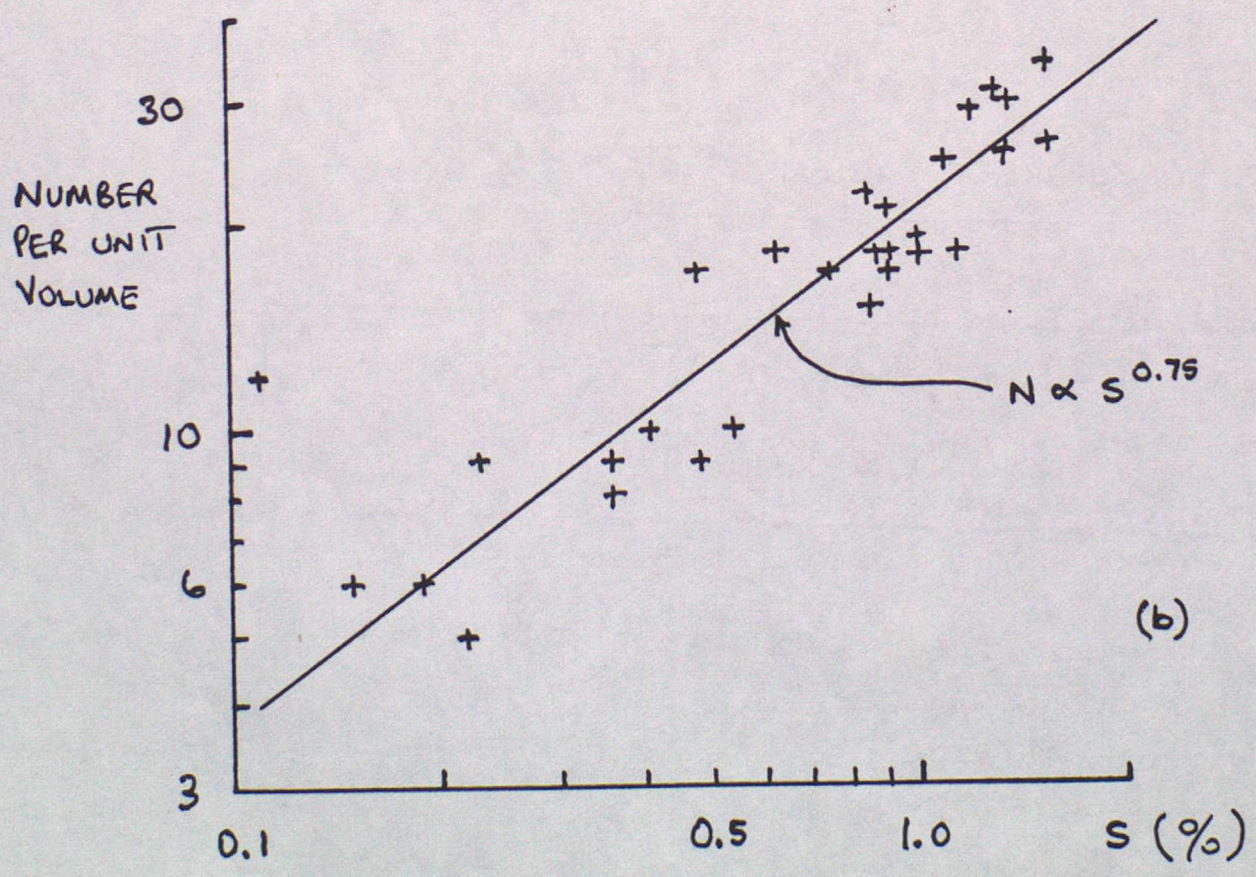

Fig 4

a) Example photodetector output from TGDC (proportional to number and size of drops) as a function of time.

b) An example of an activation spectrum measured with a TGDC.

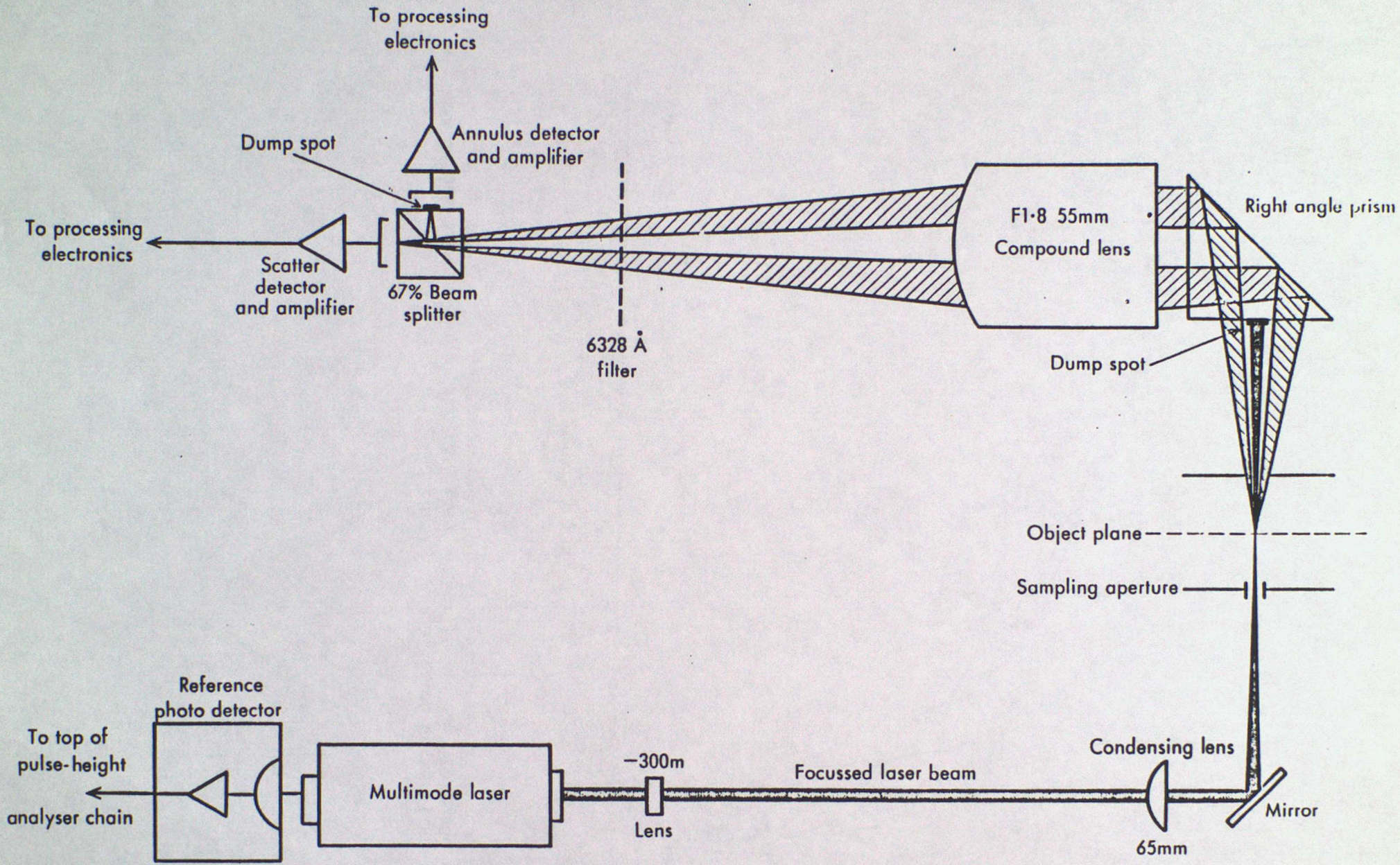

Figure 5. Forward scattering spectrometer probe optical and detector system

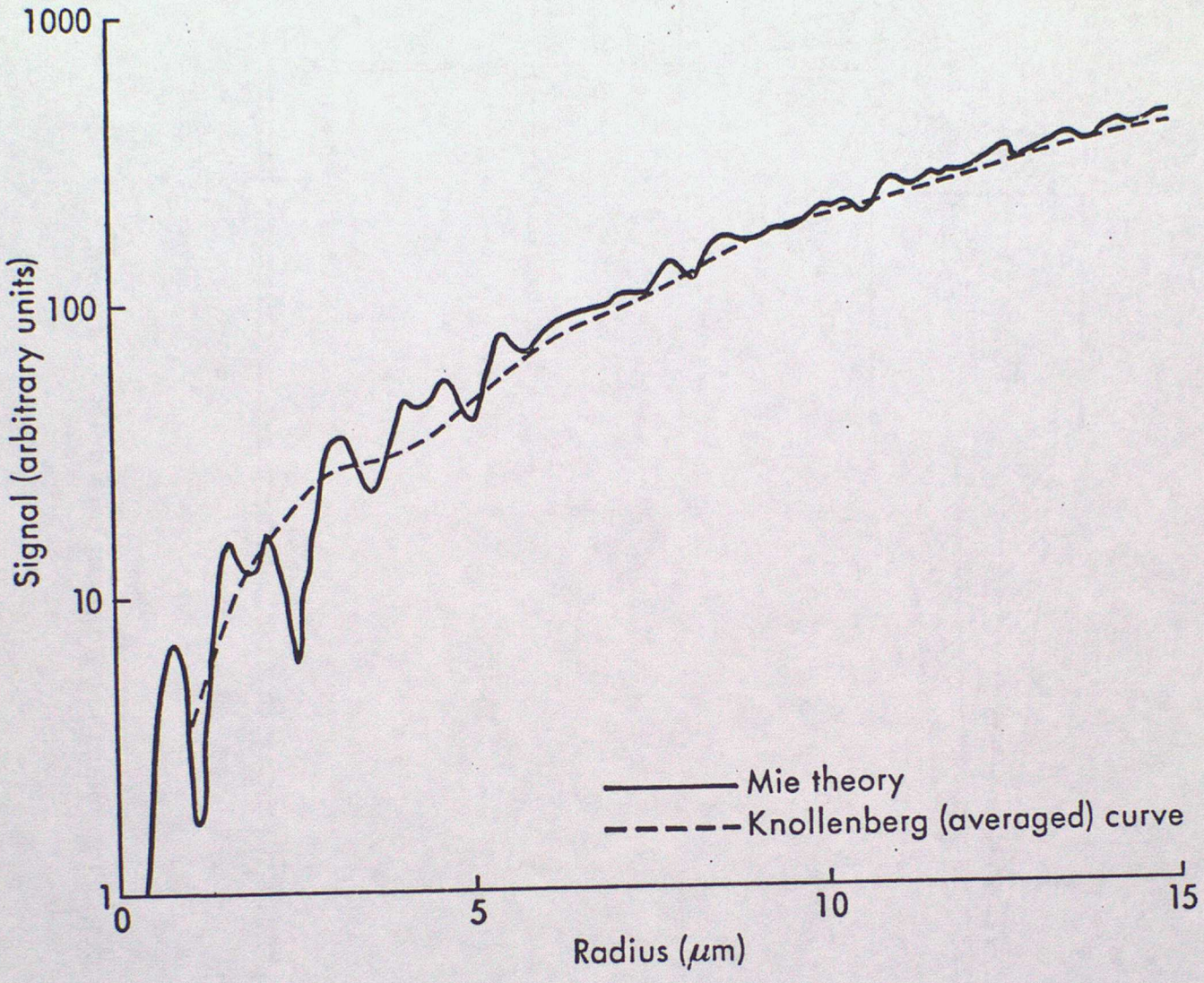

Fig 6 Intensity scattered into the range of angles 7.1°–15.3° from a spherical droplet of radius r at 0.63 μm. Also shown is the makers calibration curve.

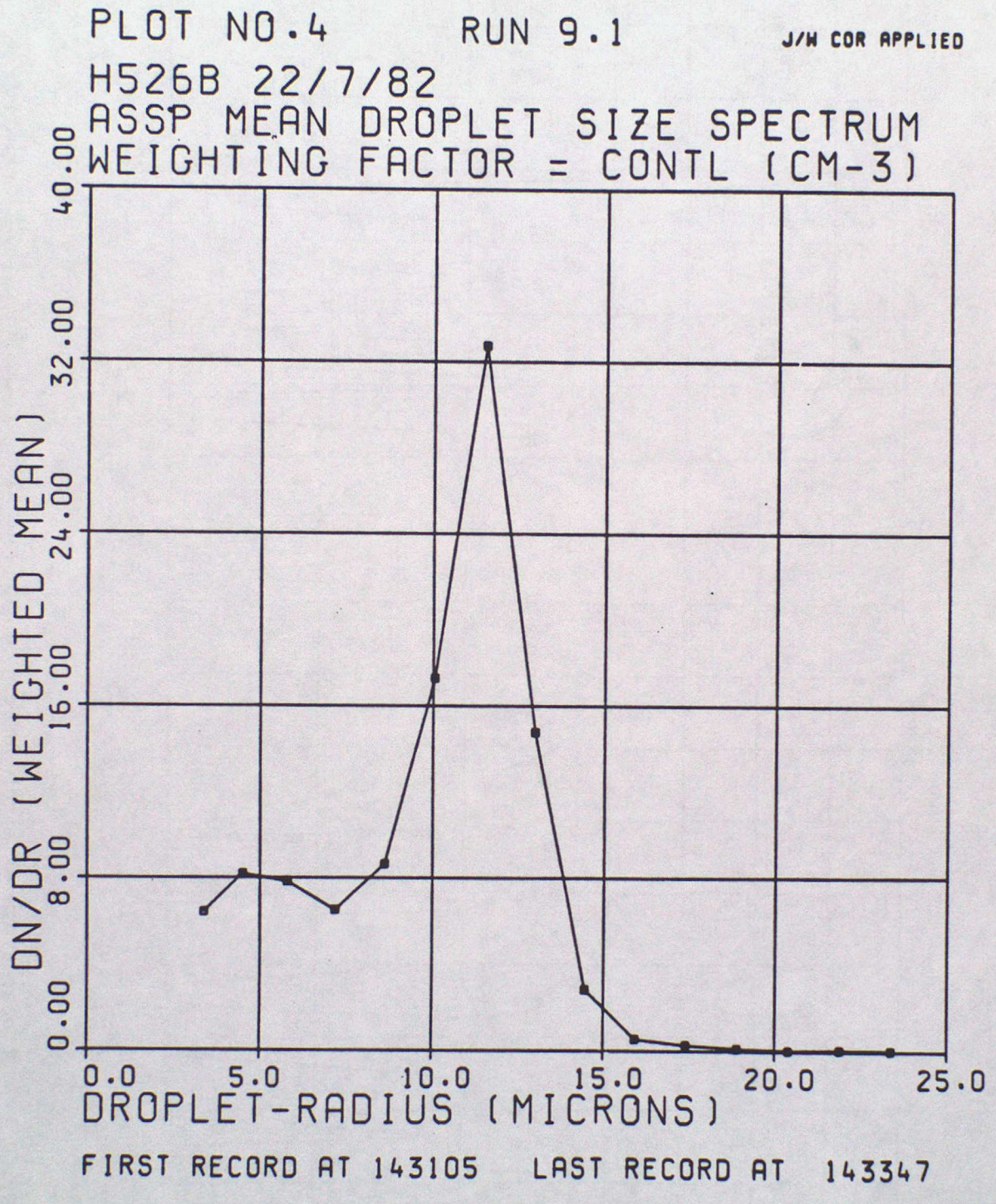

Fig 7 a Example averaged droplet spectrum measured by the ASSP in stratocumulus

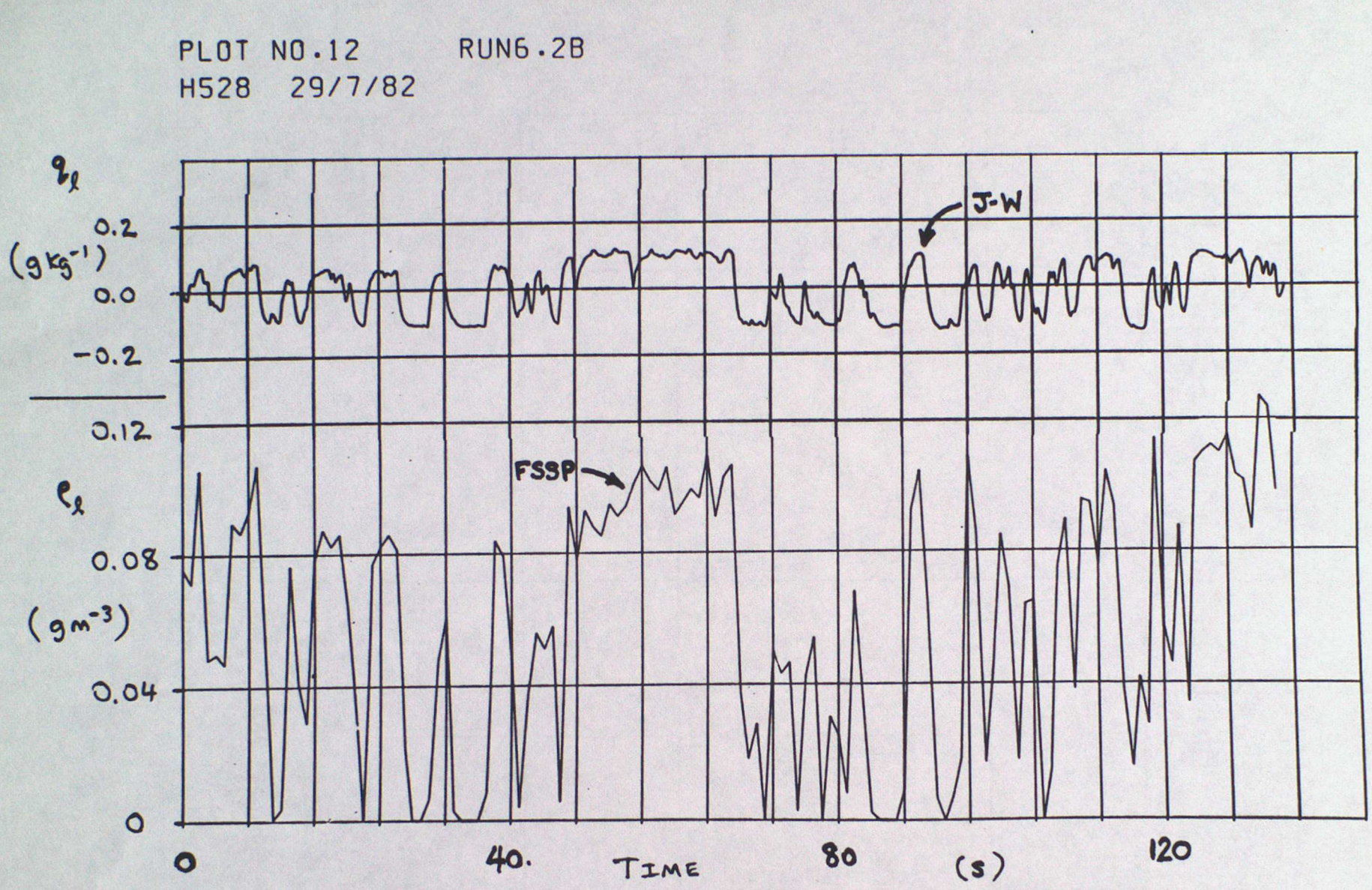

Fig 7 b A comparison of liquid water content measured by the FSSP (by integration of 1s averaged spectra) and the J-W probe

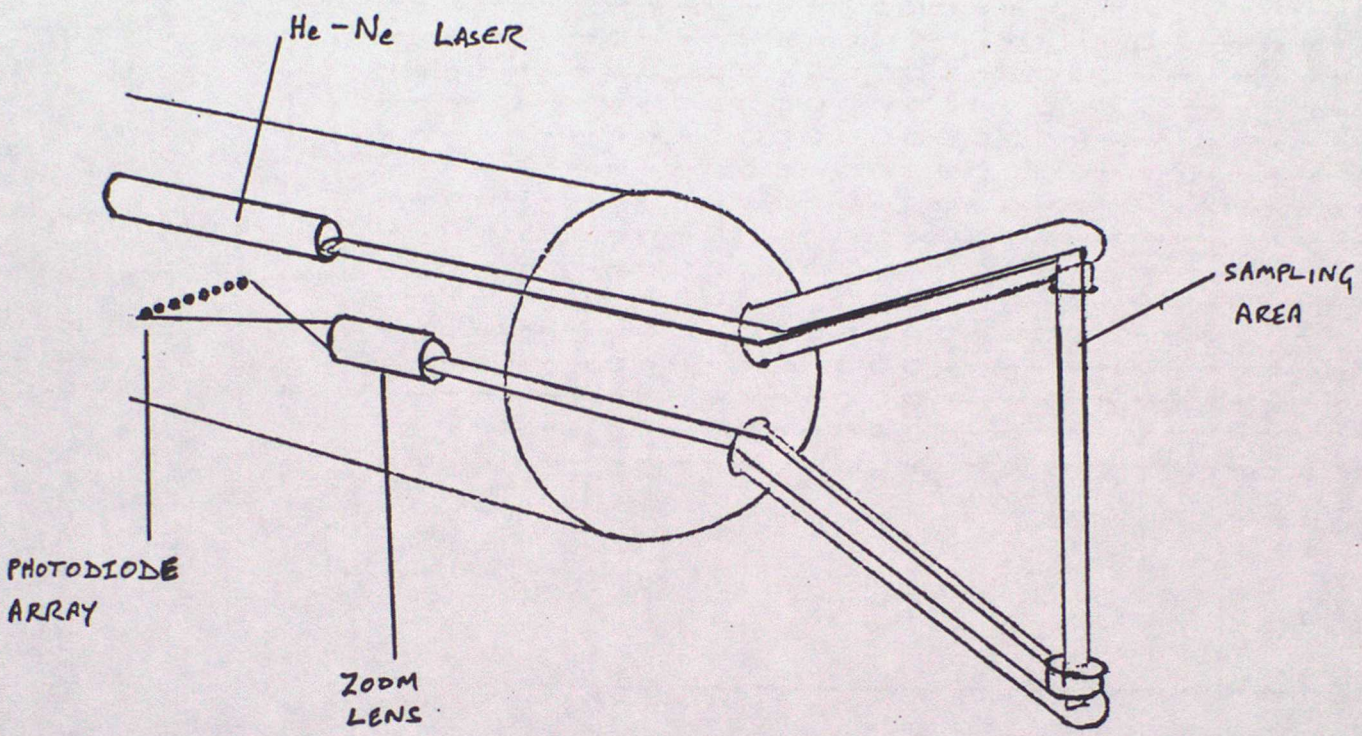

Fig 8 Optical layout of the PMS 2-D probes.

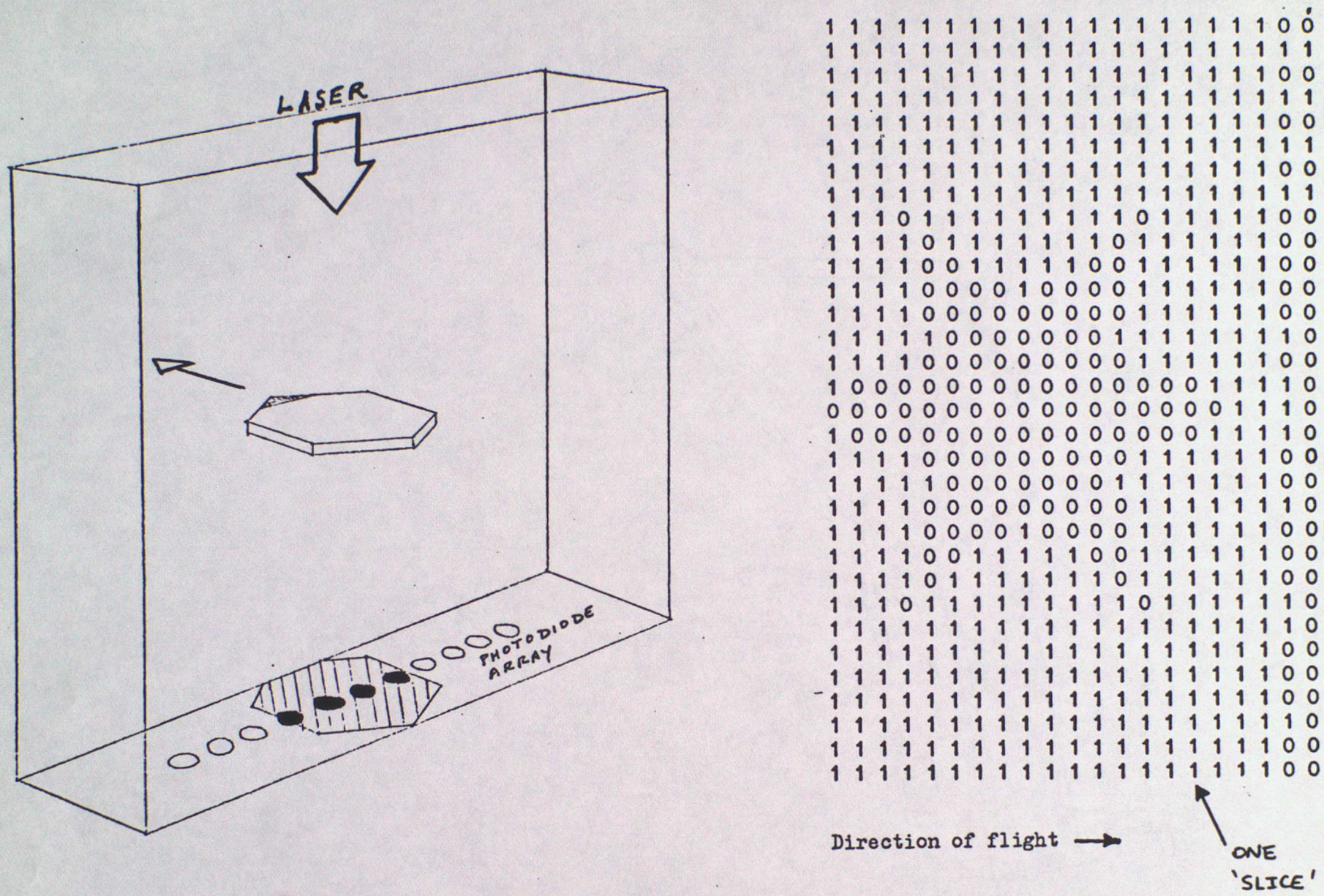

Fig 9 Formation of shadowgraph and digitized image in 2-D probes.

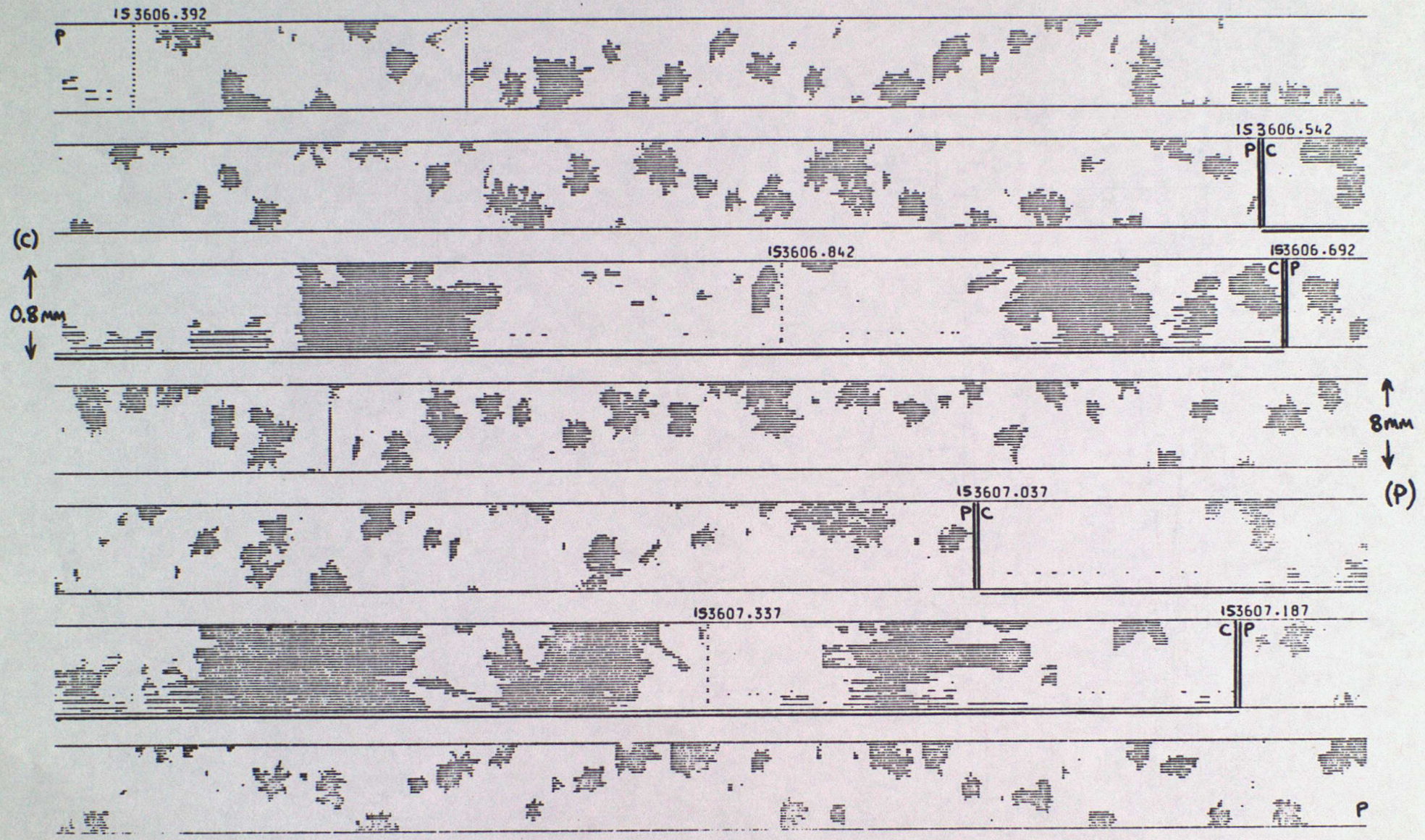

Fig 10 Example of 2-D cloud (C) and precip. probe (P) images from part of a flight on 21 Dec 1983 in precipitating Cu cong. The record is continuous with C and P data interleaved. C-probe data has a double underline. Length scales for both probes are indicated.

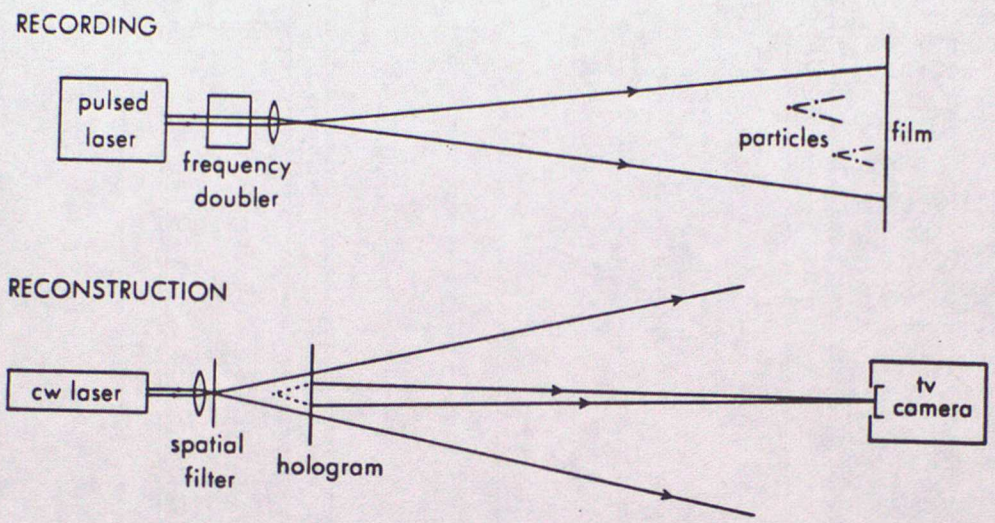

Fig 11 Operating principles of the holographic particle sizing system.

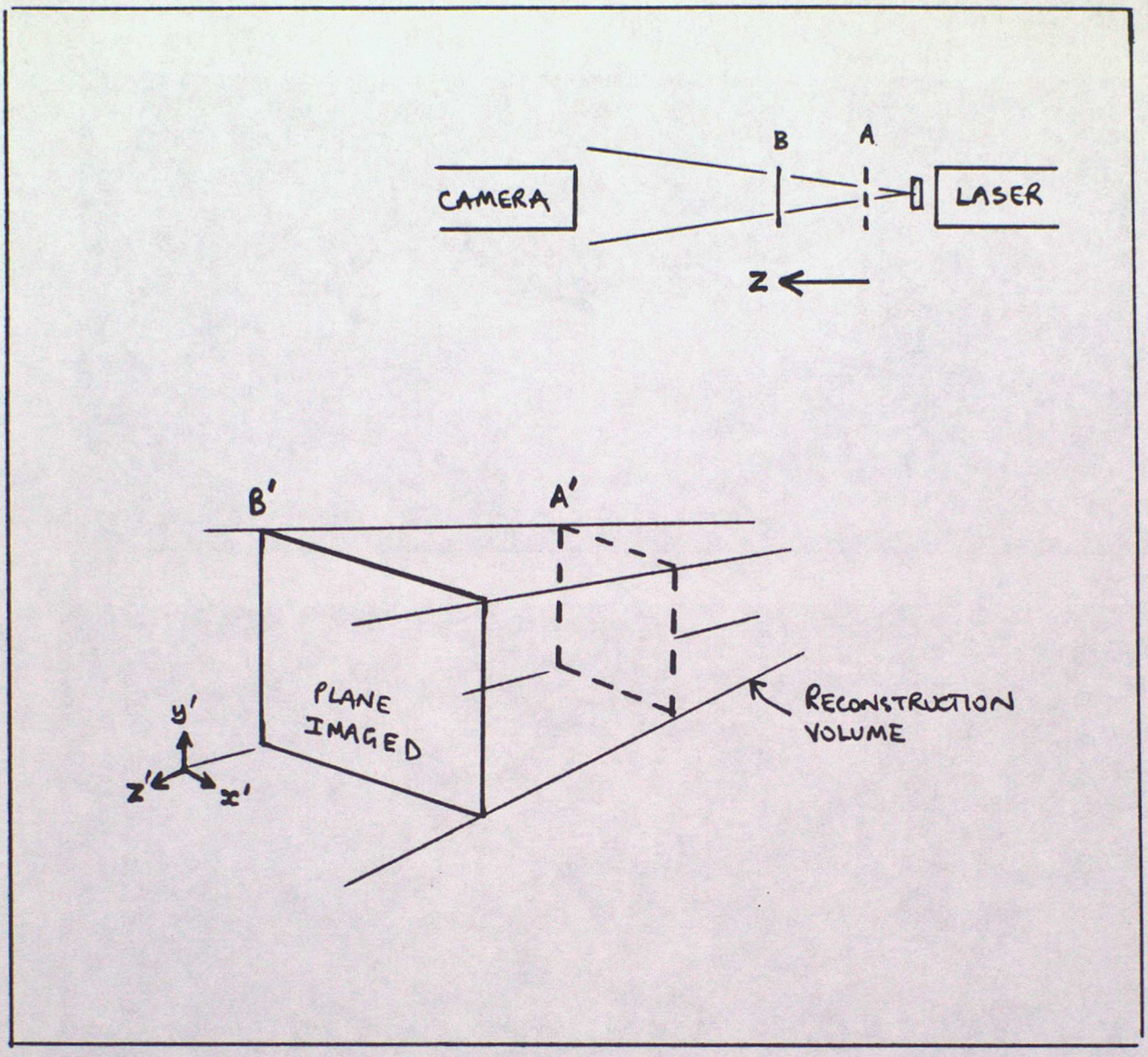

Fig 12 Successive xy planes are imaged as the hologram is moved in the z-direction.

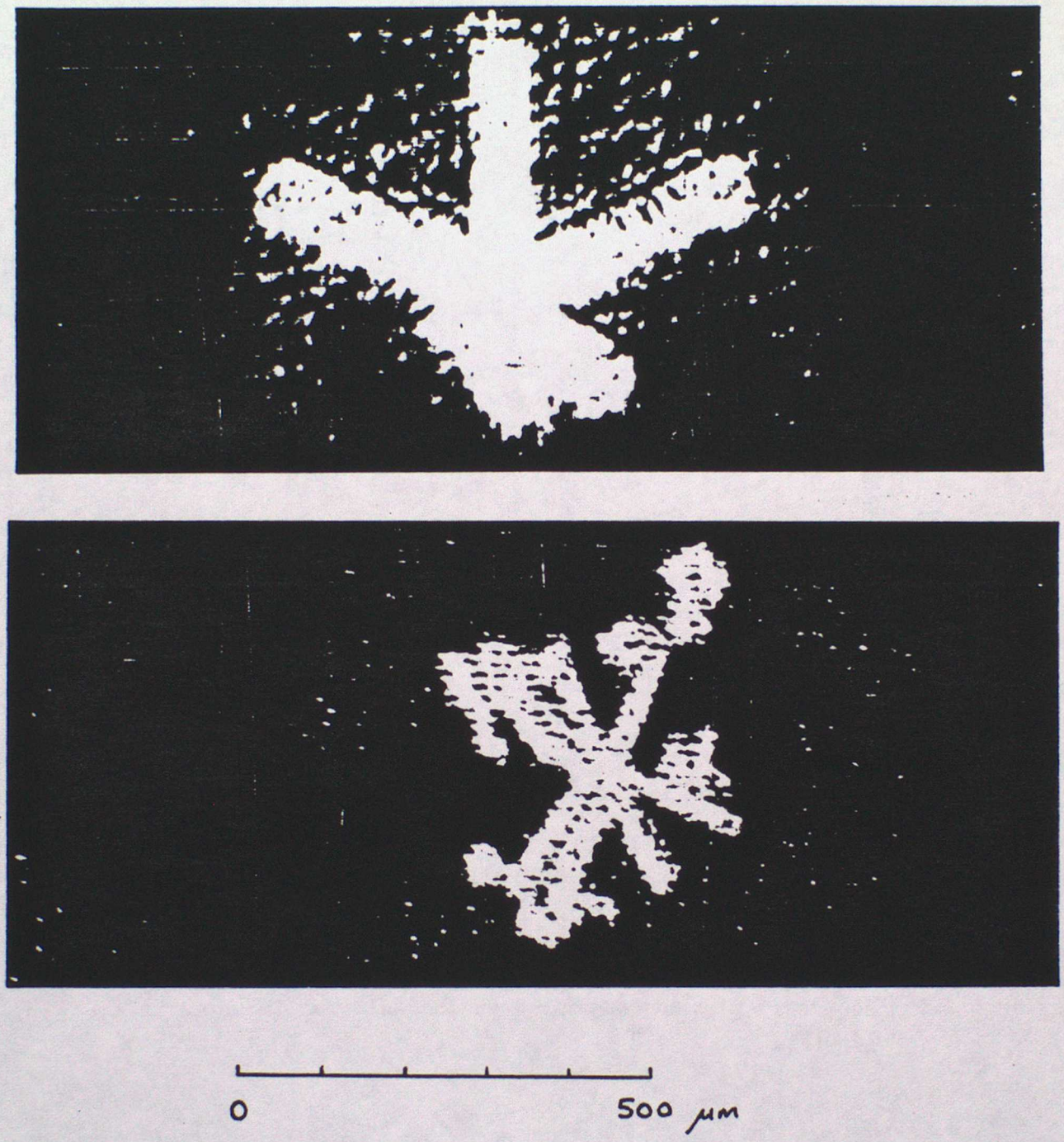

Fig. 13 Examples of reconstructed holographic images. These show ice crystals observed at the base of a Cs layer, T≈230K. (From Ref 10).

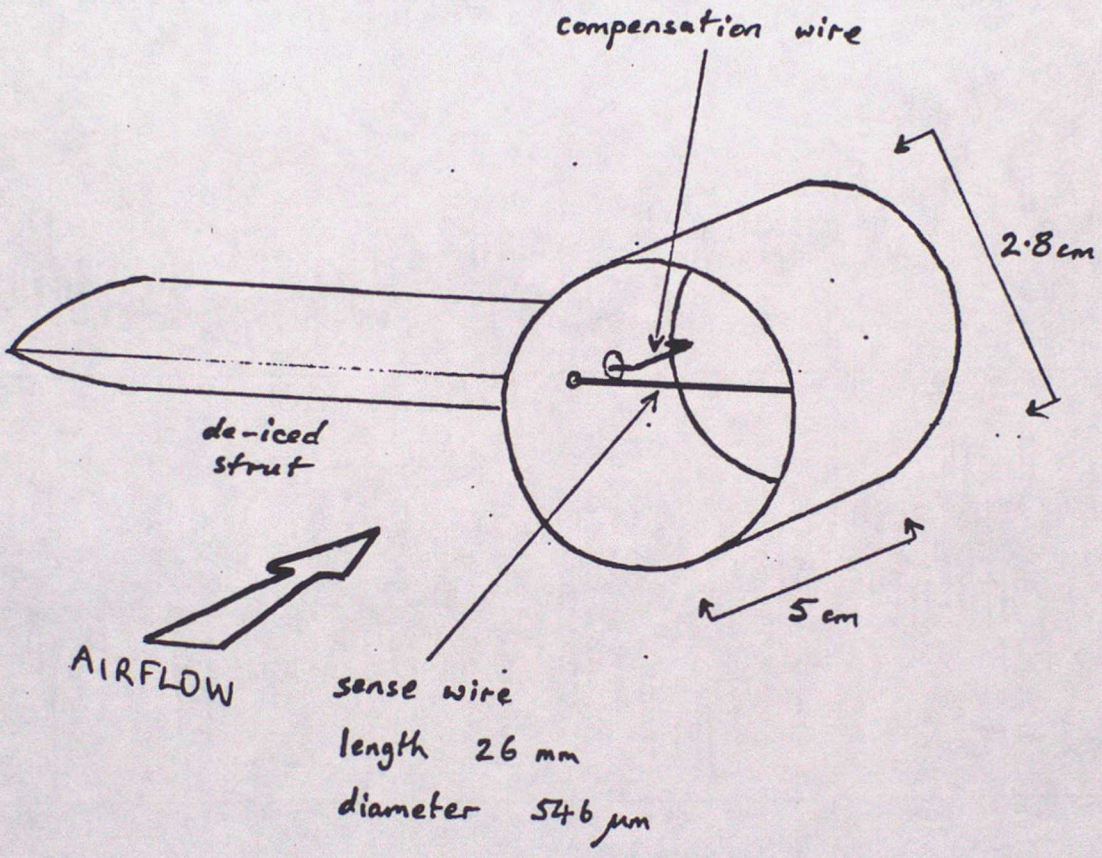

Figure 14. The Johnson-Williams sensor head.

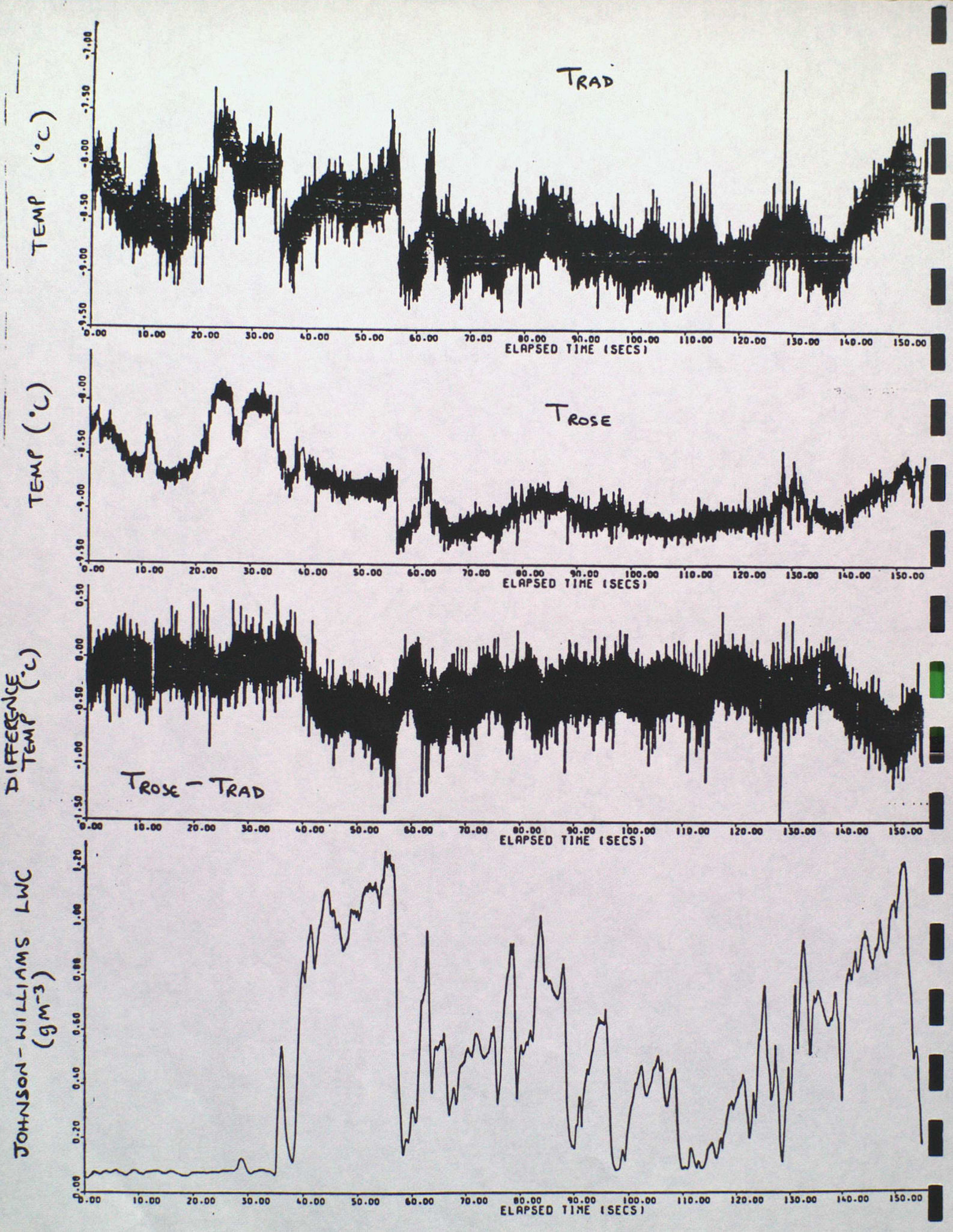

Fig 15 Radiation thermometer (T_{RAD}) and Rosemount (T_{ROSE}) data during a cumulus penetration. Note the correlation between the difference and the lwc.

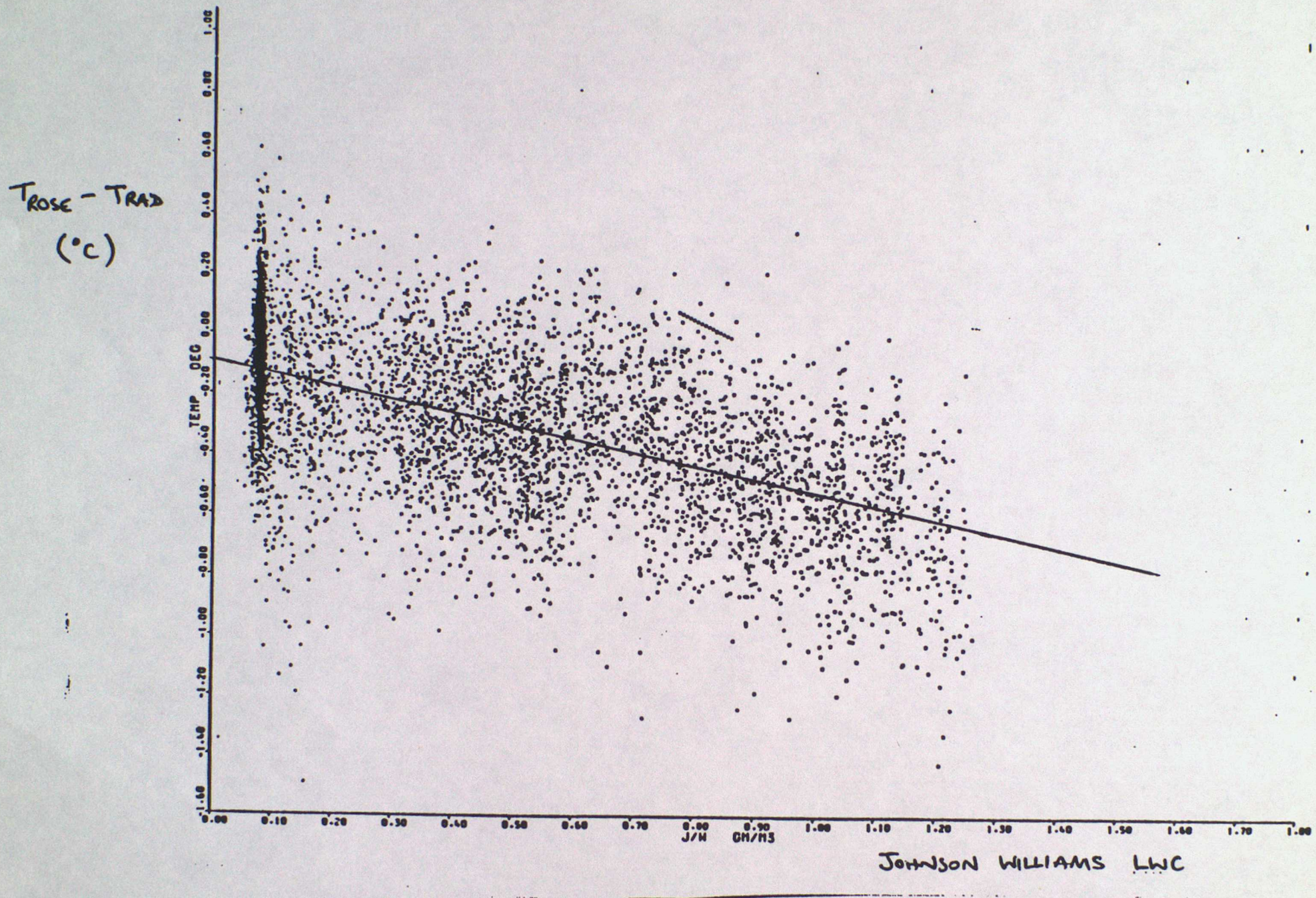

Fig 16 Scatter plot of data shown in Fig 15. Line is best fit.

6. THE INTERACTION OF RADIATION WITH PARTICLES: BACKGROUND

J S FOOT

METEOROLOGICAL RESEARCH FLIGHT

6.1 INTRODUCTION

The next two lectures introduce the problems involved in calculating radiative transfer through haze or cloud layers in the atmosphere. In the first we summarise the definitions, outline scattering theory and discuss the assumptions commonly made in discussing longwave and shortwave transfer through clouds. In the second lecture we shall discuss in more detail some of the particular areas that current research is concentrating upon in the treatment of haze layers, water and ice clouds.

More detailed discussion on some of the Figures will be given in the lectures.

6.2 DEFINITIONS

For monochromatic radiation Beer's law defines an extinction coefficient β_e such that a beam of initial radiance N_o (units $Wm^{-2}sr^{-1}$) is attenuated to a value N in travelling a distance L such that

$$N = N_o \exp - \left[\int_o^L \beta_e \, dl\right] \qquad (1)$$

The term in the brackets is referred to as the optical depth τ.

Attenuation is made up of two principal parts, absorption and scattering so that we can similarly define absorption (β_a) and scattering (β_s) coefficients which obey:

$$\beta_e = \beta_a + \beta_s \qquad (2)$$

Single scattering albedo ω is defined by:

$$\omega = \beta_s/\beta_e \qquad (3)$$

and represents the proportion of energy that is scattered in a single interaction with an 'average' particle. For a distribution of particle

sizes with concentration n(r) with radii between r and r + dr we can define an extinction efficiency (or scattering, absorption efficiencies) Q_e (or Q_s, Q_a) by:-

$$\beta_e = \int_0^\infty n(r)\, \pi r^2 Q_e(r)\, d_r \qquad (4)$$

For large particles obeying geometric optics $Q_e(r) = 2$, that is because apart from the energy that directly hits the particles which is absorbed, reflected or transmitted, there is an equal amount that is defracted around the particle.

For unpolarized radiation scattered by a spherically symmetric particle the radiance of the scattered radiation $N(\theta)$ is a function of the scattering angle θ and is given by the phase function $p(\theta)$ thus:

$$N(\theta) = \frac{p(\theta)}{4\pi} \cdot L' \qquad (5)$$

where L' is the fraction of the irradiance (Wm^{-2}) that interacted with the particle. For isotropic scattering $p(\theta) = 1$. For many purposes, eg calculations of net irradiance, the detail of the phase function can be approximated to a single number, the asymmetry factor g thus:-

$$g = \tfrac{1}{2} \int_0^\pi p(\theta) \sin\theta \cos\theta\, d\theta \qquad (6)$$

It approximately represents the difference between the flux scattered into the forward and backward hemispheres. For isotropic scattering $g = 0$, for complete scatter into the foward direction $g = +1$ and into the backward direction $g = -1$.

6.3 MIE THEORY

Mie theory provides a general solution to the problem of the interaction of a plane electromagnetic wave with a spherical particle. The solutions are obtained by the application of Maxwell's equations with a spherical boundary condition [see Van de Hulst or Deirmendjian] and provide complicated series dependent on the size parameter

[$x = \frac{2\pi r}{\lambda}$] and the complex refractive index of the sphere. The solutions reduce to simpler solutions in the limit of small and large x. Thus $x << 1$ gives, Rayleigh scattering where scattered radiances is proportional to r^6/λ^4 or $x >> 1$ gives geometric optics where the extinction efficiency $Q_e(r)$ is equal to 2.

For transfer of solar radiation, cloud and haze particles are sufficiently large that the size parameter is not small enough for Rayleigh scattering limits to apply. Only molecular scattering obeys the Rayleigh limit - hence the blue sky - the phase function is symmetrical (g = 0) but not isotropic.

$$p(\theta) = {}^3/4(1 + \cos^2\theta) \qquad (7)$$

Although for the longwave region small haze particles will approximate to Rayleigh scatters this is generally unimportant because the optical depth of hazes in the thermal region is not significant.

The geometric limit is satisfied for large droplets or ice crystals, approximately 20 μm radius for the solar region or 100 μm radius in the longwave region. As most clouds are composed of a high concentration of droplets smaller than these, Mie theory must be used.

Typical Mie calculations are shown in Figure 6.1 which shows the efficiency factors Q_e, Q_a, Q_s as a function of x for water spheres at a wavelength of 8 μm where the bulk absorption coefficient of water (k) is $3.6\ m^{-1}$.

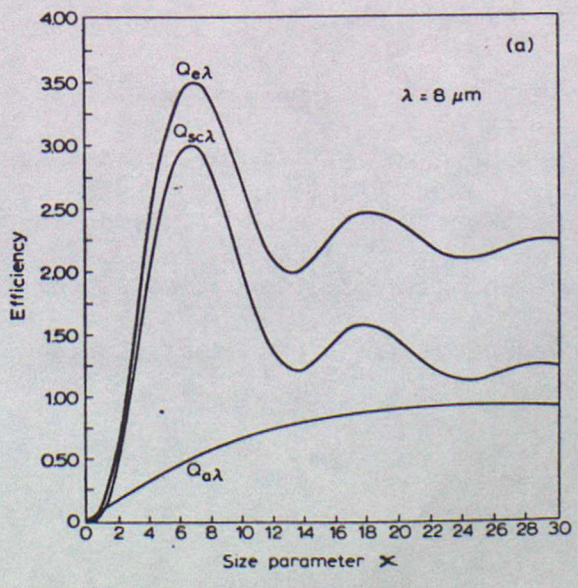

Fig. 6.1

$Q_{e,a,s}$ at 8 μm wavelength for water spheres as a function of x.

For a strongly absorbing particle in the geometric limit $\omega = 0.5$ and in the Rayleigh limit $\omega = 0$. For a weakly absorbing particle [$\omega > 0.9$] the single scattering albedo can be approximated by

$$\omega = 1 - 0.8\ kr \qquad (8)$$

[see Twomey and Bohren (1980)].

6.4 MAGNITUDE OF EFFECTS

Fig 6.2 shows the extinction coefficient at the surface from 0.3 μm - 10 cm wavelength. This is copied from a communication journal and indicates

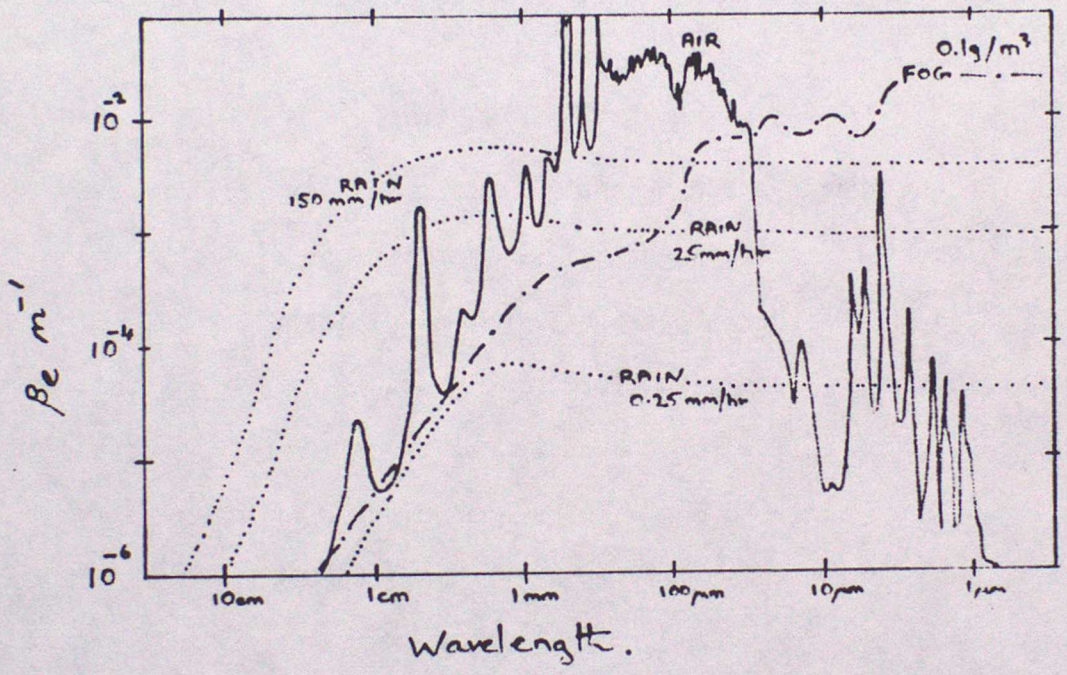

Fig. 6.2 The extinction of clear air (surface conditions), fog and precipitation as a function of wavelength.

the relative importance of various attenuation processes through this region of the spectrum. Clouds and gases, principally water vapour, are both important attenuators. It must be remembered that while particle extinction changes slowly with wavelength much of the gaseous attenuation is confined within very fine lines or groups of lines and Beer's law does not apply to finite bandwidths.

6.5 COMMON ASSUMPTIONS MADE IN PREDICTIONS

6.5.1 Longwave Region

a. Haze particles and layers have small values of x and low optical depths and are usually ignored. In some cases for example the determination of SST from satellite, haze particularly at high altitude may be important.

b. For cloud droplets (x ~ 6), Figure 6.1 indicates that Q_a is approximately proportional to x and approaches unity, and Q_s is between 1 and 3. Scattering however is often ignored because most of the scattering takes place in the strong forward peak (g ~ 0.9), and because absorption is strong the likelihood of many scattering events redirecting the beam significantly is small. It is common practice to assume that $Q_a = cr$, with c = constant, from equation (8) although this will not be valid for large particles or in regions where water is a particularly strong absorber where $Q_a \simeq 1$.

$$\beta_a = \pi c \int_0^\infty n(r) r^3 \, dr \qquad (9)$$

substituting the liquid water content $w = \frac{4}{3}\pi\rho\int_0^\infty n(r)r^3 \, dr$, equation 9 becomes

$$\beta a = \frac{3\ cw}{4\ \rho} \qquad (10)$$

Chýlek and Ramaswamy (1982) have shown that equation (10) provides a good fit within the 8-12 μm window where most of the radiative cooling takes place. The radiative properties are thus insensitive to the drop-size distribution and further more for a cloud with a liquid water content of 0.5 gm^{-3} then the emissivity of only 20 m depth is 0.8 and for 60 m the value is close to unity. Low level water clouds can be assumed to behave as black bodies.

6.5.2 Shortwave Region

a. Haze layers are generally ignored in GCM. They can have significant effect by reducing the heat flux to the surface and increasing heating within the boundary layer. A balance between these two processes exists, Hansen et al (1979) for example suggests that with surface albedo of 0.15 a critical value of ω of 0.85 exists: above this value cooling of the boundary layer occurs, below it warming. Typical values of vertical optical depth are 0.1 - 1.0, g ranges 0.6 - 0.8 and ω most typically >0.9.

b. The geometric optics approximations for clouds provided a reasonable estimate of the extinction coefficient. Thus

$$\beta_e = \frac{3\,w}{2\,r_e\,\rho} \qquad (11)$$

where r_e is the equivalent radius defined by

$$r_e = \frac{\int_0^\infty n(r) r^3\,dr}{\int_0^\infty n(r) r^2\,dr} \qquad (12)$$

Both scattering and absorption are important in the transfer of solar radiation in clouds (absorption for wavelengths >0.7 μm). Here the optical properties are dependent upon the drop-size distribution. Figure 9.8(c) shows some calculations of cloud absorption and albedo.

6.6 Remarks

In the next lecture we will look at some of the assumptions that have been described above.

6.7 References

See Lecture 7.

7. THE INTERACTION OF RADIATION WITH PARTICLES: CURRENT RESEARCH

J S FOOT

METEOROLOGICAL RESEARCH FLIGHT

7.1 INTRODUCTION

The purpose of this second lecture is to examine some of the assumptions of the first lecture. Much of this is the subject of current research and biased toward MRF's own research interests. These notes are supplied to outline the problems and provide some references for the work.

7.2 MIE THEORY

Mie theory applies to spherical homogeneous particles. It can be extended to cover more complicated shapes Liou (1972), Wiscombe and Mugnai (1986) as well as spheres with concentric shells of different material, Fenn and Oser (1965). Water clouds are composed of ideal spheres provided they are not contaminated by insoluable particles. Chylek and Ramaswamy (1984) have considered the problem of carbon particles randomly distributed within cloud particles: interestingly the carbon is twice as effective at absorbing radiation when dispersed in large water droplets compared to the same aerosol on its own. Crudely we can imagine the droplet acting to 'focus' the radiation onto the absorbing particles. There are few direct determinations of optical contamination of cloud particles and those that exist, [Patterson et al (1984)] suggest that they do not significantly affect cloud absorption. Haze and ice particles will however not behave as spheres.

Pollack and Cuzzi (1980) present an empirical model of scattering by irregular particles and fit their calculation with observations using large replica particles irradiated with microwaves.

7.2.1 Haze particles

The scattering properties of small haze particles appear to be fairly accurately predicted from Mie theory using a sphere of equal cross-section area. The precise phase function is probably poorly predicted particularly for larger particles where the asymmetry factor is >0.7. In most experiments there is an element of a circular argument because particles are commonly "sized" using optical techniques that measure the scattering intensity in a near-forward direction. According to Pollack and Cuzzi absorption should be described by a sphere of equal volume. The other problem with small haze particles is that the absorbing part - principally elemental carbon - is not uniformly mixed in the aerosol. Two approaches are seen in the literature. One is to fit radiation observation using an "effective" refractive index of the mixture [eg Kitchen and Squires (1984)]. This refractive index does not correspond to any one substance but a mixture and it depends on how the absorbing part is mixed. The other approach is to attempt to predict that refractive index from a chemical analysis of the aerosol, Sloane (1983). A set of standard aerosol models has recently been introduced by Lenoble and Brogniez (1984). There are four basic components used in this model (water soluble, dustlike, soot and oceanic). These four components are mixed according to their volume to provide typical continental, maritime or urban aerosols. As already indicated in Lecture 6 one of the key parameters in describing hazes is ω. This is extremely difficult to determine, most measurements are made indirectly. A recent workshop provides an excellent review of the techniques and the accuracy that can be obtained in ideal conditions, Gerber and Hindman (1982)

7.2.2 Ice Crystals

Ice crystals present similar problems to haze particles however the impact of the non spherical particles is probably more fundamental

and there has been far less work conducted in this area. Cirrus clouds are particularly important in determining radiation transfer in the atmosphere: a review of the impact of cirrus clouds on the climate is given by Liou (1986).

There are calculations of $p(\theta)$ for perfect hexagonal columns and plates using geometric optics (see Coleman and Liou 1981). These show distinct optical phenomena, however real cirrus particles are probably far less regular. Phase function measured in the laboratory of ice clouds exist (Sassen and Liou (1979)), these are probably more realistic than the calculations but the particles generated within cloud chambers are small compared to those found in nature. There are few direct observations (see Platt and Dilley (1984) and Foot (1988)) and they indicate strong side scattering which is not consistent with Mie calculations on spheres and cylinders or geometric calculations on hexagonal plates and columns. The existence of plates which are highly orientated can also be demonstrated using lidar and such oriented crystal may also significantly increase back scattering efficiencies.

Paltridge and Platt (1981) and Foot (1988) have shown from direct observation of solar albedo and reflectances that cirrus particles are more efficient back scatterers than spherical particles. This is probably also important in the longwave region where the neglect of scattering will be a more significant error. Because of the large size of cirrus particles it is unlikely that the relationship used in equation (10), Lecture 6 will be valid. The longwave absorption coefficient would be expected to be size dependent. Until recently this has been ignored for example Griffith et al (1980) attempted to use equation (10) to analyse cirrus emissivity: Foot (1988) provides some evidence of the size dependence of the longwave absorption coefficient.

There has been even less work on the solar absorption properties of cirrus. Paltridge and Platt (1981) have obtained solar absorption measurements and Foot (1988) has attempted to relate radiances at discrete wavelengths to the observed particle size distribution in a manner consistent with Pollack and Cuzzi theory. One of the major problems in this is to obtain accurate determination of ice water contents of cirrus clouds using present day instrumentation.

7.3 ANOMOLOUS ABSORPTION

One of the areas that radiation scientists have concentrated upon is to obtain agreement between observation and calculations of the solar albedo and absorption of fairly thick apparently uniform clouds composed solely of water droplets. In some work high cloud absorptions are obtained. There is still a great deal of debate as to whether there is a problem and if there is where the discrepancies originate. Recent work, Foot (1988), will be briefly discussed.

7.4 LAYER AND BROKEN CLOUD

Fairly efficient schemes exist for determing the transfer of radiation through plane parallel cloud from τ, ω and g. An excellent review article by Stephens (1984) describes much of the physics as well as the schemes currently used in a number of GCMs. Most cloud regions are far from the plane parallel assumption. One of the major aims for the future must be in providing better microphysical and radiative descriptions of these fields. It seems unlikely that a single description of cloud cover, however measured or inferred can satisfactorily describe both the shortwave and longwave properties of a real cloud field. Some work on shortwave cloud albedo is presented by Kite (1987).

7.5 BIBLIOGRAPHY

Bohren, C.F. and Huffman, D.R. 1983, Absorption and Scattering of Light by Small Particles. John Wiley & Sons, New York.

Deirmendjian, D. 1969, Electromagnetic scattering of spherical polydispersions. Elsevier, New York.

Liou, K-N. 1980, An introduction to atmospheric radiation. International Geophysics Series Volume 26. Academic Press, New York.

Paltridge, G.H. and Plat, C.H.R. 1976, Radiative processes in meteorology and climatology. Developments in atmospheric Science, 5. Elsevier, Amsterdam.

van de Hulst, H.C. 1957, Light scattering by small particles. John Wiley & Sons, New York.

7.6 REFERENCES

Coleman, R.F. and Liou K-N, 1981, Light scattering by hexagonal ice crystals. J. Atmos. Sci. 38, 1260-1271.

Chylek, P. and Ramaswamy, V. 1982, Simple approximations for the emissivity of water clouds. J. Atmos. Sci., 39, 171-177.

Chylek, P. and Ramaswamy, V. 1984, Effect of graphitic carbon on the albedo of clouds. J. Atmos. Sci. 41, 3076-3084.

Fenn, R.W. and Oser, H. 1965, Scattering properties of concentric soot-water spheres from visible and infrared light. Appl. Optics, 4, 1504-1509.

Foot, J.S., 1988, Some observations of optical properties of clouds. Part I: Stratocumulus. Part II: Cirrus. Accepted for publication Quart. J. Roy. Met. Soc.

Gerber, H.E. and Hindman, E.E., 1982, Light absorption by aerosol particles. Spectrum Press, Virginia.

Griffith, K.T., Cox, S.K. and Knollenberg, R.G. 1980, Infrared radiative properties of tropical cirrus clouds inferred from aircraft measurements. J. Atmos. Sci. 37, 1077-1087.

Hansen, J.E., Lacis, A.A., Lee, P. and Wang, W. 1979, Climate effects of atmospheric aerosols: Presented at Conference on aerosols: Urban and Rural Characteristics, Source and Transport Studies, New York Academy of Science.

Kitchen, M. and Squires, E.C. 1984, Aircraft observations of solar radiation in cloud free atmospheres. Boundary Layer Met. 29, 321-342.

Kite, A.J. 1987, The albedo of broken cloud fields. Quart. J. Roy. Met. Soc., 113, 517-532.

Lenoble, J. and Brogniez, J. 1984, A comparative review of radiation aerosol models. Bietr. Phys. Atmos. 57, 1-20.

Liou, K-N. 1972, Electromagnetic scattering by arbitrarily oriented ice cylinders. Appl. Opt. 11, 667-674.

Liou, K-N. 1974, On the radiative properties of cirrus in the window region and their influence on remote sensing of the atmosphere. J. Atmos. Sci. 31, 522-532.

Liou, K-N. 1086, Influence of cirrus clouds on weather and climate processes: a global perspective. Mon. Weather Rev., 114, 1167-1199.

Paltridge, G.W. and Platt, C.M.R. 1981, Aircraft measurements of solar and infrared radiation and the microphysics of cirrus cloud. Quart. J. Roy. Met. Soc. 107, 367-380.

Platt, C.M.R. and Dilley, A.C. 1984, Determination of cirrus particle single scattering phase function from Lidar and solar radiometric data. Appl. Opt. 23, 380-386.

Patterson, E.M., DeLuisi, J, Castillo, R. and Ackerman, T. 1984, Measurements of the absorption of cloud water and unactivated within-cloud aerosols at Whiteface Mountain, New York. Proc. of Int. Rad. Sym. Perugia, Italy, 38-41. Deepak Pub, Virginia.

Pollack, J.B. and Cuzzi, J.N. 1980, Scattering by nonspherical particles of size comparable to a wavelength. A new semi-empirical theory and its application to tropospheric aerosols. J. Atmos. Sci., 37, 868-881.

Sassen, K. and Liou, K-N. 1979, Scattering of polarized laser light by water droplet, mixed-phase and ice clouds. Part I: Angular scattering patterns. J. Atmos. Sci., 36, 838-851.

Sloane, C.S. 1983, Optical properties of aerosols - comparison of measurements with model calculations. Atmos. Environ. 17, 409-416.

Stephens, G.L. 1984, The parameterization of radiation for numerical weather prediction and climate models. Mon. Weather Rev., 112, 826-867.

Twomey, S. and Bohren, C.F. 1980, Simple approximations for calculations of absorption in clouds. J. Atmos. Sci., 37, 2086-2094.

Wiscombe, W.J. and Mugnai, A. 1986, Single scattering from nonspherical Chebyshev particles: A compendium of calculations. NASA Reference Publication 1157.

LECTURE 8. THE EFFECT OF RADIATION ON CLOUD : RADIATION MICROPHYSICS

W.T. Roach, Meteorological Research Flight

8.1 Introduction

Over the past decade or so, there has been a significant shift of the interests of many cloud physicists from studies of convective cloud and precipitation processes to the much longer-lived and quiescent layer clouds and fog in which mean vertical motion can be neglected to a first approximation, but in which radiative transfer becomes of prime importance. This has resulted in a growing literature on the gross effect of radiation on clouds.

On the other hand, radiative transfer physicists have been concerned for about 3 decades with the effects of clouds on radiation. These studies have in recent years received fresh impetus from the requirement to improve physical parametrization in general circulation and climate models.

Sandwiched between the cloud physicists and the radiation physicists, a small number of papers have appeared which consider the effect radiative transfer might have on the growth of individual cloud droplets. The realisation about 10 years ago (Roach 1976, Barkstrom 1978) that the classical Maxwell equations for the transfer of latent and sensible heat between a spherical droplet and its environment did not include a term for radiative transfer led to the birth of 'radiation-microphysics'.

While the insertion of a radiation term in the Maxwell equations for droplet growth is relatively straightforward, the need to include an explicit formulation of the microphysics in models of the evolution of fog or strato-cumulus which contain bulk radiative parametrization is not obvious. However, droplet growth or evaporation induced by radiative transfer must alter the radiative properties of the cloud as a whole. Situations where this may be important must therefore be identified.

The first part of this lecture consists of an assessment of the effect of radiative transfer on the growth of individual droplets and ice crystals. The second part extends these ideas to droplet and ice crystal populations with particular reference to the interaction of droplet or ice crystal growth with supersaturation and gravitational settling.

8.2. Growth of individual droplet or ice crystal

The basic equations for the heat and water budgets of a cloud droplet are:

8.2.1 Cloud droplet

HEAT $$mc.dT_r/dt = L.dm/dt - 4\pi r^2 K(dT/dr) + 4\pi r^2 \mathcal{R} \quad (1)$$

Heat input — condensation — conduction — radiation

WATER $$dm/dt = 4\pi r^2 D(d\rho_w/dr)_s \quad (2)$$

mass input — diffusion

where r = droplet radius
m = droplet mass = $4\pi\rho r^3/3$
ρ = droplet density
c = specific heat of water (4185 J $kg^{-1}deg^{-1}$)
T_r = droplet temperature
T = environment temperature
L = latent heat of evaporation (2.5 x 10^6 J kg^{-1})
K = molecular thermal conductivity of air (0.024 W m^{-1} deg^{-1})
ρ_w = vapour density in droplet environment
D = molecular diffusivity of water vapour (2.3 x 10^{-5} m^2 s^{-1})
$\mathcal{R}$ = radiative heat input per unit surface area of droplet
suffix $_s$ refers to value at droplet surface

It is shown (Annex 1) that the adjustment of the molecular diffusion fields of temperature and water vapour in the vicinity of the droplet is very rapid compared to droplet growth. Therefore it is standard practice to assume that the diffusion fields are steady state, and Eqs 1 and 2 can be rewritten in the form first given by Maxwell (1890):

$$L\rho dr/dt = (K/r)\Delta T - \mathcal{R} \quad (3)$$

$$\rho dr/dt = (D/r)\Delta\rho_w \quad (4)$$

$\Delta T = T_r - T$ = excess of droplet temperature over its environment
$\Delta\rho_w = \rho_w - (\rho_w)_r$ = excess of environment vapour pressure over that $(\rho_w)_r$ at droplet surface

Note that the sign conventions of ΔT and $\Delta\rho$ are reversed in accordance with general usage.

Combining Eqs 3 and 4 gives

$$LD\Delta\rho_w = K\Delta T - \mathcal{R}r \quad (5)$$

Eq 5 shows that, without the radiation term, the gradients of temperature and water vapour gradient near the droplet are always reversed: for droplet growth, the droplet is slightly warmer than its

environment. However, the inclusion of radiative loss ($\mathcal{R} < 0$) allo the possibility of droplet growth even if the droplet is colder th its environment. This is the normal situation in the top radiation fog and cloud where radiative cooling is dominated by t droplets, so that the principal heat sink is transferred from t atmosphere between the droplets to the droplets themselves.

Supersaturation has not yet been introduced to the abo equations. To do this, it is assumed that the vapour density at t droplet surface is just saturated at the droplet temperature - ie. $\rho_r = \rho_s(T_r)$. The vapour density difference ($\Delta\rho_w$) can then be divid into a component due to supersaturation of the environment and component due to T such that

$$\begin{aligned}\Delta\rho_w &= \rho_s(T)(1+s) - \rho_s(T_r) \\ &= \rho_s(T)[s - \Delta T(LM/RT-1)/T]\end{aligned} \qquad (6)$$

where s = fractional supersaturation
M = molecular weight of water
R = universal gas constant (8.3 J $mole^{-1}deg^{-1}$)
$\rho_s(T)$ = saturation vapour pressure at T
and the Clausius-Clapeyron relationship has been used.

Substitution of Eq 6 in Eq 4 shows that droplet growth can stil occur in the presence of slight undersaturation ($s<0$) if $\Delta T<0$. Thi is also illustrated by eliminating ΔT from Eqs 3-6 to obtain

$$dr/dt = (s/r - \mathcal{R}f(T))/g(T) \qquad (7)$$

where f(T), g(T) are slowly varying functions of temperature onl given by

$$f(T) = (LM/RT - 1)/KT \; ; g(T)=\rho[L(LM/RT - 1)/KT + RT/DMe_s(T)] \qquad (8)$$

where $e_s(T)$ = saturation vapour pressure at T

It remains to evaluate the radiation term, $\mathcal{R}$. This evaluation i based on the Mie theory of the interaction of electromagneti radiation with a spherical droplet of a specified uniform refractiv index. Dr Foot summarised the basis of this theory in Lecture 6, an its results are applied here without further comment.

8.2.1.1 Terrestrial Radiation

It has been shown (Roach 1976) that

$$\mathcal{R} = Q_a(r)\left(\tfrac{4}{2}(F^+ + F^-) - \sigma T^4\right) \text{ very nearly} \qquad (9)$$

where F^+ = upward) radiative flux across a horizontal plane
F^- = downward)
σ = Stefan-Boltzmann constant for black-body radiation
$Q_a(r)$ = mean absorption efficiency factor averaged over th intensity spectrum to which the droplet is exposed.

$Q_a(r)$ was found to be relatively insensitive to the conversio from spherical to plane parallel geometry, and to the differenc between the spectra comprising F^+ , F^- and σT^4 . For modellin purposes, it was found that the errors incurred by using
$Q_a(r) = 1.18[1 - \exp(-0.28r)]$ throughout were less than 1%.

The values of F^+ and F^- can be obtained from standard radiation transfer schemes (see Annex 2) using temperature and water vapour profiles from atmospheric models or observations using a standard radiative transfer scheme (eg. Rogers and Walshaw 1966). Typical values of $\mathcal{R}$ in the top of fog or low cloud are -30 to -50 Wm^{-2}.

8.2.1.2 Solar radiation

Absorption of solar radiation by cloud droplets has been parametrised by Slingo & Schrecker (1982) to give

$$Q_a(r) = 2(1-\omega)$$

where ω is the single scattering albedo weighted by the solar spectrum specified by Thekaekara & Drummond (1971), and the extinction cross section is assumed to be 2 since water droplets are large compared to the wavelength of solar radiation. $(1-\omega)$ is close to zero throughout the visible solar spectrum and only exceeds 0.1 at wavelengths beyond 2.5 μm. Nevertheless, this small fractional absorption may occur in the presence of solar fluxes which may reach 1.5 $kW.m^{-2}$ (upward + downward fluxes) near cloud top, and results in solar heating of cloud under a high sun not much less than long-wave cooling. There is also evidence that clouds sometimes may absorb twice as much solar energy as estimated for liquid water alone. The reality and cause of this additional absorption has not been resolved.

However, we may conclude that characteristic magnitudes of $\mathcal{R}$. are of order 30 $W.m^{-2}$ for droplets near cloud top under a high sun with no higher cloud layers above. From Eq 3, it is seen that droplet growth (or evaporation) of order 1 μm/min can be induced by radiative transfer alone. If the conduction term is of similar magnitude, then it is seen that ΔT is of order 0.01 deg.

This completes the theory of individual droplet growth with the inclusion of radiative transfer, except that for droplets of radius less than about 5 μm, additional terms for the effects of surface tension and solute in the droplet have to be included in Eq 7.

Fig 1 shows the effect of the radiation term on equilibrium values of the radius of droplets - ie. for $dr/dt = 0$ - as a function of supersaturation, s. The droplets are assumed to contain ammonium sulphate solute. Radiative cooling depresses all the curves to lower values of s. For values of solute mass greater than about 2×10^{-13}g, s remains negative for quite moderate radiative cooling.

Fig 2 shows the growth curves of droplets (solute mass 10^{-12}g) for different values of $\mathcal{R}$ for a fixed supersaturation of 0.0005. This suggests that droplet radius near cloud top at night (Curve 1) will increase at a rate of about 20 μm hr^{-1}, but within cloud during the day would level out at a value of about 8 μm.

8.2.2 Ice crystal growth

The expression for ice crystal growth in the presence of radiative transfer is formally similar to that for droplet growth, but with the addition of parameters associated with the shape of the ice crystal. Eq 8 may be written for ice crystals in the form

$$dr_i/dt = C_1 V[s_i/r_i - C_2 f_i(T)\mathcal{R}]/g_i(T) \qquad (11)$$

where r_i = radius of sphere of equal volume to the ice crystal
s_i = supersaturation with respect to ice
C_1 = shape factor relating (through C_1/r_i) to rate of mass increase as electrostatic capacity of a condenser relates to charge increase
C_2 = ratio of the surface area of the ice crystal to that of its equivalent sphere
V = ventilation factor = $1 + 0.23\sqrt{Re}$
Re = Reynolds number = $2au/\nu$
ν = kinematic viscosity of air ($\sim 10^{-5}$ $m^2 s^{-1}$ at -40 C)
u = terminal velocity
a is related to r_i through a shape factor

$f_i(T), g_i(T)$ are temperature dependent functions of the same form as $f(T)$, $g(T)$, but containing latent heat of sublimation and saturation vapour pressure with respect to ice. The shape factors C_1, C_2 were evaluated (see Appendix 2) by representing the crystals by spheroids (after Mason 1971) - prolate for bullet, column and needle crystals; oblate for short prisms and plate crystals. Heymsfield (1972) has discussed the parameters a and u as functions of crystal shape.

8.2.2.1 Terrestrial radiation

Eq 9 above applies to ice crystals as well as water droplets. $Q_a(r)$ is nearly unity since ice crystals are in general large compared to the wavelength of thermal radiation, so that the particle cross-section (whatever the shape) can be equated to $Q_a(r)$.

The value of $\mathcal{R}$ will be highly variable depending on circumstances. For thin cirrus with clear sky above and a cloud deck close beneath, cooling to space will be a maximum, $\mathcal{R} \sim -50$ $W.m^{-2}$; for cirrus streaks falling from the base of thick cirro-stratus with no cloud beneath, $\mathcal{R} \sim +50$ $W.m^{-2}$. Thin cirrus in an otherwise cloudless atmosphere will be slightly cooled radiatively in a temperate atmosphere, and slightly warmed in a tropical atmosphere.

8.2.2.2 Solar radiation

Ice becomes highly absorbing at wavelengths longer than 2.7 μm, with weak absorption bands centred near 1.55 and 2 μm. These lie in between water vapour absorption bands so do absorb some solar radiation. The total absorption of solar radiation by an ice crystal of 100 μm dimension is about 4% [ie. $Q_a(50) \sim 0.04$] so if such a crystal was exposed to a downward solar flux of 1200 $W.m^{-2}$, and (say) a reflected flux of 800 $W.m^{-2}$ from a thick cloud deck beneath, it could experience a value of $\mathcal{R}$ of ~ 80 $W.m^{-2}$ - more than offsetting cooling in thermal wavelengths. The larger the crystal, the more dominant is the solar heating.

Although Eqs 7 and 11 are formally similar, the magnitude of terms within them are very different. Eq 11 shows that zero growth rate of an ice crystal occurs if

$$s_i = C_i f_i r_i \mathcal{R} \qquad (12)$$

For 'typical' values of temperature (230 K), crystal size (r_i ~200μm), and (nocturnal) radiative loss ($\mathcal{R}$ ~ -50 W m^{-2}), it appears that s_i ~ -0.05 for needle crystals and -0.1 to -0.2 for plate crystals. This suggests that crystals could survive for some time and even grow in relative humidities (with respect to ice) of 80-90%, and could therefore settle through considerable depths in the atmosphere before evaporating. However, under a high sun, supersaturations of up to 20% might be necessary to prevent evaporation.

Rewriting the LHS of Eq 11 as $u.dr_i/dz$ and adopting a profile typical of a temperate atmosphere at night, then integrating Eq 11 for needle and plate crystals yields survival times of order 1 hr and fall distances of up to 5 km by individual crystals. This is illustrated in Fig 3. An oblate spheroidal ice crystal with an initial r_i of 0.15 mm is released from 9.5 km into an atmosphere of constant relative humidity with respect to ice. The following features are apparent:

(i) For a relative humidity of 80%, the fall distance above a cloudless atmosphere is increased by radiative loss by only 150m in about 3 km. The introduction of a cloud sheet at 6km increases the fall distance by a further 6000m - in fact the ice crystal almost reaches the cloud top.

(ii) An increase of RH to 95% more than doubles the fall distance for RH = 80% in the absence of radiation, but introducing radiative loss causes the crystal to grow slowly, and faster if there is a cloud deck beneath it. The cloud protects the ice crystal from low-level thermal radiation.

8.3 Growth of droplets or ice crystals in cloud

Growth or evaporation of droplets or ice crystals entails an exchange of water substance with the environment which will change the relative humidity of the environment. This in turn will modify droplet growth as a negative feedback mechanism: evaporation rates will be reduced by increasing relative humidity; growth rates reduced by decreasing relative humidity. The relative time-scales of these processes will depend upon cloud density and are defined by:

$$\tau_s = -s/(ds/dt); \quad \tau_r = r/(dr/dt) \qquad (13)$$

where τ_s and τ_r are relaxation times for supersaturation and droplet/ice crystal growth. The case where $\tau_r \ll \tau_s$ represents the isolated droplet/ice crystal growth discussed in Section 2 in which the effect of droplet growth on the environment was neglected. The case where $\tau_r \gg \tau_s$ represents the condition where the s-field changes much more rapidly than droplet growth and - as with the diffusion field - supersaturation quickly attains equilibrium with droplet growth. In practice, cloud droplets do not exist in isolation from their parent clouds for more than a few seconds, but (as we have seen) large ice crystals may fall some way below the base of their parent cloud.

8.3.1 Water clouds and fogs

The heat balance equation for a layer cloud in which there is no mean vertical motion can be written:

$$dT/dt = -(dF/dZ)/(\rho_a c_p) - (L/c_p)dx/dr \qquad (14)$$

where ρ_a = air density; x = vapour mixing ratio

The Clausius-Clapeyron equation may be used to further constrain the relationship between T and x:

$$dx/dt = x_s[(LM)/(RT^2)dT/dt + ds/dt] = - dw/dt \quad (15)$$

where x = saturation vapour mixing ratio
w = liquid water content (g/g of dry air)

In order to obtain a feeling for the magnitudes and time scales of the terms in Eqs 14 & 15, we assume that the fog or cloud is monodisperse, and that radiative loss in cloud top is entirely due to droplets. In fact, cooling due to water vapour and carbon dioxide only accounts for about 10% of the cooling in this situation. We then have

$$dw/dt = 4\pi r^2 N(\rho/\rho_a)(dr/dt) \quad (16)$$

and $$dF/dz = -4\pi r^2 N\mathcal{Q} \quad (17)$$

where N = droplet concentration

Taking typical values for r as 8 μm and N as 100 cm^{-3} - for which w ~ 0.2 $g.m^{-3}$ - gives a contribution to cooling in Eq 14 of order 7 K/hr. This implies that ds/dt in Eq 15 would have to be of order of 10^{-4} sec^{-1} to compete with the cooling term. A similar magnitude of dw/dt in Eq 15 implies, through Eqs 7 and 16, a value of order 10^{-4} sec^{-1} for dr/dt and -5×10^{-4} for s. Using Eq 13 implies $\tau_r >> \tau_s$. Therefore s quickly tends towards some equilibrium value which is given by putting ds/dt = 0 in Eq 15, and combining Eqs 14-17 with Eq 7 to yield:

$$s/r = \mathcal{Q}[D - AX(T)] \quad (18)$$

where $\rho X(T) = [L + (R^2 T c_p/LMx_s)]^{-1}$

Combining Eq 18 with Eq 7 leads to

$$dr/dt = - X\mathcal{Q} \quad (19)$$

Eqs 18 & 19 show that, in the absence of vertical motion of the air, droplet growth and supersaturation are controlled only by radiation and some temperature dependent coefficients.

This initial analysis, although instructive, may be misleading since it neglects the effects of droplet dispersion, gravitational settling and turbulence. Fuller treatments have been attempted by Brown & Roach (1976) and Brown (1980) in two models of radiation fog. Cloud microphysics was parametrized in the first model, but was formulated explicitly in the second.

MODEL 1.

This model is based on the thermodynamic equation and continuity equations for water vapour and liquid water, as follows:

$$\partial T/\partial t = -1/(\rho_a c_p).\partial F/\partial z + \partial/\partial z(K_h \partial T/\partial z) + LC/c_p \qquad (20)$$

$$\partial q/\partial t = \partial(K_q \partial q/\partial z)/\partial z - C \qquad (21)$$

$$\partial w/\partial t = \partial(K_w \partial w/\partial z)/\partial z + \partial G/\partial z + C \qquad (22)$$

Symbols are as in Eq 14 above with the addition of:

K_h, K_q, K_w = turbulent exchange coefficients for heat, water vapour and liquid water. These are assumed to be equal but are allowed to vary with height.

C = rate of condensation per unit mass of air

G = gravitational settling flux of liquid water

= vw, where v is a mean droplet settling speed derived from Stokes' law.

The surface heat balance forms the lower boundary condition, and the soil is assumed to be of constant thermal conductivity appropriate to sandy-clay soil with 15% water content. Condensation was automatically generated by the model whenever it detected a vapour mixing ratio above its saturation value for the local temperature.

The net radiative flux was evaluated using the equations for radiative transfer in a stratified atmosphere in the form given by Rodgers & Walshaw (1966) - see Annex 2. These equations require for their solution a knowledge of the distribution and optical transmission properties of water vapour, carbon dioxide and fog. Standard methods were used for water vapour and carbon dioxide.

The optical depth, $\mu(Z)$, of a layer of cloud or fog of physical thickness Z is given by:

$$\mu(Z) = \int_0^\infty \int_0^Z N(r,z)\pi r^2 Q_a(r)\,dr\,dz \qquad (23)$$

where N(r,z) is concentration of droplets in the radius range r to r+dr at height z.

$Q_a(r)$ was assumed to be proportional to r in this model. This introduces a factor r in Eq 23, and allows $\mu(Z)$ to be expressed solely as a function of w. This is not strictly true in view of the more accurate expression of $Q_a(r)$ quoted in Section 2a above, but it may reasonably be said that optical depth is mainly dependent on liquid water content and insensitive to drop-size distribution. It is therefore possible to parametrize the microphysical properties of cloud solely in terms of liquid water content, which greatly reduced the computational demands of this model.

This model was used to simulate a field study of the formation of radiation fog (Roach et al. 1976) and yielded the following main results:

(i) A reduction (or cessation) of turbulent diffusion resulted in earlier and thicker formation of fog. This was contrary to conventional wisdom, which required some mixing to generate fog. Condensation can result from direct radiative cooling, or by the mixing of two damp air masses at initially different temperatures. The former mechanism appears to dominate in radiation fog formation; the latter in advection of warm air over cold sea or snow, or in the breakdown of a nocturnal radiation inversion after sunrise. In the field, local wind fluctuations will result in variations in the time of fog formation. It is a common observation that fog tends to form first over damp, sheltered areas where the wind, and therefore turbulence, tends to drop out earlier.

(ii) The development of radiation fog on a realistic timescale was simulated by including the (bulk) radiative cooling due to water vapour, carbon dioxide and (when formed) fog. The fog dominated the cooling, although the cooling of individual droplets was not introduced in this model.

(iii) The inclusion of gravitational settling of droplets was necessary to simulate observed liquid water contents. The droplets in a fog initially 50 m deep would all settle to the ground in about 2 hrs, so a radiation fog is being constantly renewed. If settling was omitted, liquid water contents of 1-2 g m^{-3} were soon achieved by the model, whereas values of 0.2 g m^{-3} were observed in the field.

(iv) The nature of the underlying surface - mainly through its thermal properties - influences the time of fog formation. This will be delayed (other factors being equal) if the ground is initially warm.

MODEL 2.

The microphysics was represented explicitly in this model (Brown 1980). The fog droplets were grown on 6 different initial cloud condensation nuclei (CCN) populations. The model included expanded forms of Eqs 7,9,15 and 20-22: The droplet growth equation included allowance for droplet surface tension and solute, and for the condensation coefficient - basically the fraction of water vapour molecules colliding with the droplet which condense. Drop sizes were divided into bins of fixed width (55 bins covered the radius range 0.3-20μm) so that additional equations were required to account for transitions of droplets between size bins and height levels. The model was used to simulate the same field study as Model 1. Three experiments were carried out with the model and their results are summarised here:

Expt 1. Effect of initial CCN spectra on visibility.

Minimum visibilities of about 50 m were attained with most CCN spectra after about 3 hours. There was also an initial rapid drop from 2 km to 200 m within about 10 min about 1 hr after start of integration. Removal of large CCN had little effect, although an overall increase the concentraion of a given CCN spectrum by a factor of 5 brought minimum visibilities down to about 30m. However, a large relative increase of large CCN resulted in a much more gradual onset of fog with a final minimum visibility of about 100 m.

Reduction of the condensation coefficient from 1 to the generally accepted value of 0.033 resulted in slight reduction of mean droplet radius, but further reduction of the condensation coefficient to 0.0033 had a dramatic effect: the mean droplet size was halved and the minimum visibility reduced to 20 m. This was the only way the microphysical model could be made to simulate the old `pea-souper' of Victorian legend. This suggests that surface contamination may greatly reduce the rate of condensation on an individual droplet thus causing a much greater number of CCN to be activated. This leads to increased initial supersaturation, an increased number of smaller droplets and much lower visibility and (in the model) an increased liquid water content.

Expt 2. Comparison of Models 1 and 2.

The time of initial fog formation was a few minutes earlier in Model 2 than in Model 1, but the fog depth after 4 hours integration was 80-100 m and liquid water contents 0.4 g m^{-3} in Model 2 as compared to 20 m and 0.2 g m^{-3} in Model 1 . This difference was attributed to a higher radiative cooling and lower settling rates in Model 2 than in Model 1. In fact, Model 1 agreed better with the field results than Model 2, but the poor representation of turbulent diffusion in both models prevented any firm conclusions on the relative predictive perfomances of the two models.

Expt 3. Effect of removal of radiative loss from droplets.

The effect of removing the radiative term, $\mathcal{R}$, from the droplet growth equation was investigated, although bulk radiative cooling was retained in the heat budget equation. This is physically inconsistent, but was intended to investigate the errors resulting in the microphysical properties of the cloud. The omission of $\mathcal{R}$ has most effect on atmospheres with relatively low initial CCN counts (Fig 4). Droplet concentrations are increased by a factor of 3, liquid water content by 30% and mean drop radius reduced by 30%.

Increase of CCN concentration by a factor of 5, results in a considerable increase in the optical depth of the fog is much greater, and removal of $\mathcal{R}$ has correspondingly less effect.

Removal of $\mathcal{R}$ also increased supersaturation slightly from 0.0005 to 0.0007. It is of interest that Model 2 generated an overall positive supersaturation, where a slight negative supersaturation was predicted by the simple `monodisperse' theory. This relates to Fig 1 which shows that s remains negative only for the larger CCN. When there is wide dispersion of CCN sizes, the prevalence of small CCN results in an overall positive s.

In conclusion to this section, it appears that explicit modelling of the microphysics has added significantly to our insight into factors which may control the drop-size distribution, liquid water content, and therefore visibility. However, the need to allow for radiative transfer from indivdual droplets in bulk models oflayer cloud is less clear, particularly in situations where turbulence plays a larger role, although it is certainly necessary to parametrize droplet settling. Nicholls (1984) model of marine stratocumulus parametrizes droplet settling, but not radiative transfer from individual droplets. Expt 3

above suggests that, particularly in situations where the air-mass is likely to be of maritime origin, that Nicholls model may overestimate liquid water content and underestimate droplet settling.

8.3.2 Ice clouds

The ubiquitous presence of thin cirrus, particularly in tropical latitudes, and its effect on radiative transfer is a matter of concern to general circulation and climate modellers. In this section, we touch on two aspects of cirrus, fall-streaks and high tropical cirrus.

8.3.2.1 Cirrus fall-streaks

An early (the first?) suggestion that radiative transfer might directly affect ice-crystal growth was made by Braham & Spyers-Duran (1967) - BSD - who observed ice crystals falling up to 5 km in environmental relative humidities of order 30%. These ice crystals were 10-70 μm in size and in concentrations of 10^4-10^6 m^{-3}, and it was inferred by BSD that these crystals must originally have been about 1mm in size at the beginning of their fall.

Hall & Pruppacher (1976) - HP - developed a theory of the effect of radiative transfer on cirrus crystal growth similar to that developed above, and applied it to the BSD observations. HP concluded that radiative heat transfer changed the survival of columnar ice crystals by less than 10% if the relative humidity of the environmental air is less than 70%. This is broadly in line with our findings - but only if it is assumed that the environment is unmodified by the fall-streak.

If an analysis similar to that carried out for a population of monodisperse water droplets in Section 3a above is carried out for ice crystals, it is found that $\tau_r \sim \tau_s$ for ice crystals of the size reported by BSD for concentrations of order 1000 m^{-3}. In the concentrations observed by BSD, the theory above suggests that the air in the fall-streaks was nearly saturated. This is inconsistent with some early frost-point hygrometer observations (Goldsmith & Murgatroyd 1953, Kerley 1961) of under-saturations of up to 30%.

It seems likely that a column of ice crystals will progressively dampen an initially dry atmosphere. At first, the column will not fall far before evaporation, but will prepare the path for following ice crystals, and the streak will propagate downwards. The characteristically streamlined appearance of cirrus fall-streaks suggests that there is little turbulence within the streaks. The atmosphere within the streaks may therefore be maintained close to ice saturation, although the relative humidity of the environment is very low. This will occur whether or not there is radiative cooling.

EXAMPLE.

A cirrus fall-streak propagates downwards from a cirrus base near 300 mb into an atmosphere of relative humidity of 50%. The temperature at cloud base is -33C. The initial ice water-content is 0.05 $g.m^{-3}$ and is composed of ice crystals of equivalent radius of 0.1 mm. Assuming that temperature change due to evaporation and radiative loss is negligible, and solving for Eqs 14 and 15 above shows that the initial crystals will evaporate in about 10 mins about 300 m below cloud base,

and will raise the relative humidity at this level to about 70%. If the flux of ice crystals across 300 mb is maintained, the fall-streak will have extended to about 2 km below cloud base in 4-6 hrs (where temperature is about -20C), and evaporation will have cooled the column by about 1C on average.

The introduction of a radiative loss equivalent to $\mathcal{R} = -30$ W.m^{-2} will cause a further cooling of about 1C in about 4 hours. In fact, once an equilibrium value of supersaturation is established within the fall-streak, the ice crystals should grow at a rate given approximately by Eq 19. However, the fall-streak may in some situations be receiving thermal radiation from low levels, and may be protected from cooling to space by an overlying cirrus layer, so there may be a net radiative warming of the ice crystals within the streak.

It appears from these general considerations that although a cirrus fall-streak can occur without radiative transfer, radiation is likely to have an important effect on the development of fall-streaks, since the temperature changes so induced can be comparable to those induced by evaporation.

8.3.2.2 High tropical cirrus.

There is currently much activity - mainly in the United States - in studies of the radiative effects of cirrus, including tropical cirrus. It is generally agreed that optically thin tropical cirrus will experience net radiative heating (eg. Ackerman & Valero 1987), day or night, so the persistence of this cloud poses a problem. High tropical cirrus is unreachable by most research aircraft, and is geographically rather inaccessible so that there are few direct aircraft observations, and such as there are do not contain enough data for realistic modelling purposes. [Existing models are related mainly to the properties of temperate latitude cirrus and often appear to treat various aspects of the problem in a rather piecemeal fashion - eg. interaction of radiation and microphysics (Ramaswamy & Detweiler 1986), interaction between settling and radiation (eg. Stephens 1983). Starr & Cox (1985) give a more comprehensive treatment of the interaction between radiation, settling, microphysics, turbulence and large scale ascent.]

Some early observations of tropical cirrus near the ITCZ made from the MRF Canberra aircraft have been reported over E. Africa by Kerley (1961) and North India by Zobel & Cornford (1966). In both areas, tropical cirrus had a top near 14 km. Its thickness and cover was very variable, but some cirrus was present on over 95% of occasions. The main cirrus deck was topped by a thermally stable, nearly cirrus-free layer extending up to the tropical tropopause at 17-18 km.

The cirrus was clearly being replenished by cumulonimbus anvils spreading out beneath the thermally stable layer, but about one-third of the cirrus observed was remote from any local cumulonimbus development. The cirrus appeared to have a survival time of hours or even days, and could be carried hundreds or even thousands of km from its source by the broad easterly wind belt at these levels. This suggests that the settling rates and therefore the ice crystal sizes in persistent tropical cirrus may be much smaller than in temperate latitudes.

Finally, crystal growth/evaporation rates implied by Eq 19 at temperatures of -70C are of order 0.1 μm/hr for values of $\mathcal{R}$ of 10-20 $W.m^{-2}$. This suggests that cirrus particles could persist almost indefinitely in the high tropical tropopause, and are only dispersed by gravitational settling to lower (warmer) altitudes.

Even in the absence of comprehensive radiation and microphysical aircraft observations in high tropical cirrus, some insight may be obtained by modelling the evolution of tropical cirrus. It is proposed to attempt this by using Brown's (1980) microphysical fog model equations with suitable modifications. The main difference will be that the tropical cirrus model will be initiated with cirrus already in existence. This work has started, initially with turbulent diffusion omitted.

8.4 Conclusions

It seems likely that bulk models of cloud/radiation interaction in water clouds may not need to take account of the explicit detail of the effect of radiative transfer on the growth of individual droplets. However, this procedure may not be justified for ice cloud, where both radiative transfer and gravitational settling may need to be parametrised in bulk models. This issue remains to be settled.

Figure Legends

Fig 1. Equilibrium values of droplet radius as a function of supersaturation (s) for different values of solute mass (m) and radiative exchange (F). Each curve is labelld with F in $W\ m^{-2}$.

Fig 2. Droplet growth curves for s = 0.0005, T = 280 K and $\mathcal{R}$ = -30 (curve 1), 0 (curve 2) and +30 (curve 3) $W\ m^{-2}$.

Fig 3. Plots of ice crystal size v. height for $\mathcal{R}$ = 0 (NR); $\mathcal{R}$ = -30 $W\ m^{-2}$ above no cloud (Z_C = 0) and cloud top at 6 km (Z_C = 6).

Ackerman T P, Valero F P J & Liou K-N, 1987: Heating rates in tropical anvils. Sixth Conf.Atmos.Rad, Amer.Met.Soc.,Williamsburg, Va, USA. 13-16 May 1987, 26-29.

Barkstrom B R, 1978: Some effects of 8-12 μm radiant transfer on the mass and heat budgets of cloud droplets. J.Atmos.Sci.,35, 665-673.

Braham R R & Spyers-Duran P, 1967: Survival of cirrus crystals in clear air. J.Appl.Met., 6, 1053-1061

Brown R, 1980: A numerical study of radiation fog with an explicit formulation of the microphysics. Quart.J.R.Met.Soc., 106,781-802

Brown R & Roach W T, 1976: The physics of radiation fog: II - a numerical study. Quart.J.R.Met.Soc., 102, 335-354

Goldsmith P & Murgatroyd R J, 1953: Aircraft observations in cirrus. Met.Res.Cttee, London, MRP 833.

Hall W D & Pruppacher H R, 1976: The survival of ice particles falling from cirrus cloud in subsaturated air. J.Atmos.Sci., 33, 1995-2006

Heymsfield A, 1972: Ice crystal terminal velocities. J.Atmos.Sci., 29, 1348-1357

Kerley M J, 1961: High-altitude observations between the United Kingdom and Nairobi. Met.Mag.,London, 90, 3-18.

Mason B J, 1971: The Physics of Cloud (2nd Ed), Chap 5.8, Clarendon Press, Oxford. 671 pp.

Maxwell J C, 1890: Theory of the wet bulb thermometer, The scientiific papers of James Clerk Maxwell. Vol 2, 636-640. Dover Publications, New York.

Ramaswamy V & Detwiler A, 1986: Interdependence of radiation and microphysics in cirrus cloud. J.Atmos.Sci., 43, 2289-2301

Roach W T, 1976: On the effect of radiative exchange on the growth by condensation of a cloud or fog droplet. Quart.J.R.Met.Soc., 102, 361-372.

Roach W T, Brown R, Caughey S J, Garland J A & Readings C J (1976): The physics of radiation fog: I - a field study. Quart.J.R.Met.Soc., 102, 313-333.

Roach W T & Slingo A, 1979: A high resolution infrared radiative transfer sheme to study the interaction of radiation and cloud. Quart.J.R.Met.Soc., 105, 603-614.

Rodgers C D & Walshaw C D, 1966: The computation of infrared cooling rate in planetary atmospheres. Quart.J.R.Met.Soc., 102, 355-359.

Slingo A & Schrecker H M, 1982: On the shortwave radiative properties of stratiform water clouds. Quart.J.R.Met.Soc., 108,407-426.

Starr D O'C & Cox S K, 1985: Part I: A cirrus model. Part II: Numerical experiments on the formation and maintenance of cirrus. J.Atmos.Sci., 42, 2663-2694.

Stephens G L, 1983: The influence of radiative transfer on the mass and heat budgets of ice crystals falling in the atmosphere. J.Atmos.Sci., 40, 1729-1739.

Thekaekera M P & Drummond A J, 1971: Standard values for the solar constant and its spectral components. Nat.Phys.Sci., 229, 6-9.

Zobel R F & Cornford S G, 1966: Cloud tops over Malaya during the south-west monsoon season. Met.Mag., London, 95, 65-68.

ANNEX 1 : Scale Analysis of Eq 1

Scale analysis is the assessment of the relative magnitudes of the parameters in an equation, and of the time scales of fluctuations in these parameters. It is more convenient to express Eqs 1 & 2 in terms of droplet radius to yield:

$$L\rho dr/dt = (\rho cr/3)dT_r/dt + K(dT/dr)_s - \alpha \quad (A1)$$

$$\rho dr/dt = D(d\rho_w/dr)_s \quad (A2)$$

Characteristic time scales for droplet growth, and the difference, ΔT, between droplet temperature and its 'far field' environmental temperature can be defined as

$$\tau_r \sim r/(dr/dt); \qquad \tau_T \sim \Delta T/(dT_r/dt) \quad (A3)$$

For the first term on the RHS of Eq A1 to be of similar magnitude to the LHS requires that:

$$\tau_r \sim 3L/c\Delta T\tau_T \quad (A4)$$

Additionally, $\tau_r \sim \tau_T$ would require that $\Delta T \sim 2000K$. Since ΔT is clearly several orders of magnitude less than this, then $\tau_r >> \tau_T$, and the first term on the RHS of Eq 1 can be dropped. This is equivalent to saying that a steady-state molecular diffusion field exists around the droplet. It follows that the flux of water vapour and heat from the droplet is independent of radius, so we have:

$$\text{Heat flux} = 4\pi r^2 K(dT/dr) = \text{constant} \quad (A5)$$

Integrating Eq A5 from the droplet surface to infinity allows the conduction term in Eq A1 to be rewritten as $(K/r)(T_r - T)$ or $K\Delta T/r$. Similarly, the vapour diffusion term in Eq A2 becomes $(D/r)\Delta\rho$. Eqs A1 and A2 then assume the form given by Maxwell (1890) and appear as Eqs 3 and 4 in the main text.

ANNEX 2 : Radiative Transfer Scheme

The radiative transfer equations as set out by Rodgers & Walshaw (1966) are commonly used as the basis for computational schemes for evaluating infrared radiative fluxes and heating in stratified atmospheres. For a given section of the infrared spectrum, the transfer equations are:

$$F^{+}(z) = T(z,\emptyset)[B(g)-B(\emptyset)] + B(z) - \int_{\emptyset}^{z} T(z,z')\,dB(z')/dz'.dz' \qquad (A6)$$

$$F^{-}(z) = T(z,Z)[B(Z)-B(\infty)] - B(z) - \int_{z}^{Z} T(z,z')\,dB(z')/dz'.dz' \qquad (A7)$$

where $F^{+}(z)$, $F^{-}(z)$ are upward and downward directed fluxes of infrared radiation through level z. B(z) is the Planck function for the air temperature at height z for the relevant spectral interval. T(z,z') represents the transmission of the atmosphere between levels z and z' averaged over the spectral interval and all zenith angles. B(g) is the Planck function for ground temperature - not necessarily the same as $B(\emptyset)$.

The first term on the RHS of Eq A6 is the flux from the surface reduced by $T(z,\emptyset)$. The second term is the emission of the layer at z and the third term is the contribution from the layer of atmosphere between z and the surface. Downward flux is integrated between levels z and Z (Z>z) with a correction for downward flux through level Z.

There is a large literature on the evaluation of the transmission functions for the radiatively active gases (water vapour, carbon dioxide, ozone) in the atmosphere and for clouds which cannot be entered into here. For recent discussions, the reader is referred to Roach & Slingo (1979) for thermal radiation and Slingo & Schrecker (1982) for solar radiation.

The use of fluxes from a stratified atmosphere to evaluate the radiative transfer from a spherical droplet (Eq 9) has been shown by Roach (1976) to introduce errors of the order of 1% of $\mathcal{R}$.

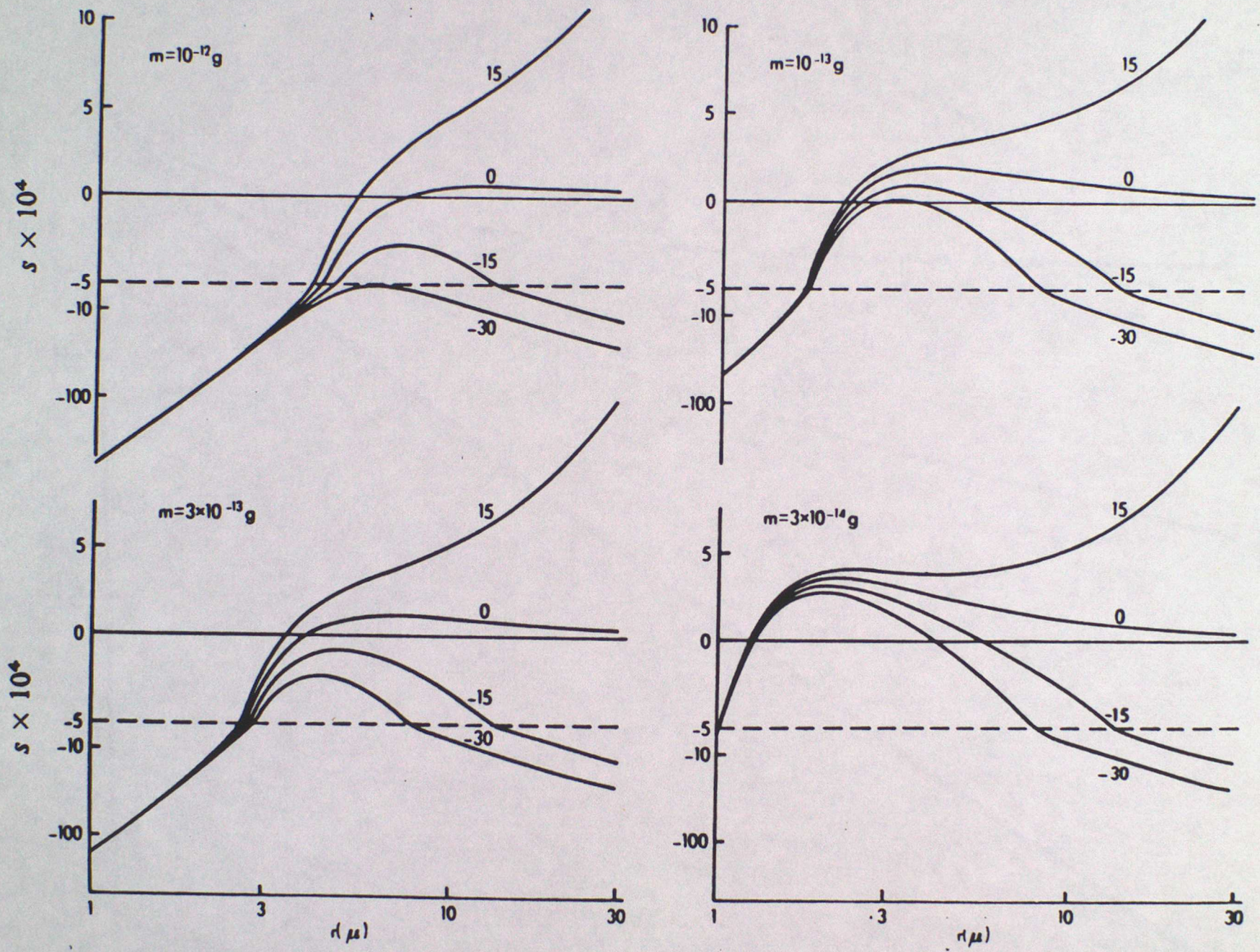
m=10⁻¹²g
m=10⁻¹³g
m=3×10⁻¹³g
m=3×10⁻¹⁴g
s × 10⁴
r(μ)
10
5
0
-5
-10
-100
15
0
-15
-30
1
3
10
30

Fig 1

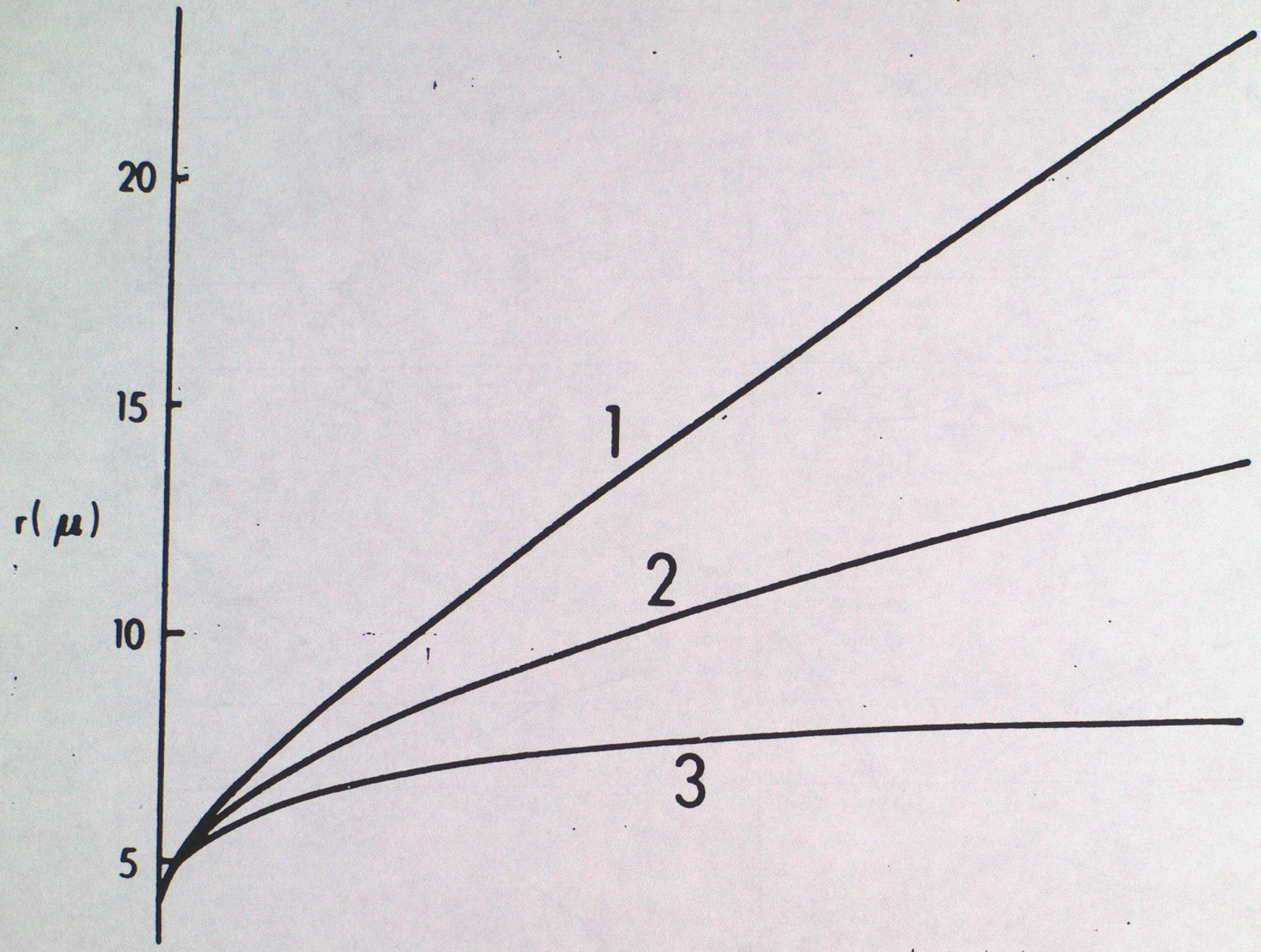

Fig 2.

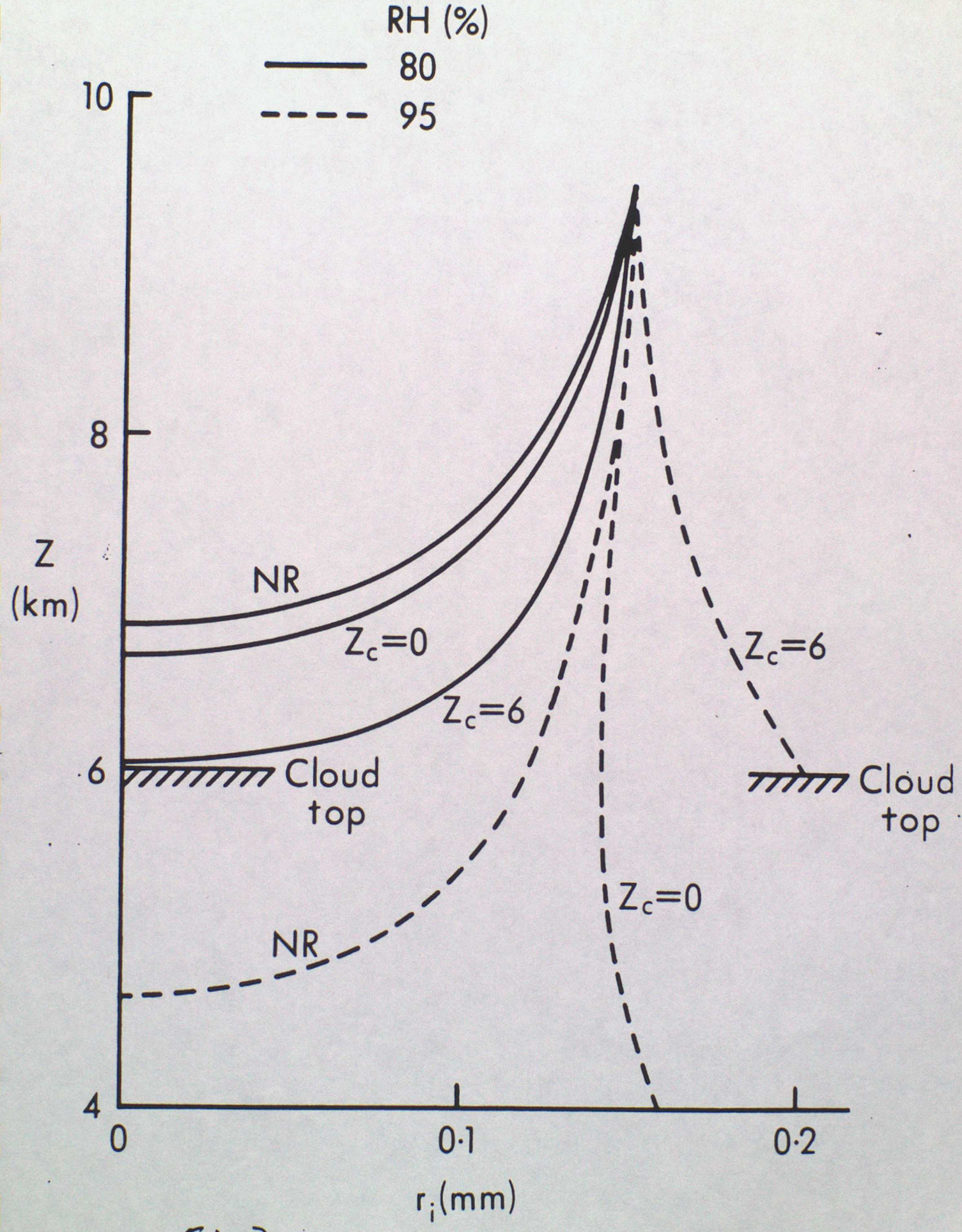
RH (%)
80
95
10
8
6
4
Z
(km)
NR
Z_c=0
Z_c=6
Z_c=6
Z_c=0
NR
Cloud
top
Cloud
top
0
0·1
0·2
r_i(mm)

Fig 3

9. RADIATION, CLOUDS AND CLIMATE

By A. SLINGO

Advanced Lecture, September 1987

9.1 THE EARTH'S RADIATION BUDGET

A convenient starting point for this lecture is the earth's radiation budget, as observed from satellites. Figures 9.1 and 9.2 show the shortwave albedo (the reflectivity of the earth–atmosphere system to the incoming solar radiation) and the outgoing longwave radiation (OLR : the thermal emission by the earth and atmosphere, which balances the absorbed shortwave radiation in the long term). These data come from the Narrow Field of View scanning radiometer mounted on the research satellite Nimbus 7 (e.g. see Hartmann et al. 1986 and references therein). The factors which contribute most to the albedo are the geometry of the earth's orbit (which determines how the incoming solar radiation is distributed), the cloud cover and the reflectivity of the underlying surface. The factors which contribute most to the OLR are the surface temperature, atmospheric temperatures and humidities and, again, the clouds.

At low latitudes, the patterns are determined primarily by the cloud distributions. For example, in the northern winter season there is strong convective activity over the Amazon and Congo basins and over Indonesia. The high, bright, cold clouds associated with the convection produce maxima on the albedo map (Fig. 9.1(a)) and minima on the OLR map (Fig. 9.1(b)). Regions where there is little cloud cover appear darker and warmer (e.g. over much of the sub–tropical oceans), because surface reflectivities are generally much lower than those of clouds and surface temperatures are generally higher than cloud–top temperatures. Important exceptions are the desert regions, especially the Sahara, which appear warm but are also bright because their sandy soils reflect more than the darker soils of surrounding cloud–free areas.

The outgoing longwave radiation decreases towards the poles, in response to the lower surface and atmospheric temperatures compared with the tropics. The shortwave albedo increases, however, because of increasing cloud cover and the higher surface albedo of snow and ice covered surfaces.

Comparison of Figs. 9.1 and 9.2 shows the shifts in the patterns with the seasons. In the tropics, the convection shifts northwards with the sun in the northern summer; for example the winter monsoon over Indonesia gives way to the Asian summer monsoon and both the Amazon and Congo basins experience (relatively) dry seasons. The albedo

thus drops over these areas and the OLR increases. In the southern hemisphere, the seasonal variations are fairly small because of the substantial area covered by ocean. In the northern hemisphere, however, the large land masses respond strongly to the seasonal insolation changes, so that the snow and ice cover are much less in summer than in winter (so the albedos are lower–Fig. 9.2(a)) and surface and tropospheric temperatures are higher (hence the higher OLR values on Fig. 9.2(b) compared with Fig. 9.1(b)).

For further discussion of the earth's radiation budget, see the paper by Hartmann et al. (1986) and the earlier reviews to which they refer.

The following two sections are adapted from Slingo and Slingo (1987a).

9.2 CLOUD RADIATIVE FORCING

Cloud–radiation interactions may be considered separately in two spectral regions, corresponding to the incoming shortwave radiation from the sun and the outgoing longwave radiation emitted by the earth–atmosphere system. In the shortwave, clouds reflect solar radiation back to space and thus cool the system (the "albedo" effect). In contrast, since cloud top temperatures are generally lower than those of the underlying atmosphere and surface, clouds reduce the outgoing longwave radiation and hence enhance the greenhouse warming of the system. A determination of the net radiative effect of clouds on climate thus requires quantification of these two opposing forcings.

Analyses of model output and satellite data to determine the effect of clouds on the radiation budget (and hence also estimate the cloud feedback, see section 9.4) have traditionally involved the sensitivity parameter δ, which is the partial derivative of the net radiation with respect to the cloud amount (e.g. Hartmann et al. 1986). While this seems a logical definition, in practice it is fraught with problems because of the need to know the cloud amount, which is a notoriously difficult quantity to determine accurately from observations. Additionally, the techniques used to define the cloud amount and the assumptions regarding the cloud radiative properties may be quite different between observational studies and models, or between different models. Comparison of values of δ from different sources can thus be very misleading. What is needed is a parameter which does not require explicit knowledge of the cloud amount. A simple analysis fulfilling this requirement was proposed by V. Ramanathan (Charlock and Ramanathan 1985, Hartmann

et al. 1986, Ramanathan 1987). For a region in which there is partial cloud cover, the effect of clouds on some area–mean radiative flux is simply taken to be the difference between that flux and its value for clear skies. The sign of the difference is changed so that implied heating appears as a positive quantity. This difference is called the cloud radiative forcing. For many purposes this is a more useful parameter than δ, because it gives the effect of clouds directly in energy units. It can also be derived with some confidence from satellite data because it is much easier to derive the clear–sky flux than the cloud amount.

Following Ramanathan (1987), let F be the area–mean radiative flux (in W m^{-2}) at the top of the atmosphere reflected by, or emitted from, a region with partial cloud cover and let F_c be the flux for clear skies. Then the cloud radiative forcing C_f is

$$C_f = F_c - F \tag{9.1}$$

It is convenient to consider the cloud radiative forcing separately in the shortwave and longwave spectral regions. Diagnostics are shown from a control integration for perpetual January conditions of a new version of the Community Climate Model ("CCM1"), developed at the National Center for Atmospheric Research ("NCAR"), in the United States. The original version ("CCM0") and results from simulations with it were described by Pitcher et al. (1983) and Ramanathan et al. (1983). Williamson et al. (1987) describe in detail the changes which were incorporated into CCM1.

The same cloud forcing diagnostics are being archived from the Earth Radiation Budget Experiment (ERBE Science Team 1986). When these data become generally available, starting at the end of this year, it will be possible to carry out a much more detailed validation of the performance of models in the areas of clouds and radiation than has previously been possible. The key has been the archival of estimates of the clear–sky fluxes and ERBE is the first radiation budget experiment to have included these as standard.

9.2.1 Cloud shortwave forcing

The cloud shortwave forcing, $C_f(S)$, is

$$C_f(S) = S(\alpha_c - \alpha) \tag{9.2}$$

where S is the incoming solar flux, α is the albedo and α_c is the albedo for clear skies. Maps of α, α_c and $C_f(S)$ from the control experiment are shown in Fig. 9.3. The albedo α may be compared with the Nimbus 7 data shown in Fig. 9.1(a). The modelled distribution is in reasonable agreement with the satellite data, although there are some deficiencies which were also present in an earlier version of the model (Charlock and Ramanathan 1985, their Fig. 7). In the tropics, the albedo maxima over the regions of deep convection are weaker than in the Nimbus 7 data. The albedo minima over the sub–tropical oceans are too close to the western coasts of South Africa and South America. In reality, there are extensive sheets of stratus and stratocumulus over the cool water adjacent to the coasts, with clearer skies to the west, but in the model this pattern is reversed. Problems with the representation of such cloud sheets are a common feature of current models (ECMWF 1985). It is demonstrated in Slingo and Slingo (1987b) that in the CCM this error may be corrected by replacing the cloud prediction scheme by that developed for the ECMWF model (J. M. Slingo 1987). Finally, the albedos are also too low in the southern hemisphere mid–latitudes. As above, this is due to cloud amounts which are too low, which may be a consequence of the serious underestimate of the strength of lows in the southern hemisphere depression belt which is a feature of the model when run with low horizontal resolution (e.g. Pitcher et al. 1983). The globally–averaged albedo is 29.8 per cent, which compares favourably with satellite data (Hartmann et al. 1986, their Table 1).

The clear–sky albedo α_c (Fig. 9.3(b)) is generally much smaller than α at low latitudes, because the albedo of the underlying surface is much lower than that of clouds. One obvious exception is the relatively high reflectivity of the North African deserts. At high latitudes, however, the surface albedo is generally large due to snow cover and sea–ice, so the contrast between the two maps is less evident.

The cloud shortwave forcing $C_f(S)$ (Fig. 9.3(c)) is everywhere negative, corresponding

to the cooling of the system by the albedo effect. The globally–averaged value is -51.1 W m^{-2}. The forcing is a maximum over the southern hemisphere mid–latitudes, which is where both the insolation and the cloud cover are large. As noted above, the model underestimates the cloud cover in this region, so the values of cloud forcing should actually be larger than those shown here.

Apart from cloud reflection, the atmosphere is relatively transparent to shortwave radiation, so the cloud shortwave forcing is felt primarily at the surface rather than within the atmosphere (e.g. Ramanathan 1987). Figure 9.3(c) shows that, in this season, most of the forcing is over the southern oceans. In the northern summer, the forcing is larger over the northern continents, but it is also significant over the northern and tropical oceans. In order to investigate the effect of this forcing on climate, one would therefore need a coupled ocean–atmosphere model, so that sea surface temperatures (SSTs) were calculated rather than prescribed, as otherwise the response would be misleadingly small.

9.2.2 Cloud longwave forcing

The cloud longwave forcing, $C_f(L)$, is

$$C_f(L) = OLR_c - OLR \tag{9.3}$$

where OLR is the outgoing longwave radiation and OLR_c is the value for clear skies. Maps of OLR, OLR_c and $C_f(L)$ are shown in Fig. 9.4. As with the shortwave albedo, the OLR map (Fig. 9.4(a)) may be compared with Nimbus 7 data (Fig. 9.1(b)). The modelled OLR distribution agrees well with the Nimbus 7 data and the global average of 239.8 W m^{-2} also falls within the range of the satellite measurements (Hartmann et al. 1986, their Table 1). The minima in the tropics over South America, South Africa and Indonesia are located correctly, although the central values are not as low in the model as in these observations. Over the tropical oceans there are some areas where the OLR exceeds 300 W m^{-2}, which is probably the result of insufficient cloud cover, as these are also the regions where the shortwave albedo is too low.

Comparison between the OLR distribution and that for clear skies (Fig. 9.4(b)) shows differences which are similar to those seen earlier in the albedos. In the tropics, the value

of OLR_c is typically about 300 W m^{-2} and is less near the poles due to the lower surface and atmospheric temperatures. At high northern latitudes, the values are lowest over the cold continents and largest over the relatively warm North Atlantic ocean. The greatest contrast between Figs. 9.4(a) and 9.4(b) is therefore in those regions where persistent high (and therefore cold) cloud is found above a warm surface, that is in the areas of deep tropical convection and in the North Atlantic storm track. These are the regions which show the largest values of the cloud longwave forcing (Fig. 9.4(c)), as was also noted by Hartmann et al. (1986).

The longwave forcing is positive everywhere, showing that clouds warm the system by enhancing the greenhouse effect. The globally–averaged value is 30.2 W m^{-2}. Since this is lower than the average shortwave forcing, the net effect of clouds in this model is to cool the system, which is in broad agreement with the results from other models (Cess and Potter 1987).

Of particular importance in the distribution of longwave forcing is the fact that the largest values coincide with the areas of deep tropical convection. This coincidence suggests that there may be important interactions between the forcing and the convection, which is of course responsible for most of the cloudiness in these regions. Before considering those interactions, however, it is first necessary to consider the partitioning of the longwave forcing between the surface and atmosphere.

9.2.3 Cloud longwave forcing of the surface and atmosphere

The effect of clouds on longwave heating rates may be understood by considering Fig. 9.5. This shows schematically the perturbation of the fluxes and heating rates produced by high and low clouds inserted into two extreme atmospheric profiles. The calculations were made with the radiation scheme incorporated into the U. K. Meteorological Office model, as described by Slingo and Wilderspin (1986). The scheme was run first for clear skies, followed by runs with complete cover by low and then high cloud, the latter being of course considerably lower in the sub–arctic winter profile than in the tropical profile because of the shallower troposphere. The emissivity of low cloud was taken to be unity (i.e. the clouds act as black bodies), whereas that of high cloud was assumed to be 0.5. A

value smaller than unity is implemented simply by multiplying the cloud amount by the emissivity.

The changes in the OLR produced by the clouds are listed at the top of Fig. 9.5, while the changes in the downward longwave radiation at the surface are given at the bottom of the figure. Consider first the OLR. Since temperature generally decreases with height, the temperature of a cloud top is usually less than that of the underlying atmosphere and surface, so the longwave emission from the cloud top is smaller than the upward flux in a clear atmosphere at the same level. The OLR is thus reduced by the presence of cloud, giving rise to greenhouse warming of the earth–atmosphere system. The magnitude of the OLR decrease depends on the difference in temperature between the cloud top and the atmosphere and surface below, and so is largest for the high (cold) cloud in the tropical atmosphere and is smallest for the low cloud in the sub–arctic winter atmosphere, where the cloud top temperature is almost the same as that of the surface.

A similar argument applies to the downward radiation at the surface. Cloud base emission is generally higher than the downward flux from a clear atmosphere at that level, so clouds increase the downward radiation and warm both the atmosphere below cloud base and the surface. The surface warming is greatest for low clouds, because for these the differential between clear and cloudy regions is greatest. It is also larger in the sub–arctic winter profile than in the tropical profile, because the atmosphere in this case has a much smaller water vapour content and is thus more transparent. Hence there is a greater contrast between the downward radiation in clear and cloudy skies, as well as less damping of that contrast by the water vapour emission and absorption below cloud base.

Substantial changes are also produced in the heating rates at the level of the clouds. Cloud tops are cooled because their emission exceeds that incident from above. This cloud top cooling has only a weak dependence on the cloud height. On the other hand, cloud bases are warmed because the atmosphere and surface below are at higher temperatures. This warming is strongly dependent on the cloud height; as the cloud is raised so the temperature differential increases. For most clouds the cloud top cooling exceeds the cloud base warming, so that a net cooling is produced locally. However, for high clouds in a tropical atmosphere the cloud base warming can be several tens of degrees K per day

(e.g. Webster and Stephens 1980). For cloud bases above about 10 km, the warming of the base thus exceeds the cooling of the top, so there can be a net warming of the cloud layer (e.g. Paltridge and Platt 1976, Figure 10.9).

In summary, in the longwave spectral region clouds warm both the earth–atmosphere system and the surface . Cloud bases warm and cloud tops cool. Most clouds cool the atmosphere locally, but warm the atmosphere below cloud base. High tropical clouds are sufficiently cold that they can warm the atmosphere locally.

The above discussion clarifies the partitioning of the cloud longwave forcing between the surface and the atmosphere. In a model it is obviously a simple matter to repeat the calculation in equation 9.3 for the downward longwave radiation at the surface and so derive the cloud longwave forcing of the surface, which is shown in Fig. 9.6(a). The values are everywhere positive so that, as explained above, clouds warm the surface. The warming is greatest at high latitudes and smallest at low latitudes, where the substantial water vapour mixing ratios in the boundary layer damp the impact of clouds on the surface fluxes (e.g. Feigelson et al. 1982).

The difference between the cloud longwave forcing at the top of the atmosphere and that at the surface gives the cloud longwave forcing of the atmosphere itself, which is shown in Fig. 9.6(b). Note that over most of the globe clouds cool the atmosphere, as expected from the earlier discussion. However, the presence of extensive sheets of high cloud over regions of tropical convection produces a significant warming in these regions. Comparison of Figs. 9.4(c) and 9.6(b) shows that in these regions the majority of the cloud longwave forcing is felt within the atmosphere, rather than at the surface. This result is important, for three reasons. Firstly, it indicates that there must be a direct interaction between the convective heating and the cloud longwave forcing, because both occur within the atmosphere where there is deep convection. Secondly, the peak values of the cloud longwave forcing of the atmosphere over Indonesia exceed 80 W m^{-2}. Even if this heating were spread throughout the troposphere (which is unlikely), the mean diabatic heating from this term would be about 1 K/day, which is by no means negligible compared with the latent heat release by convection (Ramanathan 1987). Thirdly, it should be possible to study the effect of this forcing on atmospheric convection and dynamics with a model

incorporating prescribed SSTs, which is tantamount to ignoring the cloud longwave forcing of the ocean surface. Such a study has recently been carried out with CCM1 by Slingo and Slingo (1987a,b) and selected results are shown in the next section.

9.3 EFFECT OF CLOUDS ON PRESENT-DAY CLIMATE

9.3.1 Surface temperatures

From the above discussion, one would expect clouds to produce a cooling of the surface in the shortwave and a warming of the surface in the longwave. This agrees with common experience; near-surface temperatures are generally lower in the daytime when skies are cloudy rather than clear, but they are higher at night. The *net* effect depends on the relative magnitudes of these opposing forcings, and hence on both latitude and time of year (because these control the daily-mean insolation), as well as on the cloud heights and radiative properties. Stephens and Webster (1981) explored these factors and some of their results are illustrated in Fig. 9.7. At 35^0 N, the shortwave effects dominate for low and middle level clouds, which thus cool the surface. On the other hand, high clouds generally have much lower liquid (or ice) water contents and for such clouds the albedo is smaller than that for clouds at low levels, while the longwave emittance is only slightly smaller (e.g. consider a cloud with a liquid water path (LWP) of 20 g m^{-2} on Fig. 9.8(a)). Such clouds therefore tend to warm the surface because the longwave forcing is dominant. Figure 9.7(b) shows that all clouds warm the surface at high latitudes in winter, when shortwave effects are weak. The dependence on LWP is particularly strong for values less than about 50 g m^{-2}, as one would expect from Fig. 9.8(a).

9.3.2 Atmospheric circulations

Given the magnitude of the radiative forcing by clouds, it seems reasonable to expect that they may affect the atmospheric circulation. The first study of the effect of clouds on the general circulation was performed by Hunt (1978) , who integrated a hemispheric model with annual-mean external forcing and studied the effect of removing zonally-averaged clouds from the radiative computations. Surface and tropospheric temperatures increased, due to the dominance of the shortwave effects, but there were only small changes in the zonally-averaged circulation. This result has been criticised as misleading, however, as a number of possibly important feedbacks were suppressed by assuming a flat earth

with no land–sea contrast and through the use of fixed water vapour and surface albedo distributions (G. E. Hunt et al. 1980).

Satellite observations of the earth's radiation budget show that there are substantial asymmetries in the cloud distribution, so the assumption of zonally–meaned cloudiness in Hunt's study is also unrealistic. To study the effect of such asymmetries, Meleshko and Wetherald (1981) compared an integration of the GFDL spectral model for northern summer conditions and imposed zonally–meaned cloudiness, with one in which a geographical cloud distribution was used. In the latter experiment, the cloud cover was reduced over most land areas and increased over the oceans compared with the first integration. Over land, both the solar insolation and surface longwave cooling were thus increased, although the former was dominant. Land surface temperatures rose by 2–4 K, enhancing the continental heat lows and modifying the wind and precipitation patterns. These changes were induced by the increased asymmetry in the distribution of diabatic heating in the second experiment. The sea surface temperatures were fixed, so these results are applicable only for time–scales over which this restriction is valid, corresponding roughly to the 30 days over which the differences were computed. The potential climatic impact of the different cloud distributions was thus under–estimated, since in reality the increased cloud cover over the oceans would cool the sea surface and thus enhance the land–sea contrast still further.

In addition to geographical variations in cloudiness, there are of course also temporal variations associated with synoptic systems. Shukla and Sud (1981) investigated the importance of such changes by comparing an integration of the GLAS model for northern summer conditions in which the cloud cover was predicted (and hence varied in time) with one in which the mean cloud distribution from this run was imposed. There were significant differences between the two integrations, indicating that temporal variations in the cloud cover influenced the model's circulation. With the imposed cloud distribution, the fixed asymmetric thermal forcing increased the generation of eddy available potential energy and its conversion to eddy kinetic energy. At 50^{o}N, the stationary component of the 500 mb height variance was also increased.

Letreut and Laval (1984) performed an experiment which combined features of each

of the above. They compared January and July control integrations having prescribed, zonally–meaned cloudiness with runs in which the cloud cover was interactively predicted by the model. As found by Meleshko and Wetherald, many of the most significant changes in the simulations were produced over the oceans, presumably being remotely forced by changes in the surface energy budget over the continents. The simulation of precipitation and evaporation patterns were generally more realistic in the integrations with interactive cloud. Letreut and Laval found a similar sensitivity of the atmospheric energy cycle to the cloudiness as was obtained by Shukla and Sud, with an increase of the transient eddy kinetic energy when the cloudiness was interactive.

In the above studies, many of the changes were caused by the effect of clouds on the incoming shortwave flux at the surface, enhancing the thermal forcing of the land surface and thus indirectly changing tropospheric temperatures and the general circulation. In contrast, Ramanathan et al. (1983) demonstrated that cloud longwave interactions within the atmosphere had a profound impact on the circulation in CCM0. Altering the emissivity of high cloud and the number of model layers in which it was allowed to form changed the zonally–meaned temperature of the tropical upper troposphere by over 5 K. This enhanced the equator–to–pole temperature gradient and so, through the thermal wind relationship, there was a corresponding acceleration of the sub–tropical jets by up to about 9 ms^{-1}. Each of these changes represents a substantial impact of clouds on the model's circulation.

9.3.2.1 Results from Slingo and Slingo (1987a). This paper examines the importance of the cloud longwave forcing of the atmosphere, by comparing a control integration of CCM1 (cf Figs. 9.3, 9.4 and 9.6) with one in which the forcing was removed (by replacing the atmospheric longwave heating rates by their clear–sky values).

The simulations of the zonal–mean temperatures and winds in the control experiment are shown in Figure 9.9. Apart from a cold bias by a few degrees in the tropical troposphere, these are realistic. The effects of the forcing on the zonal–mean temperatures and winds are shown in Fig. 9.10, together with the associated t–statistics. The forcing produces a warming of the tropical upper troposphere, which is highly significant. The lower stratosphere is cooled, because the high clouds reduce the upward longwave fluxes which contribute to the radiative heating. The net effect is thus a significant destabilisation of

the upper troposphere by the cloud longwave forcing. There is a strong warming of the north polar stratosphere, but this is not statistically significant as the natural variability in this region in January is substantial. The expected cooling of the upper troposphere at high latitudes may also be seen, particularly over the south pole where the cloud cover exceeds 25 %.

The zonal–mean wind differences (Fig. 9.10(b)) show a substantial and highly significant acceleration of both sub–tropical jets. As with the temperature differences, the deceleration in the north polar stratosphere is not significant. The difference field for the 200mb winds (Fig. 9.11(b)) shows that the acceleration of the jets is fairly uniformly distributed in longitude in the southern hemisphere. However, in the northern hemisphere the acceleration is located preferentially in the vicinity of the jet maxima (Fig. 9.11(a)). The effect is particularly large for the Atlantic jet, the magnitude of the perturbation representing a significant fraction (roughly one third) of the jet strength in the control.

The preferential acceleration of the Atlantic jet compared with that over the Pacific is asociated with a strong and statistically significant anomaly pattern in the 200mb geopotential height (Fig. 9.12). In the northern hemisphere, cloud forcing results in a deep negative anomaly centred over Newfoundland, with a smaller anomaly near the dateline. In the tropics, the warming of the troposphere shown in Fig. 9.10(a) increases the heights by on average about 100m. This is a large change compared with the variability of tropical temperatures on the 90–day timescale, hence the large values of t in Fig. 9.12(b). The juxtaposition of a height maximum over the Atlantic at about 25^0 N and the negative anomaly to the north gives rise to a strong height gradient at 40^0 N, which is another manifestation of the acceleration of the jet. The height changes are much smaller in the high latitudes of the southern hemisphere and are not statistically significant.

Such barotropic patterns have been generated in modelling studies of the atmospheric response to sea surface temperature (SST) anomalies (e.g. Blackmon et al. 1983, Geisler et al. 1985, Palmer and Mansfield 1986a,b). The driving mechanism for these patterns is believed to be changes in the distribution of diabatic heating over the tropical Pacific, associated with changes in the distribution of precipitation forced by the SST anomalies. It is generally assumed that the anomalous diabatic heating comes from variations in the latent

heat release (i.e. the precipitation changes themselves). However, the results shown here demonstrate that cloud longwave forcing is equally capable of generating height anomalies of this magnitude, although some of the change in the diabatic heating comes from changes induced in the precipitation field. Nevertheless, precipitation changes must be associated with changes in the distribution of cloudiness, so they must also produce changes in the cloud forcing. One may conclude that changes in cloud forcing are an inevitable and potentially important component of the changes in diabatic heating produced by SST anomalies. This possibility does not seem to have been widely recognised in previous studies.

9.3.2.2 Discussion. These results confirm that cloud radiative forcing is an important component of the atmospheric response to an applied perturbation, such as that provided by a sea surface temperature anomaly. Much of the response appears to be due to the forcing by high cloud in the tropics. The response is complicated by strong interactions between the forcing and the latent heat released by convection and large scale condensation. The cloud radiative forcing and the forcing by latent heat release are thus intimately related.

There is much supporting evidence from both observational and theoretical studies that the radiative forcing by high cloud has an important influence on tropical convection and dynamics. Data for the Indonesian region obtained during the Winter Monsoon Experiment (WMONEX) show that extended sheets of upper–tropospheric cloud are a common feature (Webster and Stephens 1980). These cloud layers produce substantial perturbations to the local radiative heating profile, particularly in the longwave spectral region. Such perturbations are significant when compared with the diabatic heating associated with latent heat release. Houze (1982) showed that the extensive upper cloud layers are associated with the mature and later stages in the development of a tropical cloud cluster. Radiative and condensational heating within the cloud and evaporative cooling of precipitation at lower levels combine to modify the heating profile from the main updraught regions, with increased heating at upper levels. As a result, the vertical motion field on the scale of the cloud cluster, which in the mean balances the heating, is also modified. Hartmann et al. (1984) showed that when such a modified heating profile was used to force a linear model, it led to a marked improvement in the simulation of the east–west Walker circulation, compared with when a profile more typical of just the deep

convective elements was used. The results of Slingo and Slingo (1987a,b) demonstrate that the radiative forcing is also capable of influencing the circulation on the largest scales, with appreciable effects on the flow fields at high latitudes.

9.4 CLOUDS AND CLIMATE CHANGE

Much of the interest in the possible impact of cloud–radiation interactions on climate has come from the need to reduce uncertainties in climate–change experiments. Climate can change due to a variety of external influences (e.g. variations in the sun's output or in the earth's orbit) or internal factors, the one attracting the most attention at the present time being the increasing concentrations of the greenhouse gas carbon dioxide (CO_2). Such perturbations may be amplified or damped by feedback mechanisms. For example, increases in CO_2 warm the planet, increasing the atmospheric water vapour content. Water vapour is the most important greenhouse gas so the result is a positive feedback enhancing the initial perturbation. Changes in cloudiness can also in principle make a contribution, which is generally referred to as the "cloud feedback". It is important to distinguish this from the cloud forcing, which acts at all times, even if there are no changes in the clouds and hence no cloud feedbacks.

Using a simplified sector model with an idealized land–sea distribution, Wetherald and Manabe (1980) ran two versions, one with model–generated cloudiness and a second with imposed cloud distributions, and compared the sensitivity of each version to different values of the solar constant. In the first set of experiments the cloud distributions changed in response to the external forcing, but the sensitivity of the model was very similar to that in the second set of experiments. This was due to a compensation between the effect of clouds in the shortwave and longwave regions. Wetherald and Manabe concluded that cloud feedbacks were unimportant, but in subsequent investigations with a global model and realistic geography, they found that cloud feedbacks enhanced the sensitivity of the surface temperature to doubled CO_2 by about 30 per cent (Wetherald and Manabe 1986). This brought them into agreement with the results discussed by Hansen et al. (1984). In both studies, the enhanced warming was produced by increases in the amount of high level cloud in the tropics, leading to a reduction in the outgoing longwave radiation and hence amplification of the initial warming.

Despite the agreement between these two studies, however, they ignore the potentially important changes in cloud radiative properties which might also take place. Figure 9.8 demonstrates that for water clouds those properties depend on both the cloud liquid water path LWP (a,b) and the equivalent radius of the drops r_e (c), which is a measure of the mean drop size. Both parameters could vary during a period of climate change.

Firstly, in a CO_2–warmed climate, one might expect the greater water vapour mixing ratios to lead to increased cloud liquid water contents. Figure 9.8(a) shows that for clouds with LWP greater than about 50 g m^{-2} the change in the longwave effective emittance is small, but the cloud albedo is still increasing with LWP. A higher albedo means that more solar radiation is reflected back to space, so this would act as a negative feedback. Estimates by Somerville and Remer (1984) indicate that this negative cloud optical property feedback might be as important as the positive cloud amount feedback in the CO_2 problem.

Secondly, there is no guarantee that climate change would not be accompanied by changes in the number of Cloud Condensation Nuclei (CCN) in the atmosphere, due to either natural processes or increasing pollution. Over land, CCN concentrations are high so there is no lack of nuclei for initiating cloud droplet growth . Over the sea, however, CCN concentrations are much lower and so variations can have a significant impact on cloud droplet spectra. If CCN concentrations were to increase over the oceans, this could therefore lead to more drops being formed for a given supersaturation. If the LWP remained the same, r_e would decrease and so from Fig. 9.8(c) the cloud albedo would increase. Increasing CCN concentrations could therefore act as an negative feedback in addition to that from the LWP. This possibility has recently been discussed by Charlson et al. (1987) in connection with the role of oceanic phytoplankton and is a good example of the growing appreciation that biological systems may play an important role in climate change.

From the above I hope it will be clear that we have only begun to appreciate some of the complexities regarding the contribution of clouds to climate change. A great deal more work is needed in many fields. Further sensitivity experiments with general circulation models are needed to assess the potential importance of the various cloud feedbacks. The theoretical and experimental foundations for the hypothesized changes in cloud amounts

and optical properties are very tenuous, so more observations are certainly needed. Global datasets from satellite experiments such as ERBE and ISCCP (Schiffer and Rossow 1985) will be useful in developing improved relationships between cloud amounts and radiative properties and the large–scale variables. More *in situ* aircraft data are also needed to provide validation for the satellites and, for example, to determine if there really is a relationship between the cloud liquid water content and large–scale variables such as temperature.

REFERENCES

Blackmon, M. L., Geisler, J. E. and Pitcher, E. J. 1983 A general circulation model study of January climate anomaly patterns associated with interannual variation of equatorial Pacific sea surface temperatures. *J. Atmos. Sci.* , **40**, 1410–1425

Cess, R. D. and Potter, G. L. 1987 Exploratory studies of cloud radiative forcing with a general circulation model. *Tellus* , submitted for publication

Charlock, T. P. and Ramanathan, V. 1985 The albedo field and cloud radiative forcing produced by a general circulation model with internally generated cloud optics. *J. Atmos. Sci.* , **42**, 1408–1429

Charlson, R. J., Lovelock, J. E., Andreae, M. O. and Warren, S. G. 1987 Oceanic phytoplankton, atmospheric sulphur, cloud albedo and climate. *Nature* , **326**, 655–661

ECMWF 1985 *Workshop on cloud cover parameterization in numerical models, 26–28 November 1984*. ECMWF, Shinfield Park, Reading, England

ERBE Science Team 1986 First results from the Earth Radiation Budget Experiment (ERBE). *Bull. Amer. Met. Soc.* , **67**, 818–824

Feigelson, E. M., Kondratyev, K. Ya. and Prokofyev, M. A. 1982 'Radiation processes and their parametrization'. Pp 389–466 in *The GARP Atlantic Tropical Experiment (GATE) Monograph*. GARP Publications Series No. 25, WMO, Geneva

Geisler, J. E., Blackmon, M. L., Bates, G. T. and Muñoz, S. 1985 Sensitivity of January climate response to the magnitude and position of equatorial Pacific sea surface temperature anomalies. *J. Atmos. Sci.* , **42,** 1037–1049

Hansen, J., Lacis, A., Rind., D., Russell, G., Stone, P., Fung, I., Ruedy, R. and Lerner, J. 1984 'Climate sensitivity: analysis of feedback mechanisms'. Pp. 130–163 in *Climate Processes and Climate Sensitivity*, (Ed. J. E. Hansen and T. Takahashi). Geophysical Monograph 29, American Geophysical Union

Hartmann, D. L., Hendon, H. H. and Houze, R. A. 1984 Some implications of the mesoscale circulations in tropical cloud clusters for large–scale dynamics and climate. *J. Atmos. Sci.* , **41,** 113–121

Hartmann, D. L., Ramanathan, V., Berroir, A. and Hunt G. E. 1986 Earth Radiation Budget Data and Climate Research. *Rev. Geophys.*, **24,** 439–468

Houze, R. A. 1982 Cloud clusters and large–scale vertical motions in the tropics. *J. Met. Soc. Japan* , **60,** 396–409

Hunt, B. G. 1978 On the general circulation of the atmosphere without clouds. *Quart. J. R. Met. Soc.* , **104,** 91–102

Hunt, G. E., Ramanathan, V. and Chervin, R. M. 1980 On the role of clouds in the general circulation of the atmosphere. *Quart. J. R. Met. Soc.* , **106,** 213–215

Le Treut, H. and Laval. K. 1984 'The importance of cloud–radiation interaction for the simulation of climate'. Pp 199–221 in *New perspectives in climate modelling*, (Ed. A. L. Berger) . Developments in Atmospheric Science, **16,** Elsevier

Meleshko, V. P. and Wetherald, R. T. 1981 The effect of a geographical cloud distribution on climate: a numerical experiment with an atmospheric general circulation model. *J. Geophys. Res.* , **86,** 11995–12014

Palmer, T. N. and Mansfield, D. A. 1986a A study of wintertime circulation anomalies during past El Niño events using a high resolution general circulation model. I : Influence of model climatology. *Quart. J. R. Met. Soc.* , **112**, 613–638

1986b A study of wintertime circulation anomalies during past El Niño events using a high resolution general circulation model. II : Variability of the seasonal mean response. Quart. J. R. Met. Soc. , **112**, 639–660

Paltridge, G. W. and Platt, C. M. R. 1976 *Radiative processes in meteorology and climatology.* Developments in Atmospheric Science, **5**, Elsevier

Pitcher, E. J., Malone, R. C., Ramanathan, V., Blackmon, M. L., Puri, K. and Bourke, W. 1983 January and July simulations with a spectral general circulation model. *J. Atmos. Sci.* , **40**, 580–604

Ramanathan, V. 1987 The role of earth radiation budget studies in climate and general circulation research. *J. Geophys. Res.* , **92**, 4075–4095

Ramanathan, V., Pitcher, E. J., Malone, R. C. and Blackmon, M. L. 1983 The response of a spectral general circulation model to refinements in radiative processes. *J. Atmos. Sci.* , **40**, 605–630

Schiffer, R. A. and Rossow, W. B. 1985 ISCCP global radiance data set: a new resource for climate research. *Bull. Amer. Met. Soc.* , **66**, 1498–1505

Shukla, J. and Sud, Y. 1981 Effect of cloud–radiation feedback on the climate of a general circulation model. *J. Atmos. Sci.* , **38**, 2337–2353

Slingo, A. and Schrecker, H. M. 1982 On the shortwave radiative properties of stratiform water clouds. *Quart. J. R. Met. Soc.* , **108**, 407–426

Slingo, A. and Slingo, J. M. 1987a The response of a general circulation model to

cloud longwave radiative forcing. I : Introduction and initial experiments. Quart. J. R. Met. Soc. , submitted for publication

Slingo, A. and Wilderspin, R. C. 1986 Development of a revised longwave radiation scheme for an atmospheric general circulation model. *Quart. J. R. Met. Soc.* , **112**, 371–386

Slingo, J. M. 1987 The development and verification of a cloud prediction scheme for the ECMWF model. *Quart. J. R. Met. Soc.* , **113**, July issue

Slingo, J. M. and Slingo, A. 1987b The response of a general circulation model to cloud longwave radiative forcing. II : Sensitivity to the cloud–prediction scheme. In preparation

Stephens, G. L. and Webster, P.J. 1981 Clouds and climate : sensitivity of simple systems. *J. Atmos. Sci.* , **38**, 235–247

Somerville, R. C. J. and Remer, L. A. 1984 Cloud optical thickness feedbacks in the CO_2 climate problem. *J. Geophys. Rev.* , **89**, 9668–9672

Webster, P. J. and Stephens, G. L. 1980 Tropical upper–tropospheric extended clouds: inferences from Winter MONEX. *J. Atmos. Sci.* , **37**, 1521–1541

Wetherald, R. T. and Manabe, S. 1980 Cloud cover and climate sensitivity. *J. Atmos. Sci.* , **37**, 1485–1510

Wetherald, R. T. and Manabe, S. 1986 An investigation of cloud cover change in response to thermal forcing. *Climatic Change* , **8**, 5–23

Williamson, D. L., Kiehl, J. T., Ramanathan, V., Dickinson, R. E. and Hack, J.J. 1987 *Description of NCAR Community Climate Model (CCM1).* NCAR Technical Note NCAR/TN–285+STR

a) Shortwave albedo (percent)

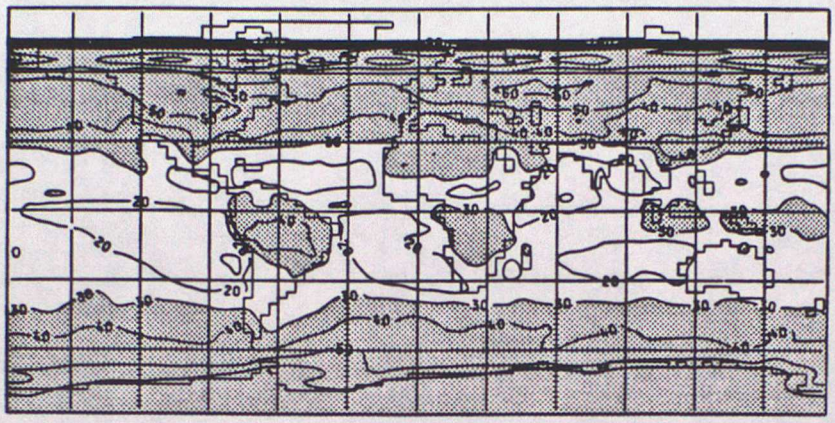

b) Outgoing longwave radiation (W m^{-2})

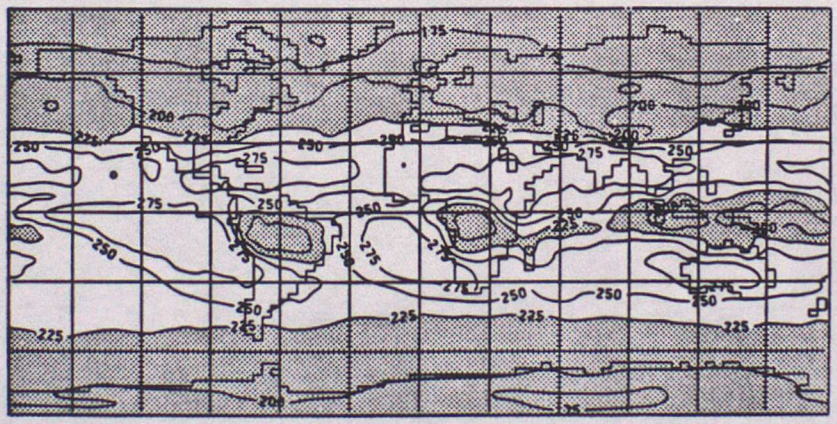

Figure 9.1 (a) Shortwave albedo and (b) Outgoing longwave radiation from Nimbus 7 Narrow Field of View data for December 1979 to February 1980. In (a) the contour interval is 10 per cent with values greater than 30 per cent dotted. In (b) the contour interval is 25 W m^{-2} with values smaller than 225 W m^{-2} dotted.

a) Shortwave albedo (percent)

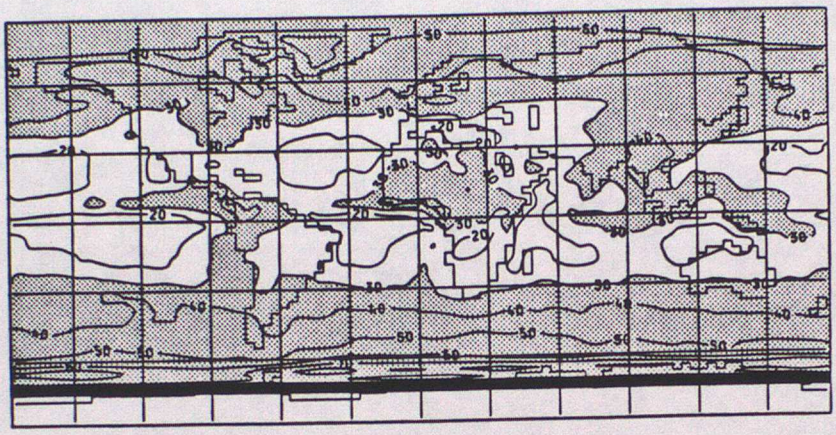

b) Outgoing longwave radiation (W m^{-2})

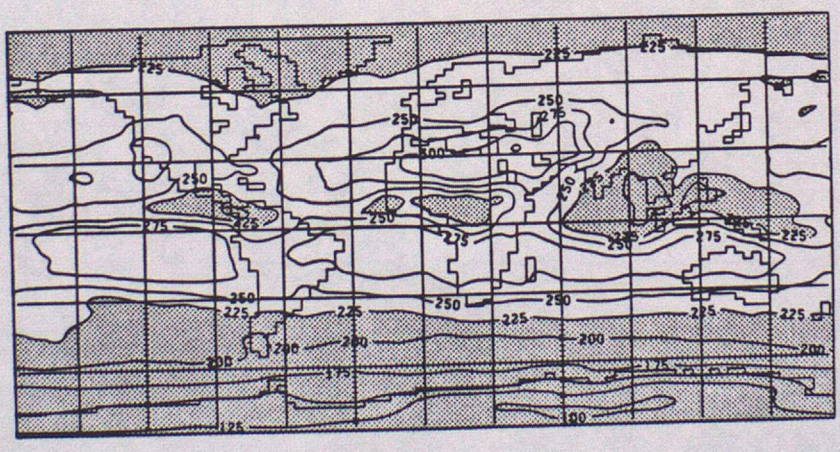

Figure 9.2 As Figure 9.1 but for June to August 1980.

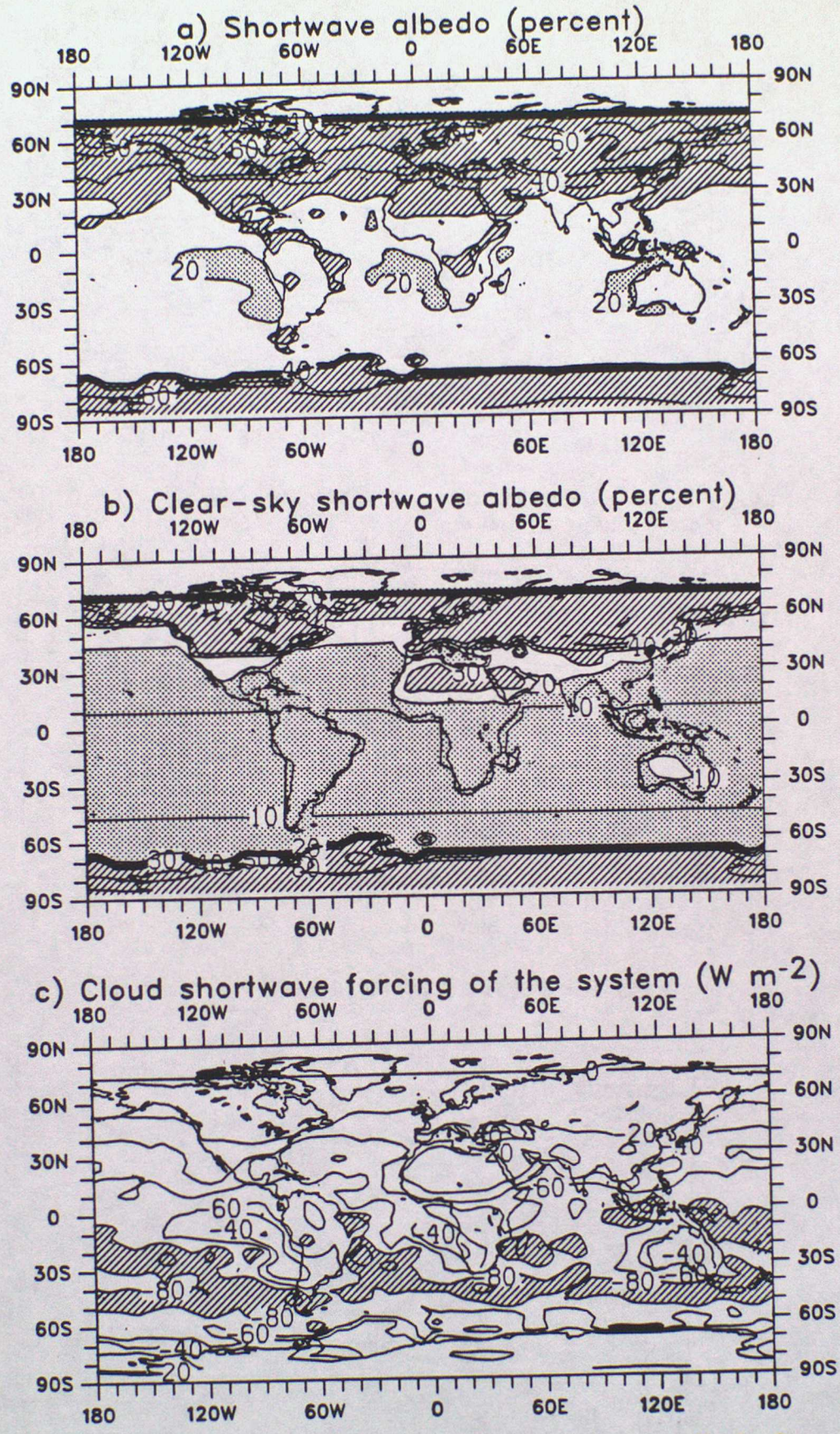

Figure 9.3 (a) Shortwave albedo and (b) Clear-sky shortwave albedo, from a January control integration of the NCAR Community Climate Model. The contour interval is 10 per cent. Values greater than 30 per cent are shaded and those smaller than 20 per cent are dotted. (c) Cloud shortwave forcing of the earth–atmosphere system. The contour interval is 20 W m^{-2} and values smaller than -80 W m^{-2} are shaded.

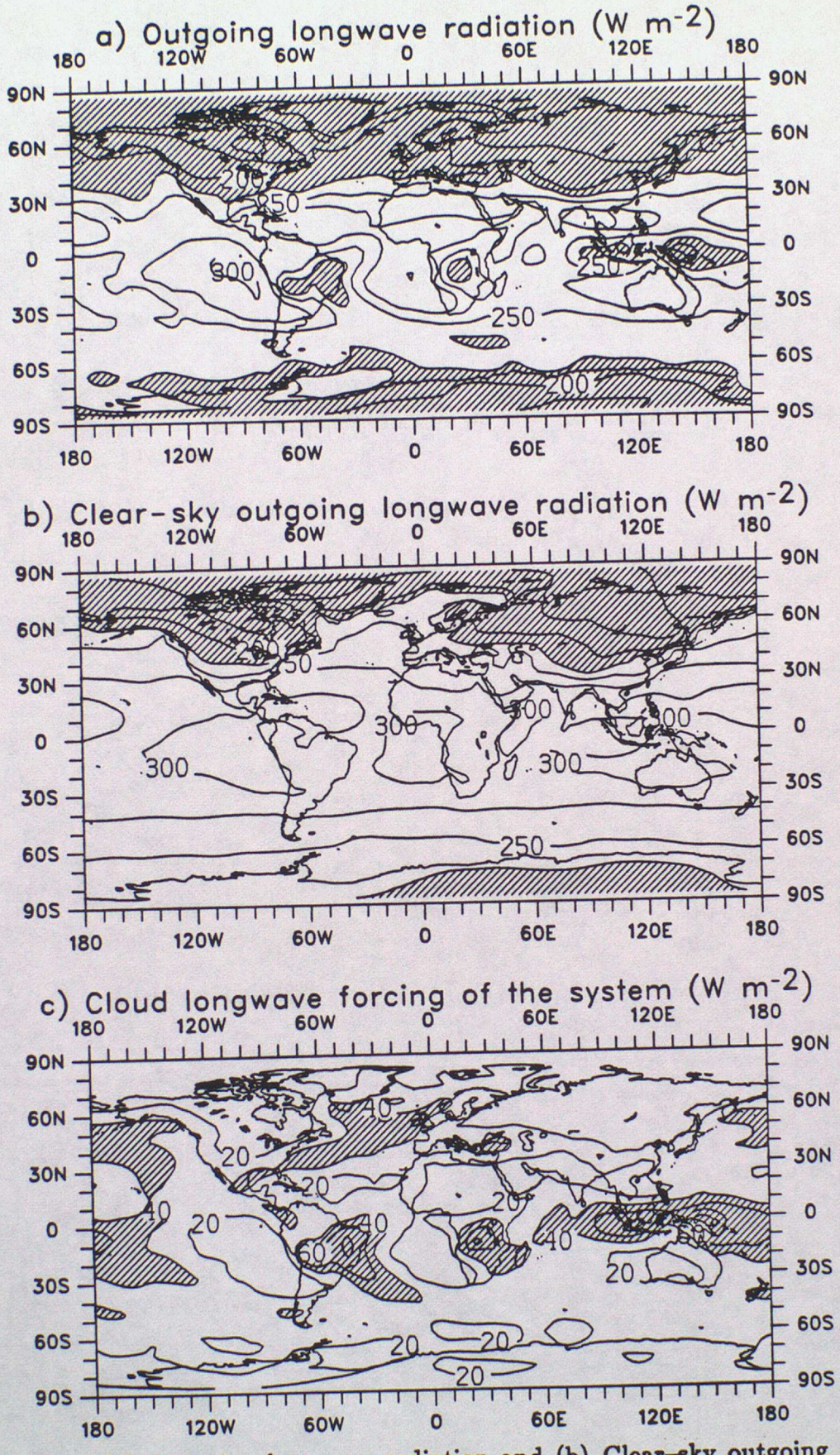

Figure 9.4 (a) Outgoing longwave radiation and (b) Clear-sky outgoing longwave radiation, from the same integration as in Figure 9.3. The contour interval is 25 W m^{-2} and values smaller than 225 W m^{-2} are shaded. (c) Cloud longwave forcing of the earth–atmosphere system. The contour interval is 20 W m^{-2} and values greater than 40 W m^{-2} are shaded.

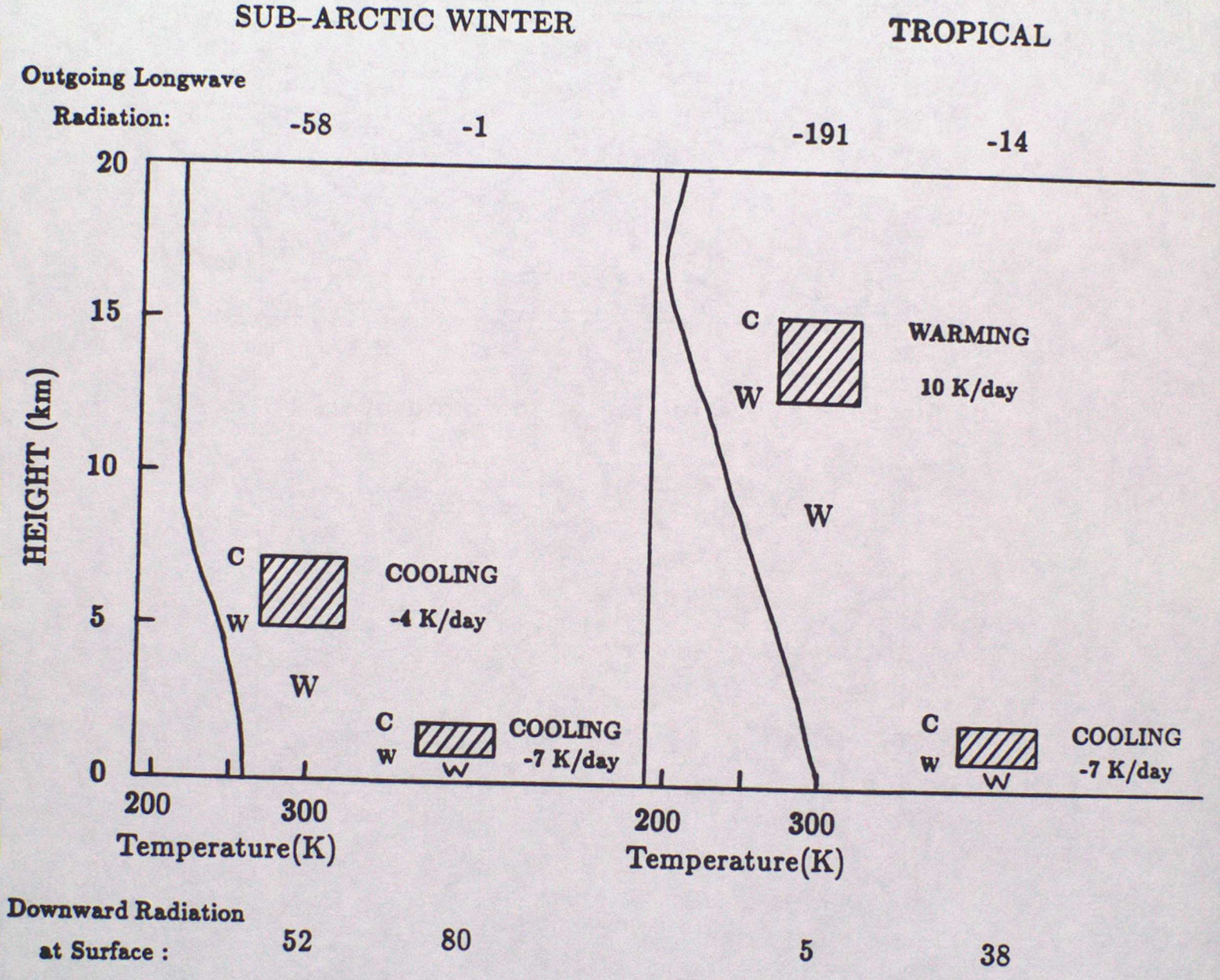

Figure 9.5 Schematic diagram of the temperature profiles in a sub–arctic winter and a tropical atmosphere and of the changes produced in the atmospheric longwave heating rates, outgoing longwave radiation (W m^{-2}) and downward longwave radiation at the surface (W m^{-2}) when a complete overcast by cloud is inserted at the levels shown. The letters C and W denote local cooling and warming, respectively, induced by the clouds.

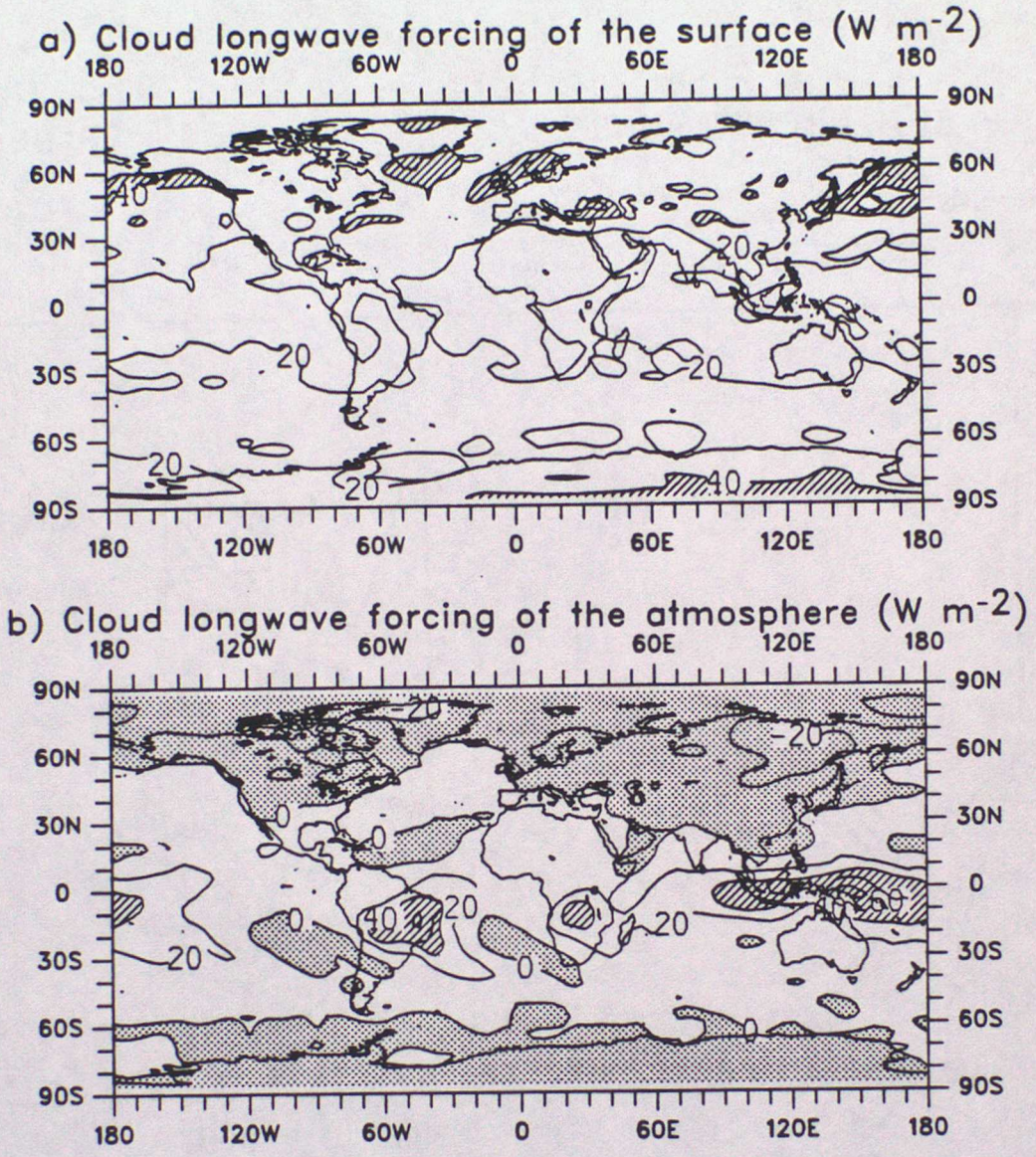

Figure 9.6 Cloud longwave forcing of (a) the surface and (b) the atmosphere, from the same integration as in Figure 9.3. The contour interval is 20 W m^{-2}. Values greater than 40 W m^{-2} are shaded and negative values are dotted.

(a)

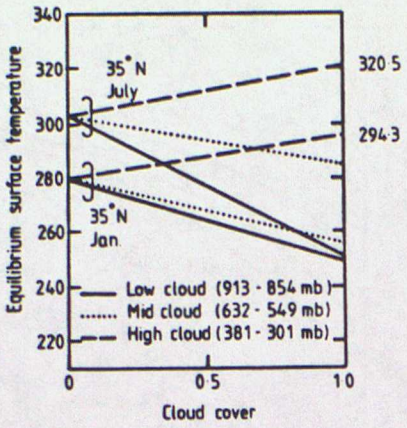

Equilibrium surface temperature distribution (K) as a function of cloud amount for the low, middle and high cloud cases using winter and summer solstice conditions at 35°N. Liquid water paths for the three cloud species are 140, 140 and 20 g m^{-2}, respectively.

(b)

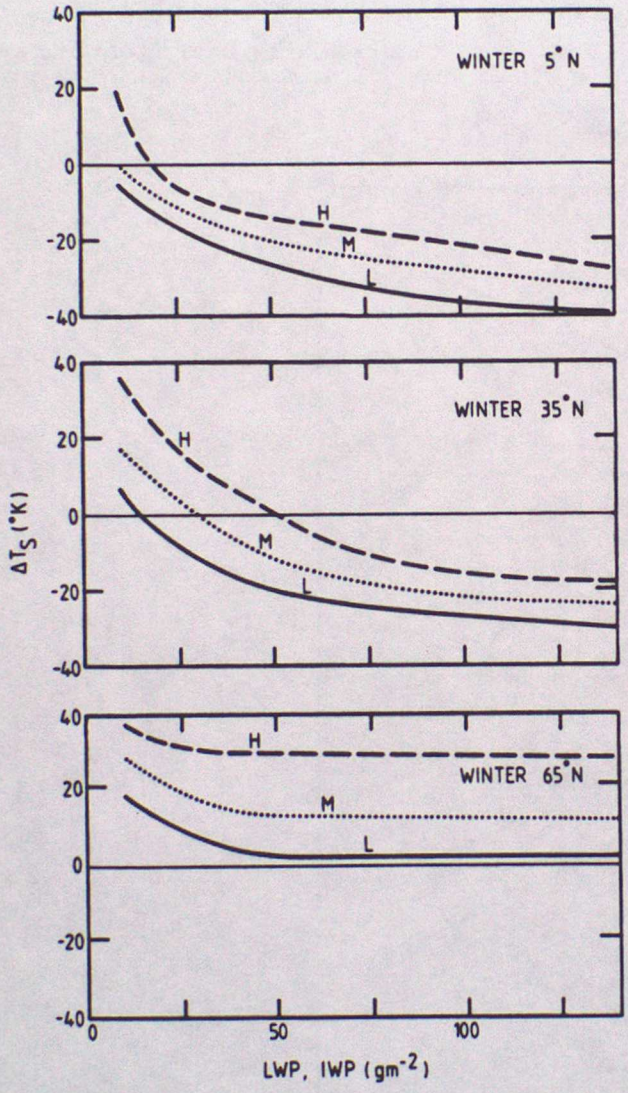

Surface temperature difference (ΔT_s) between clear and overcast conditions as a function of water or ice-water path (g m^{-2}) for the three cloud layers defined in Fig. 5. Results for 5, 35 and 65°N in winter are shown with a surface albedo of 0.102.

Figure 9.7 Dependence of surface temperature on (a) cloud amount for clouds at various levels and (b) cloud liquid water path (LWP) and latitude. From Stephens and Webster (1981).

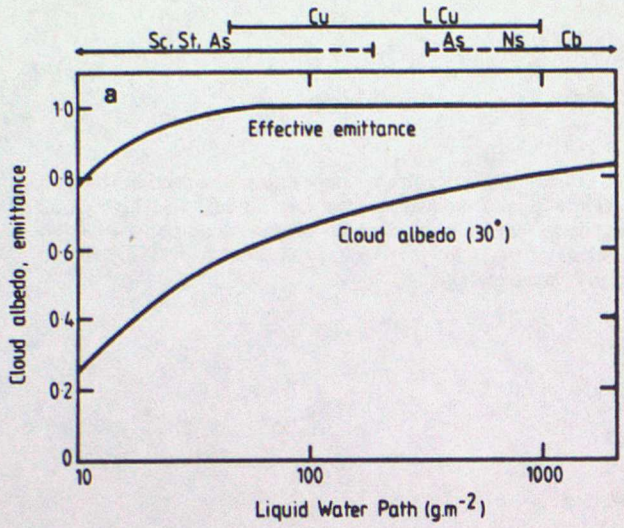

Cloud albedo and cloud effective emittance as a function of liquid-water path w for a zenith angle of 30°. Bars on upper abscissa denote approximate radiative property limits of various cloud species.

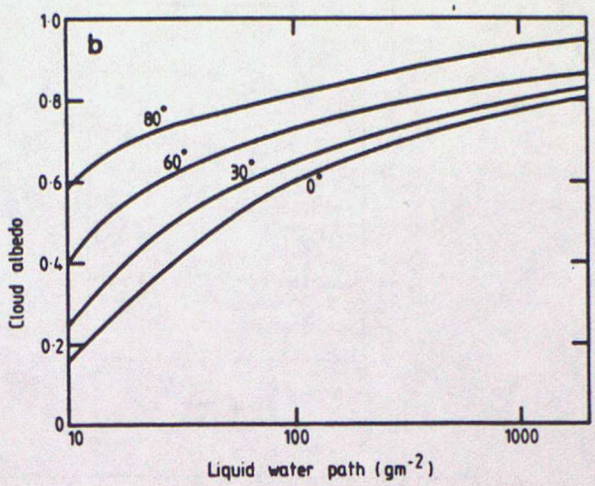

Cloud albedo as a function of liquid water path for various zenith angles.

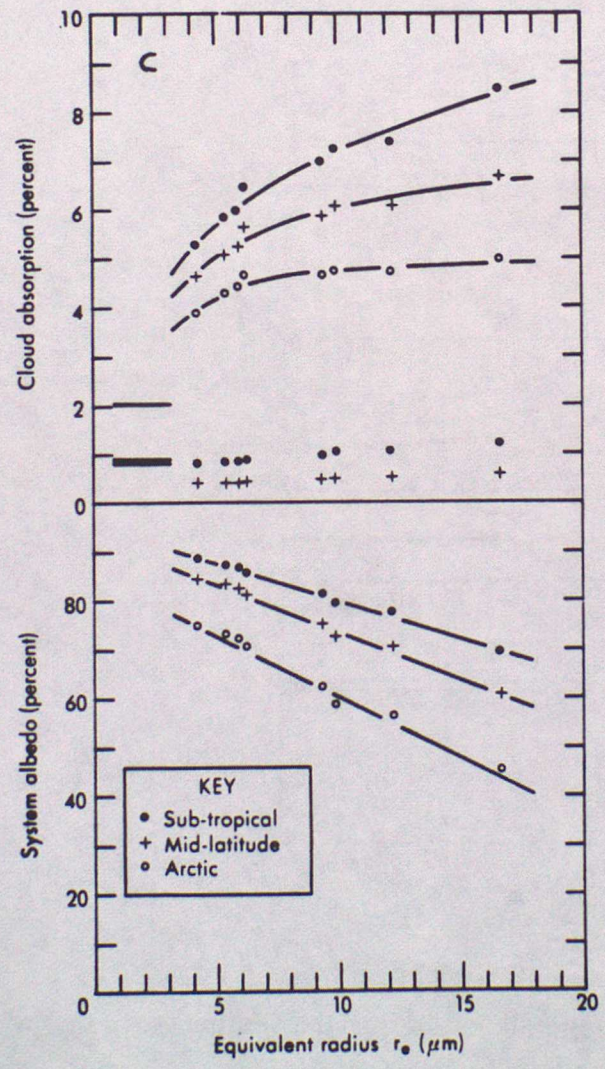

Cloud absorption and system albedo for the three atmospheric profiles shown in Fig. 6 as a function of the equivalent radius of the drop size distribution. The clear sky absorptions are shown by the horizontal bars.

Figure 9.8 Dependence of cloud radiative properties on (a) Liquid Water Path, (b) solar zenith angle and (c) equivalent radius of the drop size distribution. (a) and (b) are from Stephens and Webster (1981) and (c) is from Slingo and Schrecker (1982).

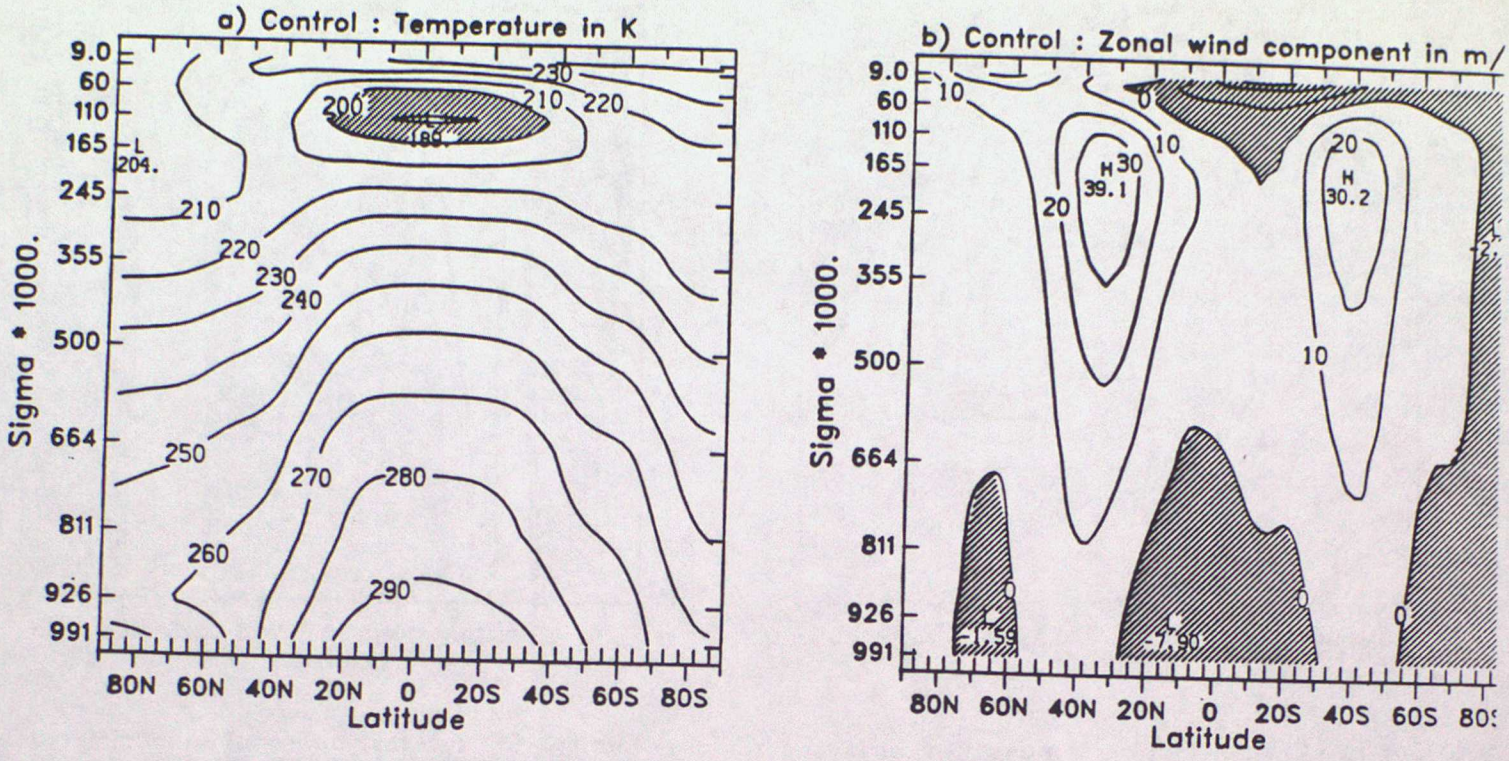

Figure 9.9 Zonal–mean (a) Temperatures and (b) Zonal wind components from the control experiment of CCM1 used by Slingo and Slingo (1987a). The contour interval for temperature is 10K with values lower than 200 K shaded. The contour interval for wind is 10 m s^{-1} with negative values shaded.

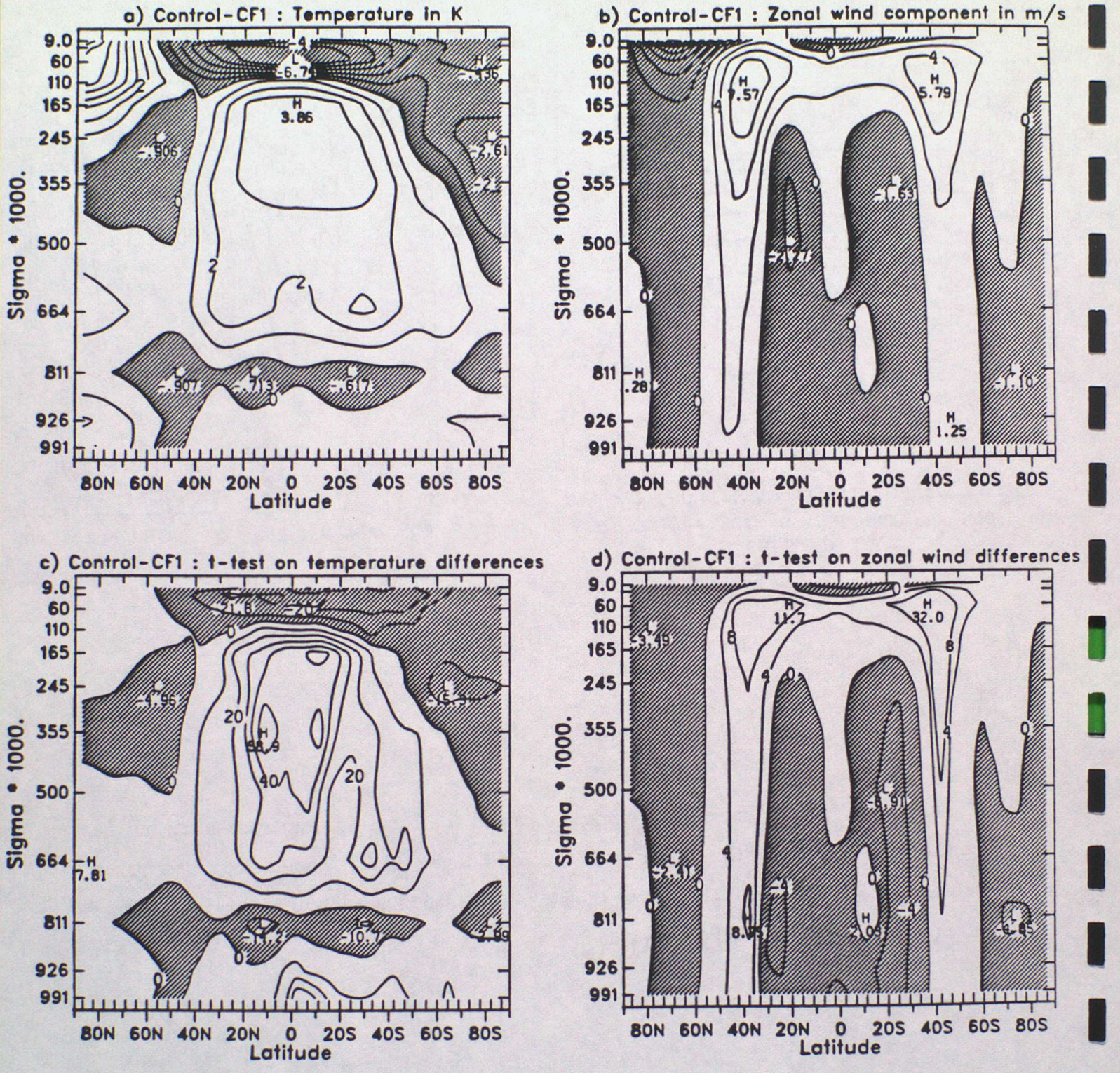

Figure 9.10 As Fig. 9.9 but for the zonal-mean (a) Temperature and (b) Zonal wind differences produced in CCM1 by cloud longwave forcing of the atmosphere. The corresponding t–statistics are shown in c) and d) respectively. The contour interval is 1 K in a), 2 m s^{-1} in b), 10.0 in c) and 4.0 in d). Negative values are shaded. For clarity, some of the contours in the southern hemisphere maximum have been omitted from (d).

a) Control : 200 mb wind and isotachs (m s^{-1})

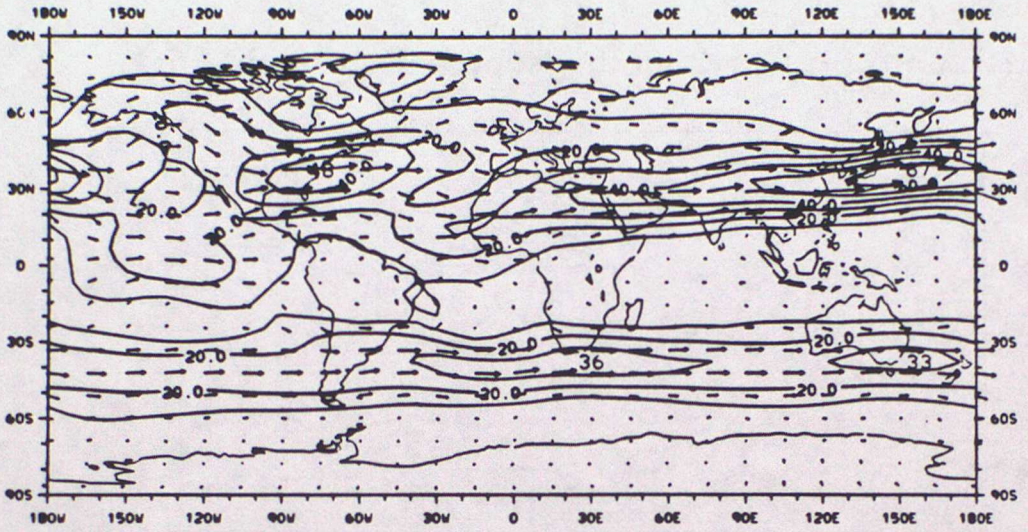

b) Control–CF1 : 200 mb wind and isotachs (m s^{-1})

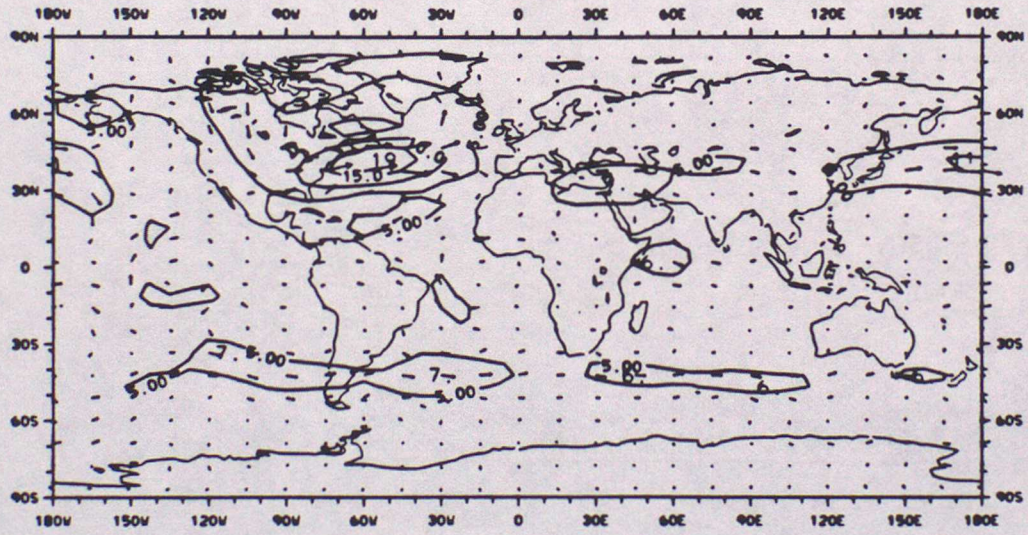

Figure 9.11 As Fig. 9.9 but for the 200mb wind vectors and isotachs for (a) the control and (b) the differences produced by cloud longwave forcing. The contour interval for the isotachs is 10 m s^{-1} in (a) and 5 m s^{-1} in (b). The length of the vectors is proportional to the wind speed. A vector whose length is 15^0 of longitude (the horizontal spacing betwen vectors) represents 50 m s^{-1} in (a) and 20 m s^{-1} in (b).

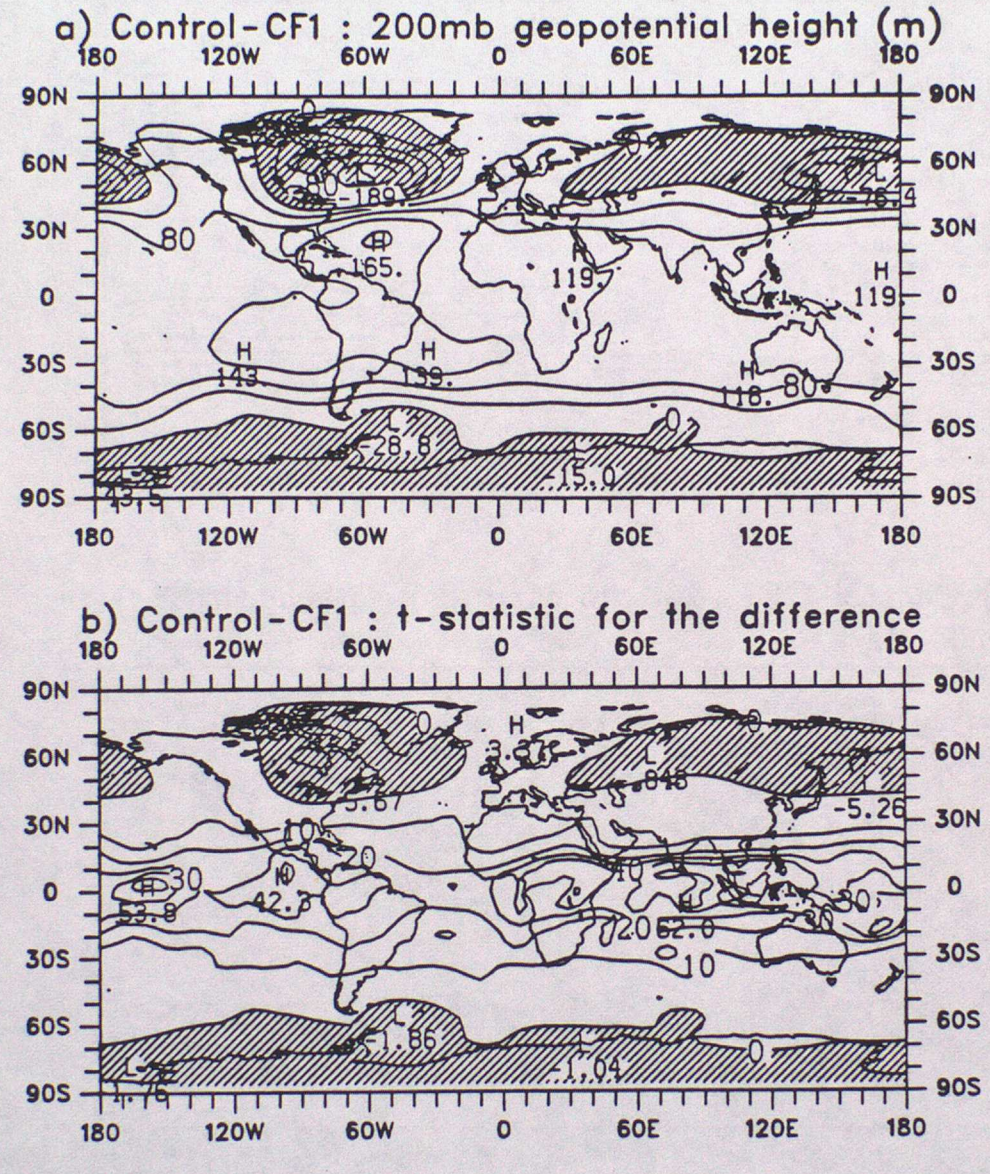

Figure 9.12 (a) As Fig. 9.9 but for the 200mb geopotential height differences produced by cloud longwave forcing. The contour interval is 40 metres. (b) the corresponding t–statistic. The contour interval is 10. Negative values are shaded in both plots.